MANIPULATING ACOUSTIC WAVE PROPAGATION WITH META-STRUCTURED SURFACES

TUO LIU

PhD

The Hong Kong Polytechnic University

2018

The Hong Kong Polytechnic University

Department of Mechanical Engineering

Manipulating Acoustic Wave Propagation with Meta-structured Surfaces

Tuo Liu

A thesis submitted in partial fulfilment of the requirements for the degree of Doctor of Philosophy

February 2018

CERTIFICATE OF ORIGINALITY

I hereby declare that this thesis is my own work and that, to the best of my knowledge and belief, it reproduces no material previously published or written, nor material that has been accepted for the award of any other degree or diploma, except where due acknowledgement has been made in the text.

_____ (Signed)

_____Tuo Liu_____ (Name of student)

ABSTRACT

Metamaterials are a class of artificial materials constructed on subwavelength scale to provide exotic properties absent in nature, enabling many counter-intuitive effects and innovative applications. Recently, the concept of metasurfaces was pushed forward as a promising evolution of metamaterials, where the modulation of wave behaviors is through the specific boundary conditions instead of the constitutive parameters. Among numerous emerging topics, this thesis focuses on metamaterials and metasurfaces for airborne sound either confined within waveguides or guided by structured surfaces open to the environment. Beyond the scope of seeking extraordinary properties along the real axis, the thesis also shows how judiciously tailored losses can play important roles in controlling sound propagation.

The thesis starts with a study on a type of gradient holey-structured metasurfaces, along which the dispersive group velocity of the structure-induced surface acoustic waves (SSAWs) slowly drops from that of air to zero. Broadband incident waves parallel and close to the metasurfaces can thus be effectively converted into the SSAWs, with various frequency components being decelerated until trapped at different positions, leading to spatial-spectrally modulated and highly compressed sound field, namely, the so-called acoustic rainbow trapping effect. The thesis further considers the inherent visco-thermal losses inside the holes, a non-negligible factor in practice. Unlike the lossless case, the gradually diminished group velocity becomes anomalous rather than zero at the trapping positions, suggesting that the system's attenuation reaches maximum. Consequently, the unavoidable strong backscattering in the absence of losses, due to the facts that the trapping is temporarily achieved and the local oscillation eventually radiates backward, is almost fully absorbed.

In the following chapter, a design approach of gradient-index (GRIN) holey-

structured metasurfaces is presented to manipulate airborne sound in the subwavelength regime via the SSAWs with large wave-vector values. Based on an explicit mapping relation between the effective index of the SSAWs and the hole depth of the unit cell, arbitrary GRIN profile of index values higher than that of air can be directly implemented by adjusting the depth distribution. As a representative example, subwavelength focusing is experimentally realized along a well-designed GRIN metasurface, in which the focal spot size is less than 1/7 of the wavelength in air. The thesis further demonstrates that two-dimensional (2D) subwavelength imaging is available when a scanning of the object plane is conducted, enabled by the near-field coupling between the evanescent waves and the slow SSAWs.

The meta-structured surfaces are capable of manipulating not only the SSAWs but also sound waves within waveguides. By decorating the rigid inner surfaces of acoustic waveguides with micro-structures, the resultant metamaterials can modulate the refractive index in a complex plane, which offers an intriguing opportunity to the study of parity-time (PT) symmetry in passive acoustic system. The exploration of non-Hermitian Hamiltonians possessing PT symmetry has tremendously advanced in experiment with optical system through the quantum-classical analogue, yet still a challenge for acoustics due to the lack of natural gain medium. This thesis reports an all passive acoustic PT-symmetric metamaterials crystal constructed through interleaving groove-structured and holey-structured acoustic metamaterials. It provides intrinsic passive PT-symmetric potential available in 2D space, which allows a flexible manipulation of unpaired wave vectors. At the transition point from unbroken to broken PT symmetry phase, unidirectional sound focusing effect is experimentally observed.

PUBLICATIONS ARISING FROM THE THESIS

Journal

1. **T. Liu**, F. Chen, S. Liang, H. Gao, and J. Zhu, Subwavelength acoustic focusing and imaging along a gradient-index metasurface, (in preparation, 2018).
2. R. Zhao, **T. Liu**, C. Wen, J. Zhu, L. Cheng, Theoretical modeling and optimization of porous coating for hypersonic-laminar-flow control, AIAA J. (accepted, 2018)
3. **T. Liu**, F. Chen, S. Liang, and J. Zhu, Unidirectional wave vectors manipulation in two-dimensional space with an all passive acoustic parity-time-symmetric metamaterials crystal, Phys. Rev. Lett. **120**, 124502 (2018).
4. **T. Liu**, S. Liang, F. Chen, and J. Zhu, Inherent losses induced absorptive acoustic rainbow trapping with a gradient metasurface, J. Appl. Phys. **123**, 091702 (2018).

Conference

1. **T. Liu** and J. Zhu, Acoustic metamaterials crystal for passive parity-time-symmetric modulation, in Metamaterials 2018, Espoo, Finland, IEEE. (accepted, 2018)
2. **T. Liu** and J. Zhu, Acoustic rainbow trapping through perforated structures, in 23rd International Congress on Sound & Vibration, Athens, Greece, 10-14 July 2016.

ACKNOWLEDGEMENTS

I would like to express my sincere gratitude to my chief supervisor Dr. Jie Zhu for his trust, support and help throughout the past three years of my Ph.D. study. He taught me not only all the research skills, but also ways of thinking. Without his invaluable guidance and continuous encouragement, I could not have finished all the research works and summarized them into this thesis. Meanwhile, my deep appreciation is dedicated to my co-supervisor Prof. Li Cheng, who has been generous in allowing me to attend his group meeting and in providing insightful suggestions. I must say I have been fortunate to be their student.

I wish to thank Dr. Xuefeng Zhu from Huazhong University of Science and Technology for his guidance and all those in-depth discussions on various projects. I am grateful to the support and help from Dr. Xiaobo Yin and his students during my visiting study at The University of Colorado, Boulder. This experience indeed broadened my horizons. I appreciate the valuable discussions with Dr. Xiang Yu from The Agency for Science, Technology and Research, Singapore, which really inspired me in many aspects. In addition, I also appreciate Prof. Chih-Yung Wen and Dr. Rui Zhao for their help on the project of hypersonic boundary layers.

I would like to thank my colleagues in Dr. Zhu's group: Mr. Fei Chen, Mr. Shanjun Liang and Ms. He Gao, for the help they offered, from everyday life to research tasks. I would also like to thank the students from Prof. Cheng's and Prof. Wen's groups, as well as my colleagues in Room FJ610. I really had a wonderful time with them.

Last but not least, I would like to thank my parents for their constant support and encouragement throughout my study. Special thanks to my beloved fiancée Siyuan: meeting you at PolyU was the best thing that ever happened to me.

TABLE OF CONTENTS

LIST OF FIGURES

Chapter 1: Introduction

1.1 Acoustic metamaterials

Metamaterials are artificial materials constructed with subwavelength building blocks while exhibiting on-demand macroscopic effective properties and functionalities not available in nature. Fundamentally, what distinguish them from other types of artificial materials, such as photonic and phononic crystals, are that: 1. the building blocks, also refer to as meta-atoms or unit cells, are much smaller than the wavelength (usually less than 1/10 wavelength) and are assembled in such a way that they collectively behave like a continuous medium; 2. the unconventional wave behaviors are governed by mainly the local behavior of individual building blocks rather than solely the multiple scattering among them. Rapid development in this field has been continuously bringing new insights into novel and extraordinary ways of wave manipulation, beyond the restriction of conventional materials, beyond what people have ever imagined.

The notion of metamaterials originated from Veselago's theoretical exploration on negative refractive index for electromagnetic waves [1], in which he predicted that an effective medium with simultaneously negative permittivity and permeability still obeys the Maxwell's equations but allows unexpected ways of wave manipulation, e.g. negative refraction. It was Pendry *et al.*'s revolutionary works [2,3] almost three decades later that opened up the path to these unusual properties with practical structures (negative permittivity: metal wires; negative permeability: split ring resonators). Soon after Pendry's proposals, Smith *et al.* [4] demonstrated the first experimental realization of a metamaterial possessing negative-index of refraction. In terms of applications, an intriguing part of negative-index metamaterial is that they are capable of amplifying the evanescent wave fields that decay exponentially outside a

source to restore sub-diffraction-limited images, namely, the so-called “superlens” [5]. Another milestone in this field is the introduction of transformation optics, a powerful tool for materials design to mold the flow of waves at will. The idea is based on the invariance of Maxwell equations under coordinate transformation. It suggests that any coordinate-transformation-based deformation, e.g. stretching and bending, is able to be accomplished through specific spatial distribution of the material properties. The required effective properties, albeit extreme and complicated in general, are exactly what inhomogeneous metamaterials can offer. One of the most exciting applications benefited from this technique is the so-called invisible cloak [6-8]. By steering the waves around the object, the ability to conceal an object, which only existed in science fiction before, now becomes possible with the help of transformation optics and well-designed metamaterials.

The first acoustic metamaterial was constructed by periodically embedding rubber-coated metallic spheres in epoxy, leading to local resonance with frequency far below that corresponds to the Bragg scattering [9]. While originally proposed as a tremendous leap of phononic crystals and a new mechanism for sound insulation, this work echoed with the essence of the underlying physics of electromagnetic metamaterials and hence is well known as a groundbreaking investigation of acoustic metamaterials. In parallel to the progress of locally resonant phononic crystals, many novel concepts from electromagnetic metamaterials have been directly borrowed to create their acoustic counterparts, as the equations describing the two wave systems share very similar mathematical form (although the two wave phenomena are fundamentally different in some respects, e.g. electromagnetic waves are transverse vector waves while fluid-borne acoustic waves are compressional scalar waves). In analogy to the electric permittivity and the magnetic permeability that govern electromagnetic wave behavior,

the mass density ρ and the bulk modulus K are the two key material properties controlling sound propagation, as evidenced by the linearized acoustic wave equation in a homogeneous medium without source term

$$\nabla^2 p - \frac{\rho}{K}\frac{\partial^2 p}{\partial t^2} = 0, \tag{1.1}$$

where p is the acoustic pressure, and the speed of sound and acoustic impedance are given by $c = \sqrt{K/\rho}$ and $Z = \sqrt{K\rho}$, respectively. Inspired by the advances of electromagnetic metamaterials as well as locally resonant phononic crystals, acoustic metamaterials with exotic properties, e.g. single/double-negative [10-19] and anisotropic effective properties [20-28], etc., have been designed and tested in experiments; accordingly, metamaterial-based devices for novel functionalities such as sub-wavelength focusing/imaging [19-22,24,28-32] and acoustic cloaking [33-39] have also been successfully demonstrated.

The past 17 years have witnessed a growing amount of studies in the field of acoustic metamaterials, accompanied by its ever-expanding scope that covers more diverse topics and directions [40-42]. As have been mentioned in the first paragraph, nowadays, the term metamaterials can refer to any artificial material whose building blocks are of subwavelength feature (either resonant or non-resonant) and collectively act like a continuous medium (usually but not necessarily in periodic manner) to produce unusual effective properties and/or functionalities, not limited to those for linear and passive systems in early stage. For instance, the exploration of effective material properties has been broadened from the real axis to the entire complex domain, in which the imaginary part represents either the gain that offers energy to incoming waves or the loss that takes away energy from a system. For acoustic waves, gain medium is not readily available in nature, while loss is omnipresent yet not easy to be

precisely regulated. The well-tailored gain and loss enabled by acoustic metamaterials, especially when they are independent to the real part of the effective properties, would contribute to a series of sub-fields, not only the apparent ones including sound absorption and loss compensation, but also those emerging topics ranging from non-reciprocal acoustic devices [43,44] to non-Hermitian or parity-time-symmetric acoustics [45-50]. Besides, there has been an increasing trend towards ultrathin and ultra-compact metamaterial-based devices, which led to the development of acoustic metasurfaces [51-55]. Acoustic metasurfaces are planar acoustic metamaterials with subwavelength thickness, composed of monolayer or multilayer stacks of meta-atoms. The modulation of wave behaviors with acoustic metasurfaces is through the specific boundary conditions rather than the constitutive parameters, thus enabling delicate ways of wave-front modulation and airborne guided mode manipulation.

1.2 Organization of the thesis

Although the field of acoustic metamaterials has tremendously advanced, as we have discussed above, it has been promptly evolving since its emergence, which leaves us many possibilities and new directions. Among numerous emerging topics in this field, this thesis will focus on the design of meta-structured surfaces for two types of guided waves: 1. structure-induced surface acoustic waves (SSAWs) supported a perforated surface open to the environment; 2. sound waves confined within waveguides. Also, beyond the scope of conventional artificial materials that modulate the effective properties in real-number space, the thesis would like to explore how judiciously tailored losses could be adjusted to respect the passive parity-time symmetry and subsequently control sound propagation.

This thesis consists of five chapters including an introductory chapter (present chapter), a conclusion chapter (Chapter 5) and three main chapters (Chapters 2-4) on

the proposed meta-structured surfaces for acoustic wave manipulation. Appendices are provided at the end for additional but less significant details. The three main chapters are organized as follows:

Chapter 2 firstly investigates the SSAWs that exist at rigid surfaces immersed in air and periodically perforated with subwavelength square holes. A theoretical model is developed to describe the SSAWs and is numerically verified using full-wave simulations. Based on the theoretical results, we then propose a type of gradient holey-structured metasurfaces at which the frequency-dependent group velocity of the SSAWs slowly drops from that of airborne sound in free space to zero during propagation, to achieve the so-called acoustic rainbow trapping effect. The thesis then considers the inherent thermal and viscous losses inside the holes, a non-negligible factor in practice. Distinct from the lossless case, the gradually diminished group velocity exhibits anomalies rather than zero near the trapping positions, suggesting the maximum attenuation of the system. Consequently, the unavoidable strong backscattering in the absence of losses, due to the facts that the trapped sound is temporarily achieved and the local sound oscillation eventually radiates backward, can be almost fully absorbed, forming reflectionless spatial-spectral modulation. The study in this chapter may provide theoretical basis for the practical design of acoustic devices to achieve high performance sensing and filtering. It may also be helpful for the study of hypersonic boundary layer stabilization.

Chapter 3 presents a design approach of gradient-index (GRIN) holey-structured metasurfaces to manipulate airborne sound in the subwavelength regime via the SSAWs with high wave-vector values. Based on the dispersion relation derived in Chapter 2, an explicit expression can be obtained to map the effective refractive index of the SSAWs into the hole depth of the unit cell. Arbitrary GRIN profile with effective refractive

index higher than that of air for the SSAWs can thus be straightforwardly achieved by simply introducing a specific spatial distribution of the hole depth. As a representative example, subwavelength focusing effect is experimentally realized with a well-designed GRIN metasurface, in which the full width at half maximum of the focal spot is less than one-seventh of the wavelength in air. The thesis further demonstrates in experiment that two-dimensional subwavelength imaging with the same metasurface is also available when a scanning of the object plane is conducted. This work provides a feasible pathway to the subwavelength manipulation of airborne sound as well as an ideal experimental platform to directly observe the wave propagation and energy flow inside two-dimensional bulk metamaterial counterparts. Meanwhile, the proposed design approach can be easily applied to other GRIN acoustic devices due to its simplicity.

In Chapter 4, this thesis shows that, by replacing the rigid inner boundaries of acoustic waveguides with meta-structured surfaces, the resultant metamaterials can be used to modulate the refractive index in complex plane, which offers an intriguing opportunity to the study of parity-time (PT) symmetry in passive acoustic system. An experimental investigation of PT-symmetric medium is conducted with passive acoustic metamaterials crystal. The metamaterials crystal consists of interleaved groove-structured and holey-structured acoustic metamaterials (namely, groove-structured surfaces within waveguide and holey-structured surfaces connected the waveguide with outside). It is able to provide intrinsic PT-symmetric potential extended in two-dimensional space, through which the unpaired wave vectors can be flexibly controlled. At the exceptional point where PT symmetry spontaneously breaks, one-way acoustic focusing (along with reflectionless acoustic transparency in the opposite direction) is experimentally demonstrated, available over a certain spectrum. It confirms that passive

acoustic systems are capable of carrying experimental studies of PT symmetry and at the same time shows the unique functionalities enabled by the unpaired wave vectors that are judiciously tailored in two-dimensional space.

Chapter 2:

Acoustic rainbow trapping through gradient metasurfaces

2.1 Introduction

The ability to slow down and trap light opens the path to precise control and temporary storage of optical waves, and enhanced light-matter interactions, which suggests potential practical applications in areas such as nonlinear optics, quantum optics, all-optical memories, etc [56,57]. However, the intrinsic delay-bandwidth conflict due to causality limits the practical development of conventional slow-light systems. The concept of "trapped rainbow" was then introduced to overcome this challenge [58-66], based on which various frequency components of broadband optical waves can be slowed down and trapped at different positions. Hence a high delay-bandwidth product can be achieved.

Unlike the significant advances in optical waves, acoustic rainbow trapping (ART) had not been realized until recent years. It is due to the fact that, contrary to the strong chromatic dispersion available in nature, almost all naturally-occurring materials are regarded as being non-dispersive in the sense of airborne sound. The emergence of artificial materials with exotic effective properties absent in nature suggests a possible way to the strong dispersion required by slow sound system [67-70]. Following this idea, ART effect has been experimentally demonstrated in two seminal works, through a gradient anisotropic metamaterial [71] and a chirped sonic crystal [72], respectively, in analogy with the optical trapped rainbow. Structures that are spatially coiled have also been utilized to go into a deeper subwavelength regime and make better use of space [73,74]. Besides airborne sound, the concept of trapped rainbow has been extended to elastic waves, e.g. Lamb and Rayleigh waves [75-77]. These highly-dispersive artificial materials may benefit many applications such as high performance

acoustic sensing/filtering [78,79] and stabilization of hypersonic boundary layers [80,81].

Among these artificial materials for ART effect, one of the most effective solutions is through the structure-induced surface acoustic waves (SSAWs, also referred to as spoof or designer surface acoustic waves) [82-89], a type of airborne surface acoustic mode supported by periodically corrugated, perforated or resonator-embedded rigid surfaces. Similar to spoof surface plasmon polaritons in electromagnetic wave system [90,91], the dispersion characteristics of the SSAWs can be engineered through adjusting the geometries of the unit cells to obtain high spatial frequency as well as enhanced and confined field that is open to the environment. The studies on this topic have enabled many fascinating functionalities and applications such as beam collimation [86,92-95], imaging [96], focusing [30,97,98], rainbow trapping [71,79,89], enhanced sensing [78], directional excitation/coupling [86,99,100], and topological insulator [101]. However, previous designs are all based on groove structures (two-dimensional unit cell) that require infinite size in the third dimension. This makes them unrealistic for practical applications, especially at low frequency range where the difference between theoretical and experimental results become non-negligible [71,78]. Meanwhile, the thermal and viscous losses inside the narrow regions of ART structures cannot be neglected owing to the resonating nature of the unit cells yet has not hitherto been theoretically investigated.

In this chapter, a theoretical model is built to investigate the SSAWs that exist at rigid surfaces immersed in air and periodically perforated with subwavelength square holes, which is numerically verified using full-wave simulations. Based on this, a type of gradient holey-structured metasurfaces is proposed, at which the dispersive group velocity of the SSAWs slowly drops from that of air to zero along the wave propagation

direction. Incident plane acoustic waves grazing the metasurface of various frequencies can thus be coupled to the SSAWs and be decelerated to standstill in different manners, resulting in enhanced sound field that is highly compressed and spatial-spectrally separated, namely, the so-called ART effect. The trapping patterns for different hole depth profiles are also discussed. Next, the inherent thermal and viscous losses are taken into consideration. What differs the lossy metasurface from the lossless one here is that an anomalous point of group velocity exists, indicating the maximum attenuation of the surface mode. As a result, the backscattering stems from the intermodal coupling between the bidirectional travelling modes is nearly eliminated, forming a so-called absorptive ART effect. This chapter has been published in Refs. [89] and [102].

2.2 Structure-induced surface acoustic waves

To realize ART effect with a gradient holey-structured metasurface, an important step is to convert airborne acoustic waves in free space into the SSAWs and spatially modulate their dispersion behavior. Hence this section start with an analysis of the dispersion behavior of the SSAWs.

As depicted in Fig. 2.1(a), consider a rigid surface perforated with periodic deep subwavelength square holes that form a two-dimensional array of quarter-wavelength resonators. It is immersed in air, with material properties being denote as density ρ_0 and speed of sound c_0. Geometrical parameters of the perforation includes the side length and depth of the holes a and h, and the lattice constant of the unit cell d. For time dependence with form $e^{j\omega t}$, arbitrary incident plane acoustic wave penetrating to the surface can be expressed as

$$p_i = e^{-jk_x x} e^{-jk_y y} e^{jk_z z}, \tag{2.1}$$

$$v_{z,i} = -\frac{1}{j\omega\rho_0}\frac{\partial p_i}{\partial z} = -\frac{k_z}{\rho_0\omega} e^{-jk_x x} e^{-jk_y y} e^{jk_z z}, \tag{2.2}$$

where p_i denotes the acoustic pressure of incident wave, $v_{z,i}$ denotes the z-component particle velocity and $j=\sqrt{-1}$. Define $q=\sqrt{k_x^2+k_y^2}$ as the in-plane wavevector and $k_z=\sqrt{k_0^2-q^2}$ as the out-of-plane wavevector, in which $k_0=\omega/c_0$ is the wavenumber or airborne sound in free space, with ω being the angular frequency. The reflected acoustic pressure $p_r^{(m,n)}$ and z-component particle velocity $v_{z,r}^{(m,n)}$ of the (m,n)-th order diffracted wave are written as

$$p_r^{(m,n)}=R_{mn}e^{-jk_x^{(m)}x}e^{-jk_y^{(n)}y}e^{-jk_z^{(m,n)}z}, \tag{2.3}$$

$$v_{z,r}^{(m,n)}=\frac{k_z^{(m,n)}}{\rho_0\omega}R_{mn}e^{-jk_x^{(m)}x}e^{-jk_y^{(n)}y}e^{-jk_z^{(m,n)}z}. \tag{2.4}$$

where $k_x^{(m)}=k_x+\frac{2\pi m}{d}$, $k_y^{(n)}=k_y+\frac{2\pi n}{d}$, and $k_z^{(m,n)}=\sqrt{k_0^2-(k_x^{(m)})^2-(k_y^{(n)})^2}$ with $m,n\in\mathbb{Z}$. R_{mn} is the reflection coefficient of the (m,n)-diffraction order, in which $(0,0)$ represents the specular reflection.

Since the side length a is much smaller than the operating wavelength ($a\ll\lambda$), fundamental mode dominates inside the holes. Consequently, the sound pressure and z-component particle velocity take the form

$$p_h=C_1e^{-jk_0z}+C_2e^{jk_0z}, \tag{2.5}$$

$$v_{z,h}=\frac{k_0}{\rho_0\omega}(C_1e^{-jk_0z}-C_2e^{jk_0z}). \tag{2.6}$$

Here C_1 and C_2 denote the pressure amplitudes of the forward and backward propagating modes, respectively. The hole bottom is rigid ($v_{z,h}\big|_{z=-h}=0$) so that $C_2=C_1e^{2jk_0h}\equiv Ce^{2jk_0h}$.

For $a\ll\lambda$, the continuity condition of acoustic pressure at the interface requires

that the mean pressure over the opening area at $z = 0^+$ equals that inside the holes at $z = 0^-$, yielding

$$\frac{1}{a^2}\int_{x,y=-a/2}^{x,y=a/2}(e^{-jk_x x}e^{-jk_y y} + \sum_{m,n=-\infty}^{+\infty} R_{mn}e^{-jk_x^{(m)}x}e^{-jk_y^{(n)}y})\mathrm{d}x\mathrm{d}y = C(1+e^{2jk_0 h}), \qquad (2.7)$$

which can be further derived as

$$\sum_{m,n=-\infty}^{+\infty}(\delta_{mn,00} + R_{mn})S_{mn} = C(1+e^{2jk_0 h}), \qquad (2.8)$$

where $S_{mn} = a^{-2}\int_{-\frac{a}{2}}^{\frac{a}{2}} e^{-jk_x^{(m)}x}\mathrm{d}x\int_{-\frac{a}{2}}^{\frac{a}{2}}\mathrm{d}y\ e^{-jk_y^{(n)}y} = \mathrm{sinc}(k_x^{(m)}a/2)\mathrm{sinc}(k_y^{(n)}a/2)$ is the overlap integral between the (m,n)-th order diffracted mode and the fundamental mode inside the holes; $\delta_{mn,00}$ is the Kronecker delta function [$\delta_{mn,00} = 1$ for $(m,n) = (0,0)$ and $\delta_{mn,00} = 0$ for $(m,n) \neq (0,0)$]. The *z*-component particle velocity $v_z\big|_{z=0}$ is continuous at the opening area while equals to zero elsewhere:

$$-\frac{k_z}{\rho_0\omega}e^{-jk_x x}e^{-jk_y y} + \sum_{m,n=-\infty}^{+\infty}\frac{k_z^{(m,n)}}{\rho_0\omega}R_{mn}e^{-jk_x^{(m)}x}e^{-jk_y^{(n)}y} = \begin{cases}\dfrac{k_0}{\rho_0\omega}C(1-e^{2jk_0h}) & x,y\in(-\dfrac{a}{2},\dfrac{a}{2})\\ 0 & x,y\notin(-\dfrac{a}{2},\dfrac{a}{2})\end{cases}. \qquad (2.9)$$

One may multiply the above equation by $e^{jk_x^{(r)}x}e^{jk_y^{(s)}y}$ ($r,s\in\mathbb{Z}$) and average over the unit cell area:

$$\begin{aligned}\frac{1}{d^2}\sum_{m,n=-\infty}^{+\infty}\int_{x,y=-d/2}^{x,y=d/2}(R_{mn}-\delta_{mn,00})k_z^{(m,n)}e^{-j(k_x^{(m)}-k_x^{(r)})x}e^{-j(k_y^{(n)}-k_y^{(s)})y}\mathrm{d}x\mathrm{d}y\\ = \frac{1}{d^2}\int_{x,y=-a/2}^{x,y=a/2}Ck_0(1-e^{2jk_0h})e^{jk_x^{(r)}x}e^{jk_y^{(s)}y}\mathrm{d}x\mathrm{d}y.\end{aligned} \qquad (2.10)$$

Based on the orthogonality of the exponential function, Eq. (2.10) can be derived as

$$R_{rs} = \delta_{rs,00} + C(1-e^{2jk_0h})\frac{a^2}{d^2}\frac{k_0}{k_z^{(r,s)}}S_{rs}^*. \qquad (2.11)$$

where $S_{rs}^{*} = a^{-2}\int_{-\frac{a}{2}}^{\frac{a}{2}} e^{jk_x^{(r)}x}\mathrm{d}x\int_{-\frac{a}{2}}^{\frac{a}{2}} \mathrm{d}y\ e^{jk_y^{(s)}y} = \mathrm{sinc}(k_x^{(r)}a/2)\mathrm{sinc}(k_y^{(s)}a/2)$. Substituting Eq. (2.11) into Eq. (2.8) yields

$$2S_{00} + C(1-e^{2jk_0h})\frac{a^2}{d^2}\sum_{r,s=-\infty}^{+\infty}\frac{k_0}{k_z^{(r,s)}}S_{rs}^{*}S_{rs} = C(1+e^{2jk_0h}). \tag{2.12}$$

The coefficient C is subsequently determined as

$$C = \frac{2S_{00}}{(1+e^{2jk_0h}) - (1-e^{2jk_0h})\frac{a^2}{d^2}\sum_{r,s=-\infty}^{+\infty}\frac{k_0}{k_z^{(r,s)}}S_{rs}^{*}S_{rs}}. \tag{2.13}$$

The reflection coefficients in Eq. (2.11) can thus be written as

$$R_{mn} = \delta_{mn,00} + \frac{2(1-e^{2jk_0h})\frac{a^2}{d^2}\frac{k_0}{k_z^{(m,n)}}S_{mn}^{*}S_{00}}{(1+e^{2jk_0h}) - \frac{a^2}{d^2}(1-e^{2jk_0h})\sum_{r,s=-\infty}^{+\infty}\frac{k_0}{k_z^{(r,s)}}S_{rs}^{*}S_{rs}}. \tag{2.14}$$

Note that $-j\tan(k_0h) = \frac{1-e^{2jk_0h}}{1+e^{2jk_0h}}$ and $S_{rs}^{*} = S_{rs} = \mathrm{sinc}\left(k_x^{(r)}a/2\right)\mathrm{sinc}\left(k_y^{(s)}a/2\right)$. Hence Eq. (2.14) is simplified as

$$R_{mn} = \delta_{mn,00} - \frac{2j\tan(k_0h)\frac{a^2}{d^2}S_{00}S_{mn}\frac{k_0}{k_z^{(m,n)}}}{1 + j\tan(k_0h)\frac{a^2}{d^2}\cdot\sum_{r,s=-\infty}^{+\infty}\frac{k_0}{k_z^{(r,s)}}S_{rs}^{2}}. \tag{2.15}$$

A true surface mode should be propagative within the *xy*-plane along the surface while evanescent in the half-space $z > 0$ away from the surface, which requires $q > k_0$ and $jk_z > 0$. Thus, by letting $jk_z^{(r,s)} = \sqrt{(k_x^{(r)})^2 + (k_y^{(s)})^2 - k_0^2}$, the dispersion relation of the SSAWs can be obtained by analyzing the divergences of the reflection coefficients [103], namely, the zeros of the denominator of Eq. (2.15)

$$1 - k_0\tan(k_0h)\frac{a^2}{d^2}\cdot\sum_{r,s=-\infty}^{+\infty}\frac{S_{rs}^{2}}{\sqrt{(q^{(r,s)})^2 - k_0^2}} = 0, \tag{2.16}$$

where $(q^{(r,s)})^2 = (k_x^{(r)})^2 + (k_y^{(s)})^2$. It can be perceived from Eq. (2.16) that the SSAWs are a result of the interaction between the local sound oscillation inside individual building blocks and the mutual coupling among neighboring building blocks. The propagation characteristics of such surface mode are governed by the geometrical parameters of the structures. This is distinct from conventional elastic surface waves such as Rayleigh or Stoneley waves that arise from the superposition of at least two types of bulk modes along a free surface or an interface between two media.

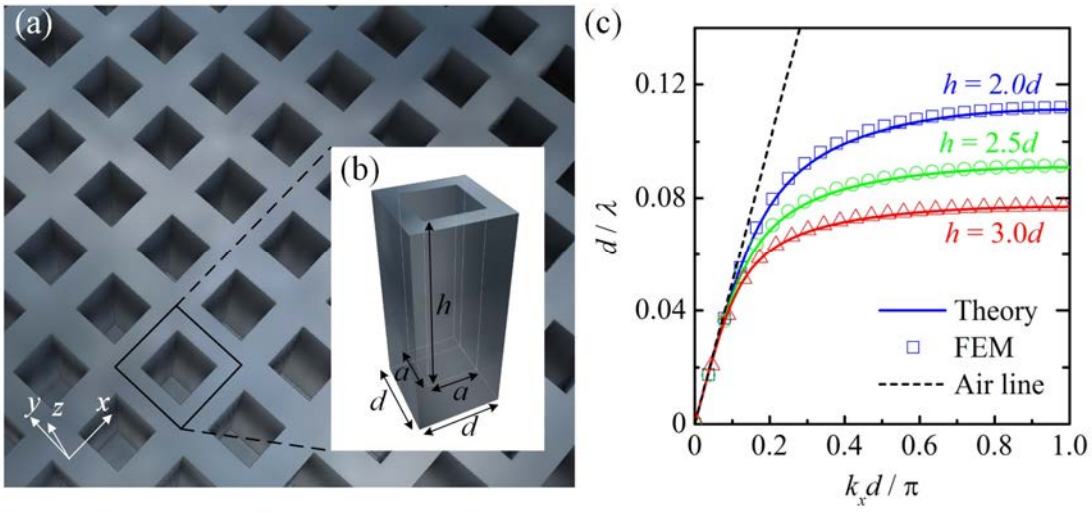

FIG. 2.1. Geometry-governed dispersion characteristics of the structure-induced surface acoustic waves. (a) Schematic illustration of the rigid surface perforated with uniform blind square holes. The lower-right inset shows the unit cell, where the side length and depth of the square hole are a and h, with lattice constant being d. (b) Dispersion curves for different hole depths ($h = 2.0 / 2.5 / 3.0d$) with $a = 0.75d$. The solid lines and symbols represent the theoretical and simulation results, respectively, while colors are used to distinguish different h. The dispersion of sound waves in free space (air) is denoted by dashed black line.

Based on Eq. (2.16), we conduct theoretical calculations to investigate the dispersion behavior of the SSAWs at perforated surfaces with uniform unit cells. The geometrical parameters are set as $d = 0.75a$ and $h = 2.0 / 2.5 / 3.0d$. The background medium is air with ρ_0=1.21 kg/m^3 and c_0=343 m/s. Finite-element-method (FEM)

simulations (see Appendix A) are also performed to confirm the theoretical model.

As presented in Fig. 2.1(b), the theoretical results (solid lines) agree excellently with the simulation results (symbols). Each dispersion curve asymptotically approaches the sound line (dashed black line) within low frequency range and tends to deviate away as frequency increases. The curves flatten at the edge of the first Brillouin zone, suggesting the vicinity of a zero-group-velocity point. Evidently, the geometrical parameters determine the curve shape and the band edge, namely, the dispersion characteristics of the surface mode. Such dispersion behavior can be well understood if ideal effective medium approximation $d \to 0$ is applied. In this case, the dispersion relation of Eq. (2.16) can be simplified into the form

$$\frac{\sqrt{q^2 - k_0^2}}{k_0} = \frac{a^2}{d^2} \tan\left(k_0 h\right), \tag{2.17}$$

which clearly shares very similar mathematical expression with the typical dispersion relation of spoof surface plasmon polaritons [90].

2.3 Acoustic rainbow trapping of controllable spatial-spectral modulation

2.3.1 Gradient holey-structured metasurface

To realize ART effect with the SSAWs, a gradually increased hole depth distribution $h(x)$ is introduced to form a gradient metasurface as shown in Figs. 2.2(a) and 2.2(b). Equivalently, it offers an adiabatic control over the dispersion of the SSAWs in space. Incident plane waves grazing the metasurface would be converted into the SSAWs travelling with slowly vanished group velocity. One may examine this from the viewpoint of effective medium approximation, in which the group velocity of the SSAWs can be directly derived based on Eq. (2.17) and associated with both the frequency and the position as

$$v_g(x,f)=\frac{1}{\mathrm{d}q/\mathrm{d}\omega}=\frac{c_0}{\sqrt{1+S^2\tan^2(k_0h(x))}+k_0h(x)S^2\dfrac{\tan^2(k_0h(x))+1}{\sqrt{\cot^2(k_0h(x))+S^2}}},\quad(2.18)$$

where $S=a^2/d^2$. As shown in Fig. 2.2(c), the group velocity is the same as that of air at $x=0$ and gradually decreases along the $+x$ direction. It ultimately approaches zero when $k_0h(x)\to\pi/2$, which denotes the trapping point. Meanwhile, this decelerating process is available over a broad bandwidth, required by ART effect.

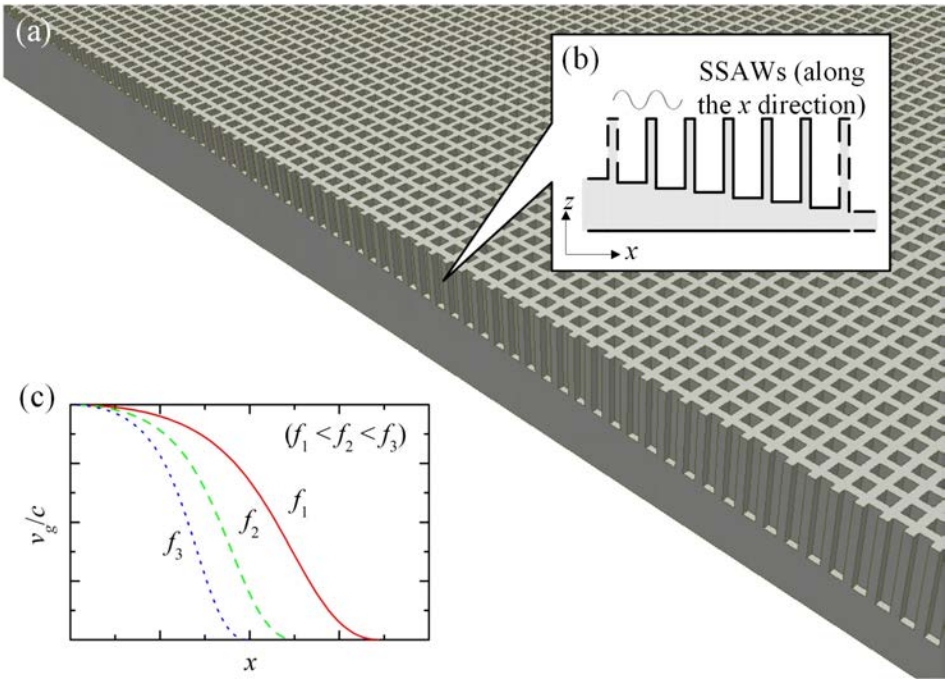

FIG. 2.2. Acoustic rainbow trapping through a gradient holey-structured metasurface. (a) Schematic illustration of the gradient holey-structured metasurface. The hole depth slowly increases along the wave propagation direction $+x$. (b) Detailed view of the structures within *xz*-plane. (c) Group velocity distribution along the wave propagation direction. Different colors and line styles denote different operating frequencies.

It should be noted that the effective medium approximation tends to be invalid at high frequency range near the edge of the first Brillouin zone, which means that the wavenumber of the SSAWs cannot be infinitely large due to the non-zero lattice constant d of a gradient metasurface constructed with actual structures. To precisely predict the where the trapping happens, the dispersion relation based on rigorous

microscopic model given by Eq. (2.16) is recalled here. Given that the *x*-component maximum momentum of the SSAWs is $k_{x,\max} = \pi / d$ instead of $+\infty$ (y-component is neglect in 1D propagation case), the equation that correlates the trapping position and the frequency can be expressed as

$$\tan(k_0 h(x)) = \frac{d^2}{a^2}\left(\sum_{r=-\infty}^{+\infty} \frac{k_0 \mathrm{sinc}^2(K_r a/2)}{\sqrt{K_r^2 - k_0^2}}\right)^{-1}, \tag{2.19}$$

where $K_r = (2r+1)\pi / d$ ($r \in \mathbb{Z}$). The left-hand side represents the local resonance inside individual holes, while the right-hand side corresponds to the mutual coupling among neighboring units via the diffracted waves. Hence Eq. (2.19) implies a balanced interplay between these two physical processes that contributes to the trapping effect.

2.3.2 Design of trapping pattern

It is also of value to investigate if one can control the spatial-spectral modulation through adjusting the gradient profile of the hole depth. In this thesis, three different gradient profiles are considered, as illustrated in Fig. 2.3(a). The first one is simply the linear hole depth profile defined as

$$h(x) = x\tan(\theta),\ x = x_0 + md,\ (m = 1,2,...,n,\ n \in \mathbb{N}), \tag{2.20}$$

in which $\theta < 5°$ is the tapering angle. For the second type, by mapping the trapping frequencies in Eq. (2.19) linearly to the hole positions, the depth profile that corresponds to the model of linear frequency trapping is written as

$$\begin{aligned} h(x) &= \frac{1}{k_0(x)}\arctan\left(\frac{d^2}{a^2}\left(\sum_{r=-\infty}^{+\infty} \frac{k_0(x)\cdot \mathrm{sinc}^2(K_r a/2)}{\sqrt{K_r^2 - k_0^2(x)}}\right)^{-1}\right), \\ k_0(x) &= \frac{2\pi f(x)}{c},\ f(x) = f_l + \frac{(f_h - f_l)}{n}\cdot\frac{(x - x_0)}{d}, \\ x &= x_0 + md,\ (m = 1,2,...,n,\ n \in \mathbb{N}), \end{aligned} \tag{2.21}$$

where f_l and f_h are the pre-designed upper and lower frequency limits, respectively. Another one that might be preferred in engineering application is the 1/48-octave-band

profile. It can also be derived by mapping the upper frequency limit of each 1/48 octave band to the required hole depth as

$$
\begin{aligned}
&h(x)=\frac{1}{k_0(x)}\arctan\left(\frac{d^2}{a^2}\left(\sum_{r=-\infty}^{+\infty}\frac{k_0(x)\cdot\mathrm{sinc}^2(K_r a/2)}{\sqrt{K_r^2-k_0^2(x)}}\right)^{-1}\right),\\
&k_0(x)=\frac{2\pi f(x)}{c},\ f(x)\in 1/48 \text{ octave bands},\\
&x=x_0+md,\ (m=\text{band number}),
\end{aligned}
\tag{2.22}
$$

in which the trapping frequencies are mapped to the upper band limits instead of the central frequencies of the 1/48 octave band since the trapping point indicates the upper cut-off within the frequency domain.

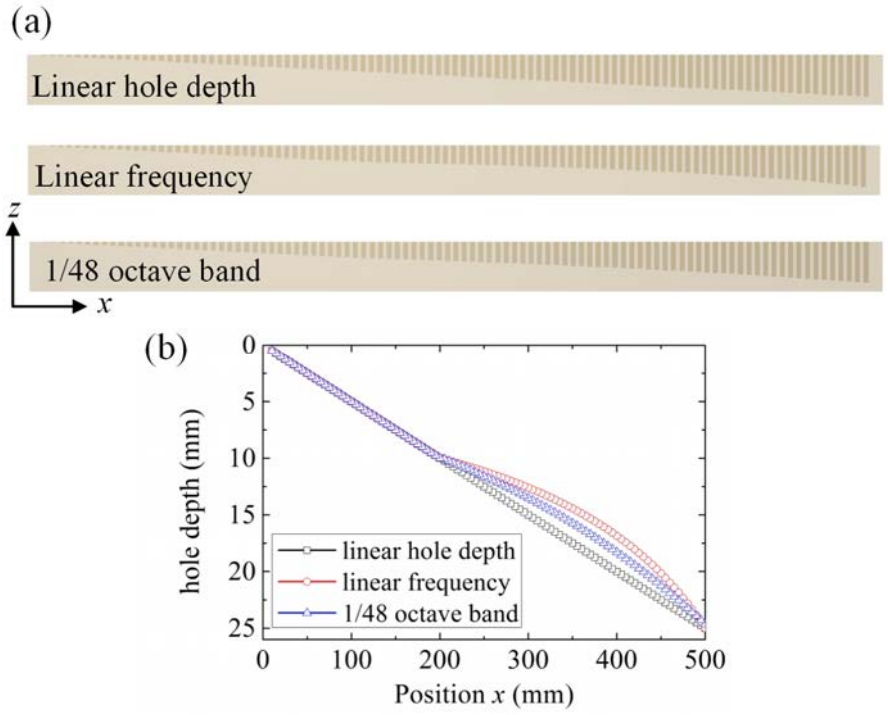

FIG. 2.3. Design of gradient hole depth profiles. (a) Schematic illustration of the three studied profiles within *xz*-plane. (b) Designed hole depth distributions along the wave propagation direction. The side length of the square hole and the period of the unit cell are set as $a=3$ mm and $d=5$ mm, respectively. The total number of unit cells is 99 in the x direction with depths ranging from 0.5 mm to 25 mm ($x\in(10,500)$ mm), among which the first 39 units ($x\in(10,200)$ mm) are with linearly distributed depths and the rests are designed using Eqs. (2.20) to (2.22).

This thesis designs three gradient metasurfaces based on Eqs. (2.20) to (2.22) to examine their effectiveness, as presented in Fig. 2.3(b). The side length of the square hole and the period of the unit cell are set as $a = 3$ mm and $d = 5$ mm, respectively. The total number of unit cells along the x direction is 99, with hole depths ranging from 0.5 mm to 25 mm. It is important to note that, for all three cases, the depths of the first 39 holes are linearly distributed. This is because, on the one hand, the trapping frequency is nearly reciprocal to the hole depths so that the depth difference between adjacent holes become extremely small at high frequencies, e.g. less than 0.1 mm, which is difficult to achieve in practice. On the other hand, the hole depth profile that increases from nearly zero value can help to minimize the impedance mismatch between background medium and the gradient metasurfaces, guaranteeing as low as reflection during the slowing down process.

2.3.3 Numerical simulation

Since the gradient profiles of the studied metasurfaces are arranged only in the wave propagation direction and periodically repeated in the transverse direction [see Fig. 2.2(a)], the problem can be simplified as one column of unit cells in the x direction together with rigid boundary conditions being applied on both sides in the y direction [104]. In other words, the simulation model becomes an array of graded holes mounted on a waveguide of open half space and width equal to the lattice constant. The geometries of the structures and other material properties are the same as those defined in Fig. 2.3(b). Plane waves of unit amplitude come from the inlet and travel along the $+x$ direction. The inlet, outlet and upper half-space are employed with perfect-matched layer (PML) to mitigate unwanted reflections. The mesh size is at most one-tenth of the smallest wavelength. All the simulations are performed in the commercial FEM software COMSOL Multiphysics.

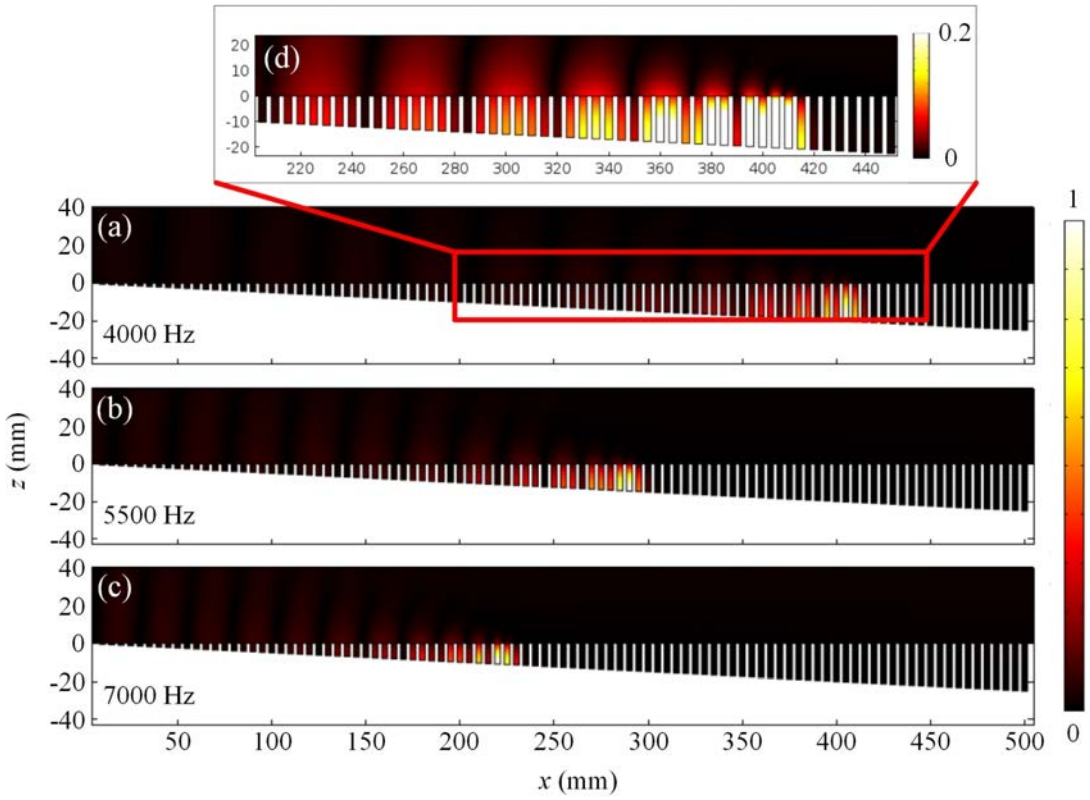

FIG. 2.4. Simulated absolute acoustic pressure fields for the linear hole-depth distribution at three different frequencies: (a) 4000 Hz; (b) 5500 Hz; (c) 7000 Hz. The pressure values in each sub-figure is normalized to the maximum value of the whole sound field. (d) Enlarged view of the absolute pressure field at 4000 Hz. The color range is rescaled from 0~1 to 0~0.2.

The simulated absolute acoustic pressure fields for the linear hole-depth distribution at three representative frequencies are presented in Fig. 2.4. These pressure fields are extracted at the symmetry plane (*xz*-plane at $y = 0$) of the simulation model. As expected, the incident plane waves are gradually converted into the SSAWs travelling along the $+x$ direction, manifested by the energy distribution confined to the metasurface near the trapping point [see Fig. 2.4(d)]. The local sound oscillations of neighboring holes are coupled with each other through the diffractions, leading to the trapping phenomenon when they reach a balance. As shown in Figs. 2.4(a)-2.4(c), incident waves of different frequencies are trapped at different horizontal positions, forming extremely enhanced sound fields. Note that this enhancement is induced by

resonance and can be very intensive without taken into consideration the inherent viscous and thermal losses. Figure 2.5 further presents the absolute acoustic pressure fields for the three types of gradient profiles at 5000 Hz. This reveals that the trapping pattern can indeed be well tailored through adjusting the gradient profile.

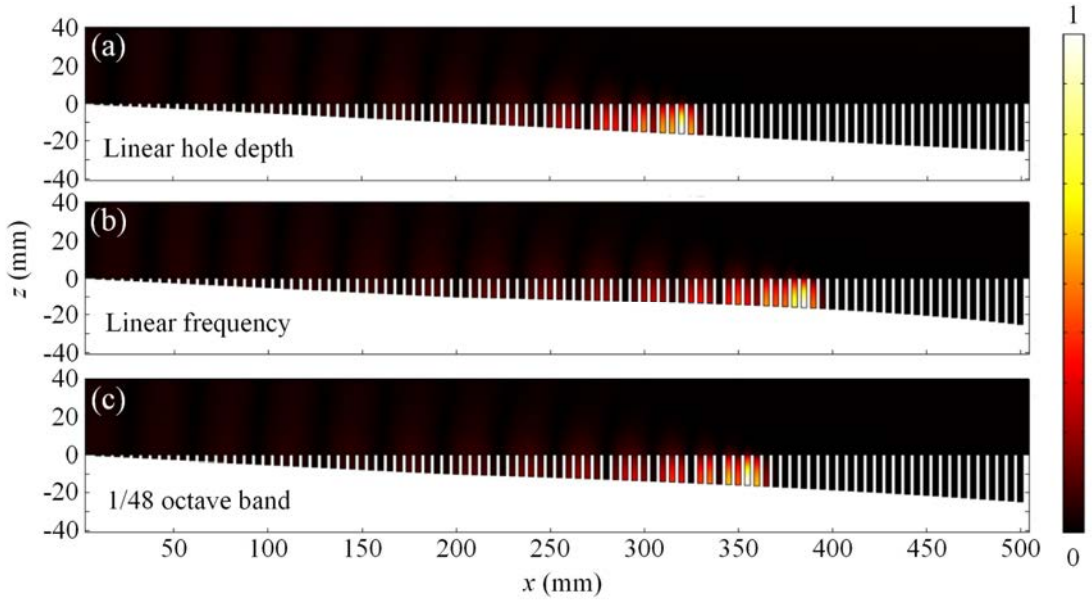

FIG. 2.5. Simulated absolute acoustic pressure fields for the three types of gradient profiles at 5000 Hz: (a) linear hole depth; (b) linear frequency; (c) 1/48 octave band. The pressure values in each sub-figure is normalized to the maximum value of the whole sound field.

For each of the studied gradient profiles, the frequency responses at the bottoms of the holes of three equally spaced horizontal positions are plotted in Figs. 2.6(a)-2.6(c). As the operating frequency increases, the acoustic pressure rises in an oscillating manner before reaching its maximum, followed by an abrupt decline. The highest peak of each curve represents the resonance of the unit cell while other peaks and valleys are results of the interference between the reflection from the trapping position and the incidence. Such resonance generates drastically enhanced sound field, with the peak value being several tens of times of the incident pressure amplitude. A clear cut-off can be observed after the highest peak, indicating the trapping frequency of the unit cell.

Note that the spatial-spectral modulation is well controlled by the gradient profiles, e.g. for every two neighboring curves of the linear frequency case [Fig. 2.6(b)], nearly equal intervals between two cut-off frequencies are prominent in the spectrum (linear coordinates), being consistent with the design in Fig. 2.3(b). As presented in Fig. 2.6(d), the correlations between horizontal position and trapping frequency are also extracted. It further demonstrates that the spatial-spectral modulation can indeed be precisely controlled by adjusting the gradient profile, which are in good agreement with the results calculated using the theoretical model given by Eq. (2.19). Such profile-governed ART effect can provide greater flexibility and adaptivity to the design of acoustic sensing and filtering devices.

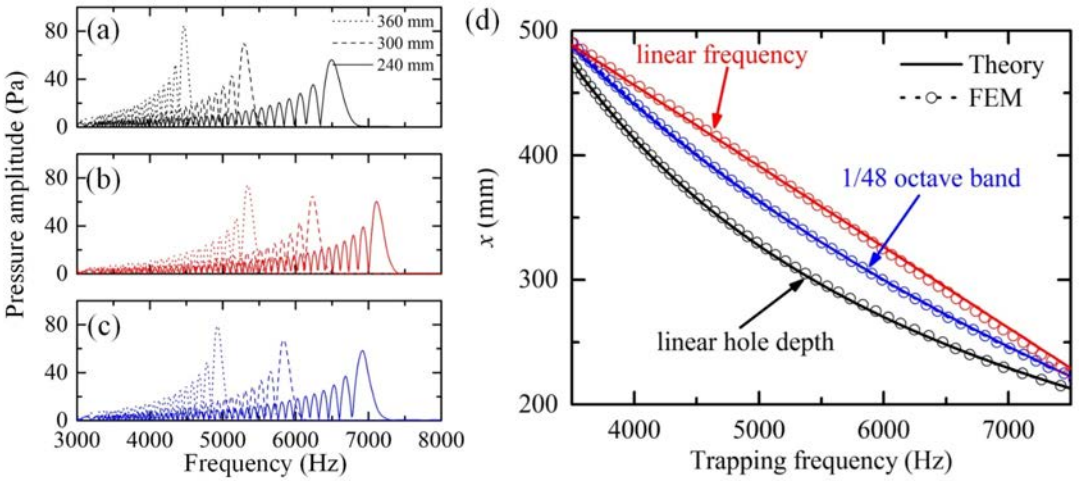

FIG. 2.6. Demonstration of the controllable spatial-spectral modulation. Frequency responses at the bottoms of the holes at three different horizontal positions: (a) linear hole depth (black); (b) linear frequency (red); (c) 1/48 octave band (blue). (d) Trapping position versus frequency for the three gradient profiles.

2.4 Inherent losses induced absorptive acoustic rainbow trapping

One may notice that, for a lossless gradient metasurface demonstrated above, the group velocity of the SSAWs cannot be slowed down to exactly zero owing to the inevitable coupling between the forward- and backward- propagating modes [65]. Consequently, the local sound oscillation eventually radiates backward rather than

being permanently trapped, despite an obvious deceleration and compression process of the propagating waves. Meanwhile, there is a growing interest in exploring the influence of inherent losses on the performance of acoustic metamaterials and metasurfaces [105-107], as well as the possibilities to utilize them to achieve functionalities such as sound absorption [107-111] and asymmetric sound transmission [112]. However, it has not been theoretically investigated how the inherent losses would affect the performance of the gradient metasurfaces for ART, which hinders their practical development.

In this section, the intrinsic viscosity and thermal conductivity within the holes of the gradient metasurface are taken into consideration. As a result, acoustic waves grazingly incident upon the lossy gradient metasurface are converted into the SSAWs with not only slowly diminished group velocity but also increased attenuation. At the trapping position, the attenuation dominates and balances with the local oscillation and the mutual units coupling. The unwanted backscattering is mitigated owing to the dissipation so that the ART effect is reflectionless. The proposed lossy gradient metasurface is a significant step towards the practical application of ART devices in r acoustic sensing and filtering, as well as artificial cochlea. It may also be utilized to design absorptive metasurfaces to delay the hypersonic boundary layer transition [80,81].

2.4.1 Effect of the inherent losses

The effect of the intrinsic losses on the SSAWs arises from the thermal and viscous boundary layers within those narrow regions of a holey-structured metasurface, which is non-trivial for resonance elements in real life [88,106,113]. Such effect can be theoretically modeled by considering the thermal conductivity κ and the viscosity μ of air inside the holes. The effective density ρ_h, the compressibility C_h, and the

wavenumber k_h inside the holes thus become complex and frequency-dependent, which are given by [114-116]

$$\begin{aligned} &\rho_h(\omega) = \rho_0 / \Psi_\nu, \quad C_h(\omega) = \frac{\gamma - (\gamma - 1)\Psi_t}{\rho_0 c_0^2}, \\ &k_h^2 = \omega^2 \rho_h(\omega) C_h(\omega) = k_0^2 \frac{\gamma - (\gamma - 1)\Psi_t}{\Psi_\nu}, \end{aligned} \tag{2.23}$$

where $\gamma = C_P / C_V$ is the ratio of the specific heat at constant pressure C_P and the specific heat at constant volume C_V. Ψ_ν and Ψ_t are functions governed by the geometry of the hole's cross-section. For rectangular holes of side lengths a and b

$$\Psi_{\mathrm{i}} = k_{\mathrm{i}}^2 \sum_{M=0}^{\infty} [(\frac{1}{\alpha_M M'})^2 (1 - \frac{\tan(\alpha_M b/2)}{\alpha_M b/2}) + (\frac{1}{\beta_M M'})^2 (1 - \frac{\tan(\beta_M a/2)}{\beta_M a/2})], \tag{2.24}$$

with

$$\begin{aligned} &\alpha_M = \sqrt{k_{\mathrm{i}}^2 - (2M'/a)^2}, \quad \beta_M = \sqrt{k_{\mathrm{i}}^2 - (2M'/b)^2}, \\ &M' = (M + \frac{1}{2})\pi, \ (M = 0, 1, 2, ...), \end{aligned} \tag{2.25}$$

and

$$k_{\mathrm{i}}^2 = \begin{cases} k_\nu^2 = -j\omega \dfrac{\rho_0}{\mu}, & \text{viscous wave number} \\ k_t^2 = -j\omega \dfrac{\rho_0 C_p}{\kappa}, & \text{thermal wave number} \end{cases}. \tag{2.26}$$

Subscript i is either ν or t that denotes the term of viscous or thermal boundary layer. The standing wave field inside the holes given by Eqs. (2.5) and (2.6) can thus be rewritten as

$$p_h = C(e^{-jk_h z} + e^{2jk_0 h} e^{jk_h z}), \tag{2.27}$$

$$v_{z,h} = \frac{k_h}{\rho_h \omega} C(e^{-jk_h z} - e^{2jk_0 h} e^{jk_h z}). \tag{2.28}$$

It is worth mentioning that the incident and reflected wave fields remain unchanged (see Section 2.2). This is because the sound attenuation in the upper half space is

negligible compared to that induced by the inherent visco-thermal losses inside the holes.

Following a similar procedure as presented in Section. 2.2 (applying the continuity conditions of both the pressure and the *z*-component particle velocity at $z = 0$), the reflection coefficient of the (m,n)-th order diffraction in the presence of the inherent losses can be obtained as [89]

$$R_{mn} = \delta_{mn,00} - \frac{2j\tan(k_h h)\dfrac{\rho_0 a^2}{\rho_h d^2} S_{00} S_{mn} \dfrac{k_h}{k_z^{(m,n)}}}{1 + j\tan(k_h h)\dfrac{\rho_0 a^2}{\rho_h d^2} \cdot \sum\limits_{r,s=-\infty}^{+\infty} \dfrac{k_h}{k_z^{(r,s)}} S_{rs}^2} \tag{2.29}$$

As we have mentioned above, a structure-induced surface mode is propagative along the parallel directions requiring $\mathrm{Re}(q) > k_0$ with $\mathrm{Re}(k_x) \geq 0$ and $\mathrm{Re}(k_y) \geq 0$. Meanwhile, it is confined to the surface so that $\mathrm{Re}(jk_z) > 0$. For the lossy case here, the propagation is with inherent attenuation, corresponding to $\mathrm{Im}(q) < 0$. Again, by setting $jk_z^{(r,s)} = \sqrt{(q^{(r,s)})^2 - k_0^2}$ and analyzing the divergences of R_{mn}, the dispersion relation of the SSAWs becomes

$$1 - k_h \tan(k_h h)\frac{\rho_0 a^2}{\rho_h d^2} \cdot \sum_{r,s=-\infty}^{+\infty} \frac{S_{rs}^2}{\sqrt{(q^{(r,s)})^2 - k_0^2}} = 0. \tag{2.30}$$

For such lossy model where ρ_h and k_h are complex, the wavenumber of the SSAWs q must be complex as well, which means the SSAWs propagate with inherent attenuation. Another important feature of the SSAWs is that they become a leaky surface mode in the presence of the inherent losses, namely, the propagation constant along the z direction $jk_z = \sqrt{q^2 - k_0^2}$ is not a purely real number anymore. Note that the surface mode radiates energy to the standing-wave mode in side holes instead of the bulk mode in the upper half space owing to the fact $\mathrm{Im}(\sqrt{q^2 - k_0^2}) < 0$. Hence, without

any leakage to the upper semi-space, the attenuation of the SSAWs completely comes from the inherent visco-thermal losses within the holes.

Theoretical calculation based on Eq. (2.30) is conducted to investigate the dispersion behavior of the SSAWs at a lossy metasurface with uniform unit cells of $a = 3$ mm , $d = 5$ mm , and $h = 25$ mm .The physical properties of air at 20 ˚C, standard atmospheric pressure, are respectively $\rho_0 = 1.21$ kg/m^3 , $c_0 = 343$ m/s , $\kappa = 0.0258$ W/m$\cdot$K , $\mu = 1.81\times10^{-5}$ kg/m$\cdot$s , $C_p = 1.005\times10^3$ J/kg$\cdot$K and $\gamma = 1.4$. Meanwhile, three-dimensional full-wave simulations using COMSOL Multiphysics are performed to examine the surface wave field above an holey-structured metasurface. 40 building blocks are arranged along the x direction to mimic a sufficiently large metasurface. Periodic boundary condition and perfectly matched layers are employed to imitate the infinitely repeated building blacks in the y direction and the semi-infinite half space $z > 0$, respectively. The inherent losses inside the holes due to thermal conductivity and viscosity are numerically considered via replacing the purely real properties with those complex ones given in Eq. (2.23). To effectively excite the surface mode [79,83,86,99], a line source is applied near the inlet of the metasurface, namely, a near field excitation technique. The mesh size is at most one-tenth of the smallest wavelength.

As shown in Fig. 2.7(a), the real part of the dispersion curve of the lossy metasurface (red solid line) overlaps with those of the lossless case (blue solid line) and the background medium (black solid line). It gradually deviates from the sound cone (black solid line) as frequency rises while remaining similar to the lossless case. A increased imaginary part is observable (red dashed line), representing the attenuation of the SSAWs, as illustrated by the simulated sound field in Fig. 2.7(b) and 2.7(c). It is worth noting that for the lossy case, the dispersion curve of the SSAWs cannot touch

the edge of the first Brillouin zone, namely, the maximum real part of the wave vector $\mathrm{Re}(k_x)$ is not π/d any more. This interesting result clearly differes from the lossless case, in which k_x is a purely real number within the first band and increases with frequency and reaches its maximum at the zone edge ($k_x \to \pi/d$). It is also different from the case studied in Ref. [88]: a lossy metasurface with relatively shorter holes still permits $\mathrm{Re}(k_x)$ to reach the zone edge, although similar attenuation behavior of the SSAWs can be observed. Here in our case, there exists a turning point in the dispersion curve [the peak of the red solid line in Fig. 2.7(a)], which represents the infinite-group-velocity $v_g = \mathrm{d}\omega/\mathrm{d}k \to \infty$. As pointed out by Ref. [117], the group velocity in a lossy medium becomes abnormal (e.g. infinite or negative) for the frequency at which the attenuation is maximum. Since the attenuation of the SSAWs completely results from the inherent thermal and viscous losses, such group velocity anomaly suggests that the turning point is where the absorption of the SSAWs reaches its maximum. As shown in Fig. 2.7(e), the SSAW mode is still propagative, but suffers severe attenuation stemming from the inherent absorption, which is in stark contrast to the result of lossless model as presented in Fig. 2.7(d). Beyond this group velocity anomaly, the imaginary part of the wavenumber is much larger than the corresponding real part, leading to the pseudo-stopband of the SSAWs. Accordingly, the surface mode can no longer be excited and the pressure oscillation is almost all confined to the source region, as rendered in Figs. 2.7(f) and 2.7(g). Whereas in lossless case, the wavenumber is purely imaginary within the bandgap.

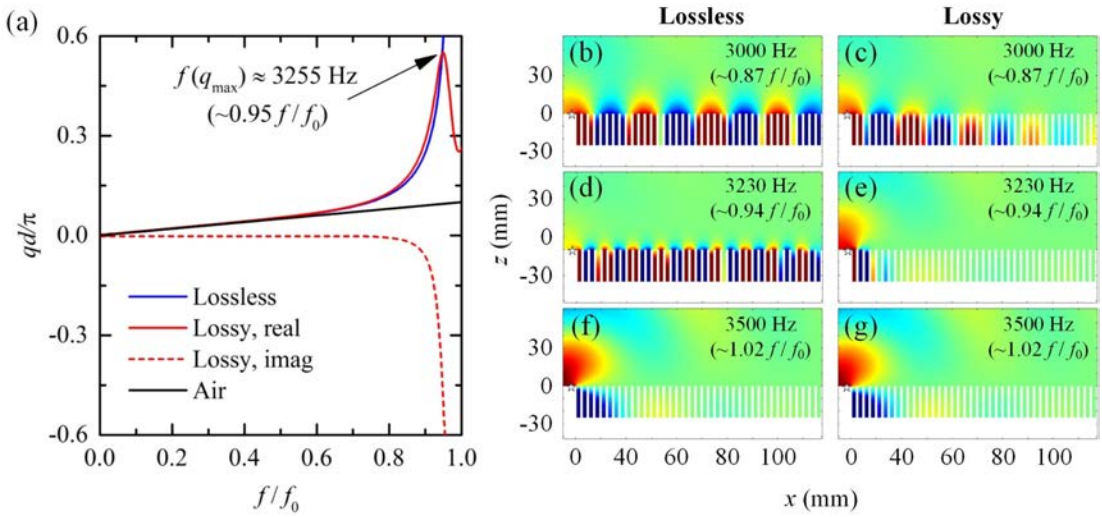

FIG. 2.7. Dispersion properties of the structure-induced surface acoustic waves at the metasurfaces with and without inherent losses [89]. (a) Calculated dispersion relation of the SSAWs. The curves of the lossless case (blue solid line) and the air line (black solid line) are also presented, where $f_0 = c_0/4h$ is the cavity resonance frequency. The unit cell is designed to have $a = 3$ mm, $d = 5$ mm and $h = 25$ mm. (b)-(g) Simulated acoustic pressure fields at three different frequencies for both lossless and lossy cases. The star in each subfigure represents a line source that is applied near the edge of the metasurface and infinitely extended in the y direction.

2.4.2 Lossy gradient metasurface model

As depicted in Fig. 2.8(a), the hole depth distribution is also arranged in a graded way along the wave propagation direction. In this case, a gradient metasurface is constructed, which consists of 99 holes with depth varying (0.25-mm step) from 0.5 mm to 25 mm. Other properties remain unchanged as those given in previous sections. The local dispersion curves of different types of building blocks (different hole depths) are combined to create the spatial distributions of both the group velocity and attenuation. As shown in Fig. 2.8(b), for any given frequency within the designed band, the group velocity (solid lines) drops from that of airborne sound in free space to a non-zero minimum. These curves then abruptly turn to infinities, manifesting that the absorption of this lossy system reaches maximum [117]. Such frequency-dependent

group velocity distribution would contribute to a reflectionless spatial-spectral separation. Therefore, the metasurface can act as an absorptive structure, mimicking a "permanently" trapped rainbow. The quote mark is used to distinguish this trapping phenomenon from the ideal ART model built that can actually diminish the group velocity to exactly zero.

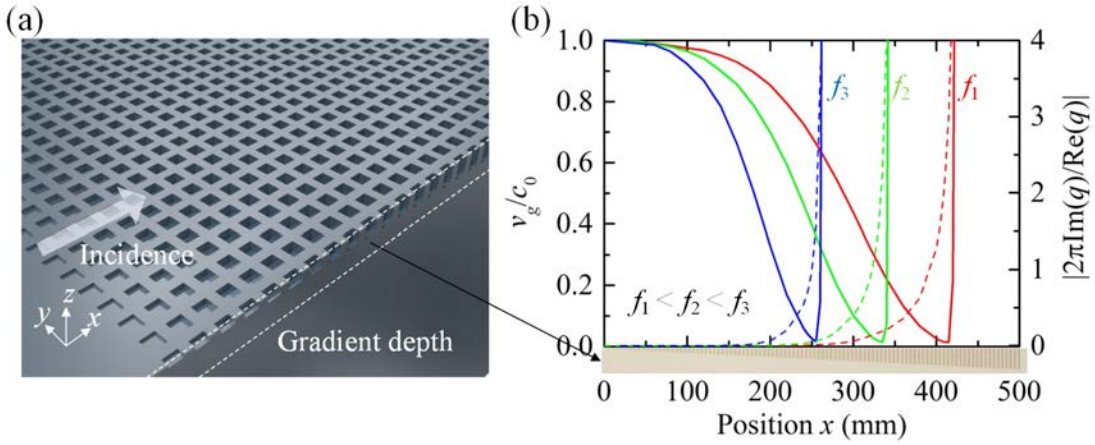

FIG. 2.8. Absorptive acoustic rainbow trapping with a gradient metasurface [89]. (a) Schematic illustration of the gradient metasurface. It consists of 99 graded square holes, whose depth linearly varied from 0.5 mm to 25 mm with a step 0.25 mm. (b) Group velocity and specific attenuation of the SSAWs along the gradient metasurface. The solid lines denote the group velocity and the dashed lines the absolute value of the specific attenuation (attenuation per wavelength). Red, green and blue represent three different frequencies $f_1 = 3860$ Hz, $f_2 = 4730$ Hz and $f_3 = 6110$ Hz. The group velocity anomaly (infinite) implies the maximum absorption of the lossy system [117].

2.4.3 Numerical simulation

Full-wave FEM simulations are conducted to test the designed model. The settings are the same as those we used in the metasurface of uniform holes except that plane incident acoustic wave from the left-hand side grazes the gradient metasurface [Fig. 2.9(a)].

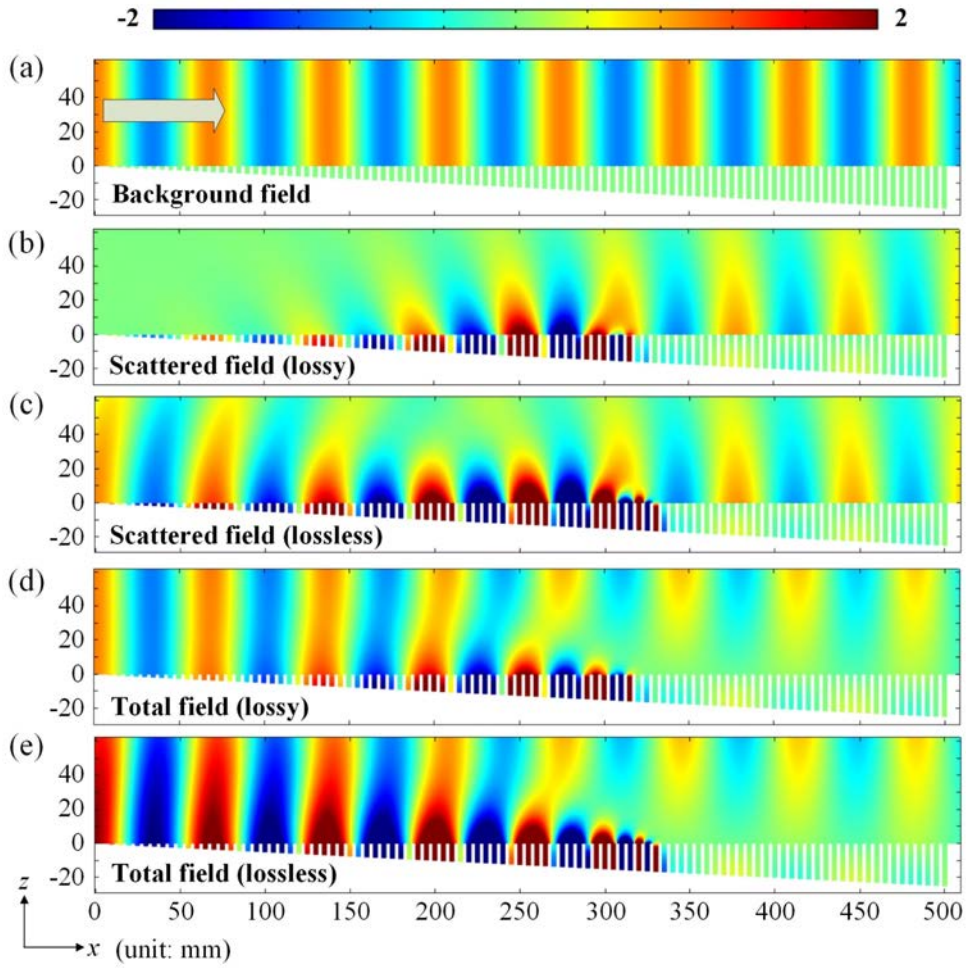

FIG. 2.9. Comparison of simulated acoustic pressure fields of lossy and lossless models at 5000 Hz [89]. (a) Background acoustic pressure field. The incident plane wave of unit amplitude travels from the left-hand side to the right-hand side. (b)-(e) scattered and total acoustic pressure fields of lossy and lossless models. The upper and lower limits of the acoustic pressure are set to two times the amplitude of the incident wave to guarantee that the wave pattern above the gradient metasurface is clear enough.

It can be seen from the scattered and total acoustic pressure fields [Figs. 2.9(b) to 2.9(d)] that the incident wave near the surface is efficiently converted into the SSAWs. They are confined to the surface and their wavelength are highly compressed, which forms strongly enhanced sound field. The maximum compression appears at the trapping position where the SSAWs cannot transmit further so that the near-surface sound field beyond this position is rather weak. Incident waves further away from the metasurface cannot interact with the structures and thus continue to propagate with

hardly any change in the shape of wavefront. For lossless case as shown in Figs. 2.9(c) and 2.9(e), the deceleration of the SSAWs is restricted by the non-zero group velocity subject to intermodal coupling between the forward and backward modes [65]. Hence the trapping is only temporarily achieved and the SSAWs eventually radiates back to the half space. In contrast, no obvious backscattering takes places in the lossy model [Figs. 2.9(b) and 2.9(d)], leading to reflectionless spatial-spectral modulation, namely a so-called absorptive trapping effect. Basically, two facts contribute to the reflectionlessness behavior: first, the mode conversion between the incident wave and the surface mode is in an adiabatic manner due to the gradient distribution of group velocity that slowly drops from that of airborne sound in free space to the vicinity of zero, with little mismatch during the propagation; secondly, the attenuation of the SSAWs also gradually increases and becomes dominant at the trapping position so that the backward mode is nearly fully absorbed. It shows that the inherent thermal and viscous losses can help to rebuild the balanced interpaly between the local sound oscillation and the mutual interaction [71].

The simulated total acoustic pressure fields and the corresponding absolute values at several different frequencies in the presence of losses are displayed in Fig. 2.10. The operating frequency increases linearly from Figs. 2.10(a) and 2.10(e) to Figs. 2.10(d) and 2.10(f). Incident waves of different frequencies are compressed and slowed down in different manners, depending on the spatial group velocity distributions shown in Fig. 2.8(b). The trapping takes place at deeper holes for lower frequencies and at shallower holes for higher frequencies, which are determined by the group velocity anomaly points in space. The whole process is accompanied by very weak backscattering. Else clear interference patterns would appear on the left-hand side of the absolute acoustic pressure fields [Figs. 2.10(e)-2.10(h)]. The overall phenomenon well meets our

theoretical expectation, which confirms that the ART effect previously investigated in lossless system [71] is still valid even in the presence of inherent visco-thermal losses, an important effect cannot be neglected in real life.

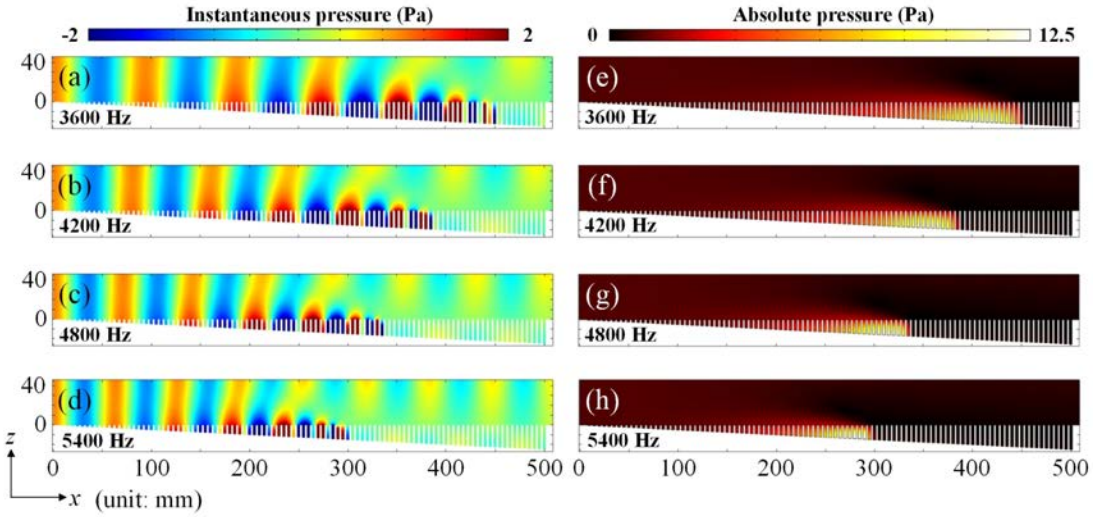

FIG. 2.10. Simulated total acoustic pressure fields and the corresponding absolute values at several different frequencies in the presence of losses [89]. (a)-(d) Total acoustic pressure fields. The upper and lower limits of the acoustic pressure are set to two times the amplitude of the incident wave to guarantee that the wave pattern above the gradient metasurface is clear enough. (e)-(h) Absolute total acoustic pressure fields. The pressure amplitudes are normalized per the maximum among the results of the four frequencies.

Figures 2.11(a) and 2.11(b) present the frequency responses at the hole bottoms of four different horizontal positions. Compared to the results of lossless case [dashed lines in Fig. 2.11(a)], the oscillatory rise of pressure amplitude with respect to frequency is smoothed due to the vanished reflection. The enhancement of sound field, albeit weakened by the dissipations, still produces pressure amplitude more than ten times over that of the background field. In each curve of Fig. 2.11(a), the rapid decline of pressure amplitude after the peak shows a clear cutoff, signifying the so-called trapping frequency. From the lossless model (solid curves) to lossy model (dashed curves), these trapping points shift slightly towards low frequency range. This phenomenon can be

well understood by the examining the change in propagation characteristics of the SSAWs brought by the inherent losses: the losses lead to complex effective wavenumber k_h and lower speed of sound inside the holes, which slightly reduces the resonance frequency [106,107]; since the SSAWs is a result of the interaction between the local resonance and the mutual coupling via diffractions, such change in resonance behavior subsequently has an impact on the propagation characteristics of the SSAWs. This low-frequency shift is consistent with our theoretical prediction, as evidenced by the extracted trapping curves [Fig. 2.11(c)], in which the lossy model undoubtedly offers a more accurate estimation. It also provides a theoretical explanation to the deviation of the measured results from the lossless model in Ref. [71].

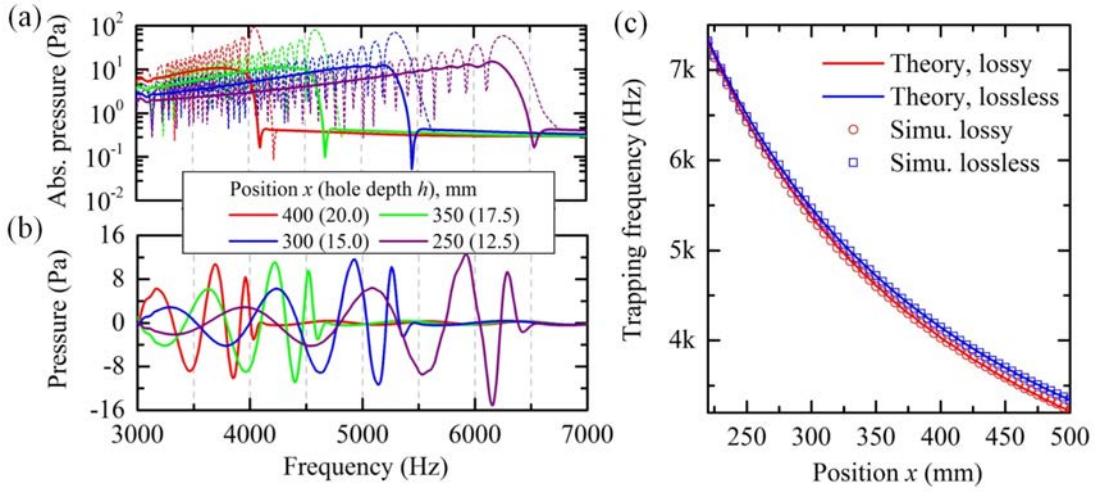

FIG. 2.11. Simulated frequency responses at the hole bottoms of four different horizontal positions and the extracted trapping curves [89]. (a) Absolute acoustic pressure versus frequency. The results of lossless case are shown with dashed lines. (b) Instantaneous acoustic pressure versus frequency. In (a) and (b), different colors denote different horizontal positions. (c) Extracted trapping frequency versus position. The red and blue solid lines represent the theoretical calculations of lossy and lossless cases; circles and squares correspond to the simulation results of lossy and lossless cases.

The backscattering is further evaluated by examining the scattered pressure amplitude $\mathrm{abs}(p_{\mathrm{scat}})$ at several different heights near the inlet. As shown in Fig. 2.12,

the backscattering generated by the metaurface is rather weak throughout the studied frequency range, which indicates that the sound waves are truly trapped and absorbed inside the gradient metasurface. On the contrary, the lossless metasurface generates strong backscattering [dashed lines in Fig. 2.12] within the same frequency band, resulting from the intermodal coupling between the forward and backward modes. At higher frequencies, the attenuation of the surface mode offered by the lossy metasurface becomes smaller because of the decreased inherent losses inside the holes, giving rise to gradually emerged (yet still much weaker than the lossless case) backscattering. Note that in lossless case the reduced backscattering for higher frequencies originates from the weakened interaction between the incident wave and the structured surface. This is due to the fact that less building blocks participate into the deceleration process at high frequencies. The large contrast between the lossy and lossless cases confirms that the phenomenon presented in Figs. 2.9 and 2.10 is valid for a broad frequency range. Clearly, the inherent thermal and viscous losses play a key role to realize the absorptive ART, leading to the reflectionless spatial-spectral splitting and sound field enhancement.

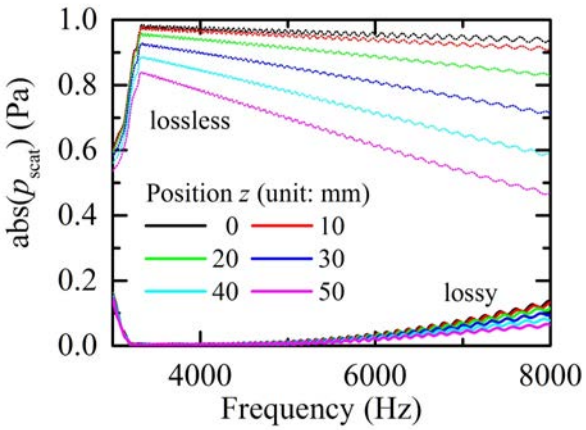

FIG. 2.12. Scattered acoustic pressure amplitudes versus frequency within upper half space at $x = 0$ [89]. Different colors represent different heights away from the metasurface. The solid and dashed lines denote lossy and lossless cases, respectively.

Fundamentally, the structure-induced surface mode is a result of the interplay

between the local oscillation inside individual holes and the mutual coupling among adjacent units. It forces the acoustic wave to go inside and outside the holes and transmit among the units through diffractions. For lossless case, the local oscillation experiences a process of periodic storage and release of energy subject to the operating frequency and strikes a balance with the mutual coupling at the resonance frequency [71]. While for lossy case, the losses within the holes participate in the process and dissipate energy into heat. Such dissipation effect slowly becomes stronger along the direction where hole depth increases, namely, along the wave propagation direction. At the trapping position, the local oscillation reaches resonance and the dissipation dominates, resulting in strong absorption of the surface mode. Therefore, the fundamental reason to absorb the SSAWs is the resonance behavior change of the holes due to the inherent losses, together with the spatial modulation of the SSAWs offered by the gradient distribution of these building blocks in space.

2.5 Summary

In summary, this chapter has demonstrated that, by carefully adjusting the gradient profile, the pattern of ART effect can be well tailored on demand. Three different profiles have been numerically evaluated. The simulation results show that broadband incident acoustic waves travelling along the holey-structured metasurfaces are effectively converted into the SSAWs. Such airborne surface mode is gradually slowed down until ultimately trapped at a specific position determined by both the operating frequency and the gradient profile, forming spatial-spectrally modulated and intensively enhanced sound field. The profile-controlled ART can provide greater flexibility and adaptivity to the design of acoustic devices for sensing, filtering and detection.

The inherent losses induced by viscosity and thermal conductivity inside the holes

are further taken into consideration, which introduces both gradually diminished group velocity and progressively increased attenuation of the SSAWs along the lossy metasurface. The resultant group velocity anomalies at the trapping position leads to spatial-spectral separation with vanished backscattering, namely, a so-called absorptive ART effect. This study deepens the understanding of the SSAWs at a lossy metasurface and is a significant step towards the practical introduction of ART-based devices. It may also provide theoretical support to the study of absorptive metasurfaces to stabilize hypersonic boundary layers [80,81].

Chapter 3:

Subwavelength focusing/imaging along a gradient-index metasurface

3.1 Introduction

Diffraction effects fundamentally limit the spatial resolution of an imaging system or the minimum focal spot size to about half the wavelength, due to the fact that near-field evanescent waves carrying rich sub-wavelength information decay exponentially outside the object/source region. There has long been a desire to overcome this barrier as sub-diffraction-limited techniques would benefit a wide variety of applications, for example, specific to acoustics-related fields, ranging from seismic exploration and sonic well logging, to ultrasonic non-destructive evaluation, to ultrasonic biomedical imaging and therapy. In essence, the so-called diffraction limit is a fundamental restriction of nature that cannot be really violated. As highlighted by Ref. [118], people can only circumvent it and get better resolution through the loopholes in the theory. The emergence of metamaterials opens up the possibilities to go into such loopholes, by providing exotic properties and unconventional functionalities beyond what nature offers. Stimulated by the concepts of superlens and hyperlens in optics [5,119-122], acoustic metamaterials with negative index/density [19,29,31,123-125] or extremely anisotropic density [20-22,24,25,28,126-128] have been reported to circumvent the diffraction limit, through amplifying the evanescent waves or converting/magnifying them to propagating modes inside/outside the metamaterials. An alternative strategy is the time-reversal mirrors combined with an acoustic sink or a resonators array [30,129], which allows flexible control of sound field and recovery of evanescent waves based on an inversion procedure. It has also been shown recently that, by carefully designing the plane wave bandgap and the trapped resonances of an acoustic metamaterial within the same band, low spatial frequency components can be filtered so that only

evanescent waves are utilized to create the edge-based image with sub-diffraction resolution [32]. However, despite these exciting advances, only a few studies have achieved subwavelength focusing effect. Successful proposals that have been verified by experiment either rely on additional time-reversal techniques [30,129], or require the sound source to be closely attached to the lens [19,130]. Although Maznev, *et al.* have pointed out that time-reversal technique is not the unique factor that contributes to the sharp focal spot [98,131], it still plays an important role in controlling over the focusing process. More importantly, the capability to focus plane acoustic waves into a subwavelength hot spot, which corresponds to the Fourier transform function essential for many imaging systems, has not been demonstrated so far.

The structure-induced surface acoustic waves (SSAWs) guided by periodically structured surfaces bring new possibilities to the subwavelength manipulation of airborne sound due to the high spatial-frequency feature and the confined sound field that is open to the environment. The subwavelength feature of SSAW can be well understood from the dispersion relation $k_{\parallel}^2 + k_{\perp}^2 = k_0^2$, where $k_{\parallel}$ is the in-plane wave wavevector, $k_{\perp}$ is out-of-plane wave wavevector, and k_0 is the wavenumber of airborne sound in free space. For the SSAW, $k_{\perp}$ is an imaginary number as the surface mode is evanescent along the vertical direction, and thus $k_{\parallel}$ must be larger than k_0, which means that the SSAW has wavelength smaller than that in free space and can carry subwavelength information. Moreover, as has been discussed in Chapter 2, the dispersion behavior of such airborne surface acoustic mode is governed by the geometrical parameters of the periodical structures and can be engineered to provide various effective properties.

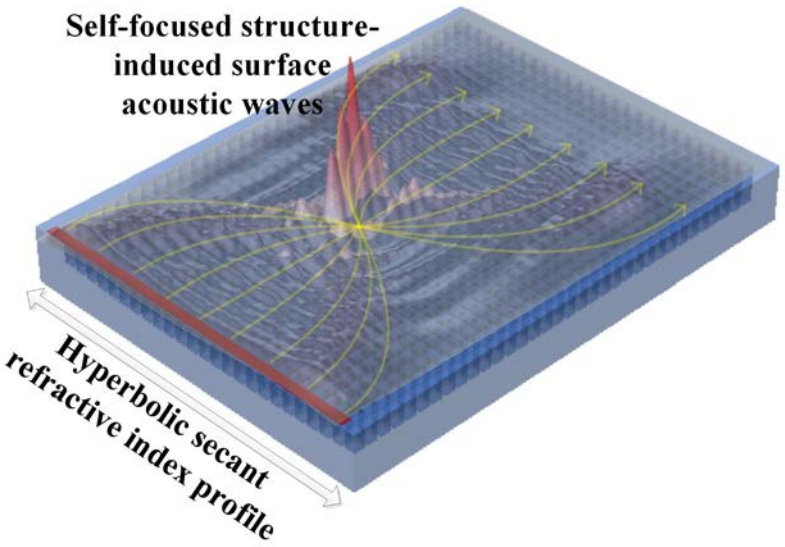

FIG. 3.1. Conceptual illustration of the gradient-index (GRIN) metasurface and the self-focused surface waves. The GRIN metasurface offers a hyperbolic secant refractive index profile to the structure-induced surface acoustic waves along the transverse direction. The yellow lines denote the trajectories of the incident plane waves.

Inspired by the unique properties of the SSAWs, this chapter presents a design approach of gradient-index (GRIN) metasurfaces to manipulate airborne sound on subwavelength scale. Different from previous study [97], the depth of the unit cell holes is utilized as a unique and direct variable to control the GRIN profile. It permits a large tunable range of the effective refractive index, and the relation between the hole depth and the refractive index can be analytically built in an explicit expression, which greatly simplifies the design process. The effectiveness of the proposed design approach is numerically and experimentally examined by considering a hyperbolic secant index profile [132-134]. As conceptually illustrated in Fig. 3.1, the GRIN metasurface is able to support self-focused SSAWs converted from incident plane waves. A focal spot with a full width at half maximum (FWHM) less than 1/7 of the wavelength in air is successfully achieved. With the same configuration, subwavelength imaging is also experimentally realized, through coupling the non-propagative evanescent field of the

source into the travelling SSAWs with large wave vectors. We then go a step further to extend the imaging into two dimensions by performing a scanning of the object plane in the third direction and synthesizing all the acquired energy density distributions. The proposed design approach offers a simple and direct way to the subwavelength manipulation of airborne sound with GRIN metasurfaces, which may facilitate the development of novel acoustic devices for focusing, imaging and sensing, etc.

3.2 Gradient-index metasurface

3.2.1 Mapping relation

We recall Eq. (2.16) obtained in Section 2.2 that describes the dispersion characteristics of the SSAWs travelling along a lossless holey-structured surface as depicted in Fig. 3.2(a):

$$1-k_0\tan(k_0h)\frac{a^2}{d^2}\cdot\sum_{m,n=-\infty}^{+\infty}\frac{S_{mn}^2}{\sqrt{(q^{(m,n)})^2-k_0^2}}=0, \tag{3.1}$$

where $q=\sqrt{k_x^2+k_y^2}$ is the Bloch wave vector of the SSAWs in the first Brillouin zone. In addition to what has been discussed in Section 2.2, the propagation characteristics of the SSAWs along all possible directions within the *xy*-plane are further investigated here. Figures 3.2(b) and 3.2(c) present the calculated and simulated dispersion curves of several different geometrical parameters along the high symmetry orientations of a square lattice [inset of Fig. 3.2(a)]. During the calculation/simulation, the density and the speed of sound are set as $\rho_0=1.21\ \text{kg/m}^3$ and $c_0=343\ \text{m/s}$, respectively. The numerical simulations are performed in commercial finite-element-method (FEM) solver COMSOL Multiphysics (see Appendix A). Typical dispersion behavior of the SSAWs can be observed: the dispersion curves asymptotically approach the air line (dashed line) at very low frequency range and start to deviate below the "sound cone"

with the increase of frequency until becoming flat at the edge of the first Brillouin zone. Evidently, the geometrical parameters determine the curve shape and the band edge, namely, the propagation characteristics of the surface mode. For large h/d value, the band edge appears in low frequency regime, indicating that subwavelength manipulation of airborne sound is possible. It should be noted that the difference between the wave vectors in the ΓX and the ΓM orientations gradually emerges as the frequency approaches the edge of the first Brillouin zone, leading to directional effective properties (non-circular equifrequency contour) and a narrow partial bandgap at even higher frequencies [96].

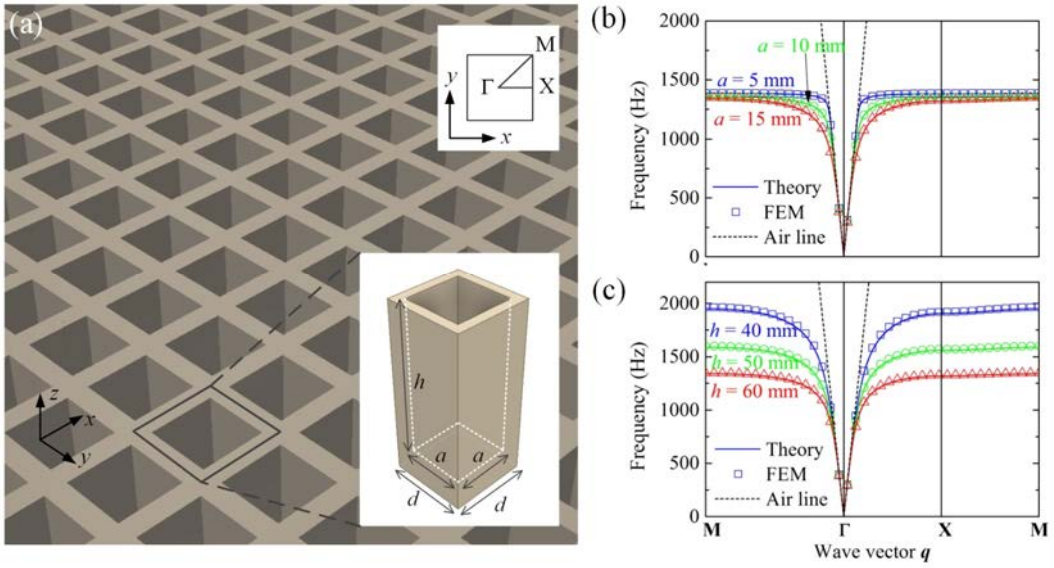

FIG. 3.2. Geometry-governed dispersion characteristics of the structure-induced surface acoustic waves. (a) Schematic illustration of the metasurface perforated with uniform square holes. The lower-right and the upper-right insets are the unit cell and the corresponding first Brillouin zone. (b) Dispersion curves for different side lengths ($a = 5,\ 10,\ 15$ mm) with fixed hole depth $h = 60$ mm and lattice constant $d = 20$ mm. (c) Dispersion curves for different hole depths ($h = 40,\ 50,\ 60$ mm) with fixed side length $a = 15$ mm and lattice constant $d = 20$ mm. The solid lines and symbols represent the theoretical and simulation results, respectively, while colors are used to distinguish different a or h. The dispersion of sound waves in free space filled with air is denoted by dashed black line.

Based on the dispersion relation Eq. (3.1), this thesis then attempts to build a straightforward mapping relationship between the geometrical parameters and the effective refractive index $n_{eff} = q / k_0$. Note that the maximum effective indices along the high symmetry orientations ΓX and ΓM are $n_{\Gamma X,\max} = \lambda / 2d$ and $n_{\Gamma M,\max} = \lambda / \sqrt{2}d$, respectively, where λ is the wavelength in air. It suggests to what degree the SSAWs can be compressed and the highest spatial frequency can be achieved, theoretically. However, as the difference between the effective refractive indices $n_{\Gamma X}$ and $n_{\Gamma M}$ becomes non-negligible near the edge of the first Brillouin zone, here we focus on the frequency range slightly away from the band edge. In this case, the approximation $n_{eff} \approx n_{\Gamma X} \approx n_{\Gamma M}$ is valid and hence Eq. (3.1) can be rewritten as

$$h = \frac{1}{k_0}\arctan\left(\frac{1}{k_0}\frac{d^2}{a^2}\left(\sum_{m,n=-\infty}^{+\infty}\frac{\operatorname{sinc}^2(K_m a/2)\operatorname{sinc}^2\left(K_n a/2\right)}{\sqrt{K_m^2+K_n^2-k_0^2}}\right)^{-1}\right), \tag{3.2}$$

where $K_m = \frac{\sqrt{2}}{2}n_{eff}k_0 + \frac{2\pi m}{d}$ and $K_n = \frac{\sqrt{2}}{2}n_{eff}k_0 + \frac{2\pi n}{d}$. Clearly, Eq. (3.2) provides a direct mapping relation between the effective refractive index and the hole depth. In other words, it is able to unequivocally determine the required hole depth for any desired refractive index ($n_{eff} \geq 1$) at a given frequency if a and d are fixed. This treatment largely reduces the complexity of design process, especially when the uniform distribution of refractive index is further changed into a GRIN manner. To the best of our knowledge, in order to obtain the target refractive index profile with large adjustable range (e.g. the maximum n_{eff} is several times larger than that of air), most GRIN design had to rely on time-consuming parametric sweep, during which a series of numerical calculations need to be performed before one can finally determine the required geometrical parameters.

3.2.2 Gradient-index design

The design principle of a planar GRIN lens that is able to focus incident plane acoustic waves can be summarized as to construct a specific refractive index profile along the transverse direction. Let x and y be the propagating and transverse directions, respectively. Here this thesis considers the hyperbolic secant refractive index distribution that has been widely used [132-134], namely, $n(y) = n_0 \,\mathrm{sech}(\alpha y)$, where n_0 is the refractive index at the center axis $y = 0$ (also the maximum value) and α is the gradient coefficient. As has been illustrated in Fig. 3.1, a planar incident beam travelling along the x direction would gradually converge towards the central axis until being focused into a small spot; the converged sound waves will then be redirected to parallel beams. The trajectory follows a sinusoidal path and the focal length is analytically given by $L_{\mathrm{focal}} = \pi/2\alpha$.

With the mapping correlation Eq. (3.2), the uniform distribution of hole depth is modified into a graded way [Figs. 3.3(a) and 3.3(b)], forming a 19×25-elements GRIN metasurface that enables the SSAWs focusing, to numerically and experimentally examine the proposed design approach. The side length of the holes and the lattice constant are $a = 15$ mm and $d = 20$ mm, respectively; the transverse spatial distribution of hole depth as a function of y is presented in Fig. 3.3(c), with the deepest ones that locate at the central axis $y = 0$ being $h\big|_{y=0} = 60$ mm. Such arrangement is directly determined using Eq. (3.2) according to the refractive index profile of $n_0 = 3.13$ and $\alpha \approx 8.27$ [Fig. 3.3(d)], in which the operating frequency and the designed focal length are $f = 1250$ Hz and $L_{\mathrm{focal}} = 190$ mm, respectively. The corresponding local dispersion relations of these individual unit cells are plotted in Fig. 3.3(e). The hole depth can well tailor the shape of the curves and thus introduces a

graded distribution of effective refractive index as shown in Fig. 2.3(d). Along the x direction, a total of 25 columns of unit cells ($0 \le x \le 500$ mm) are sufficient to fully demonstrate the converged and redirected sound field.

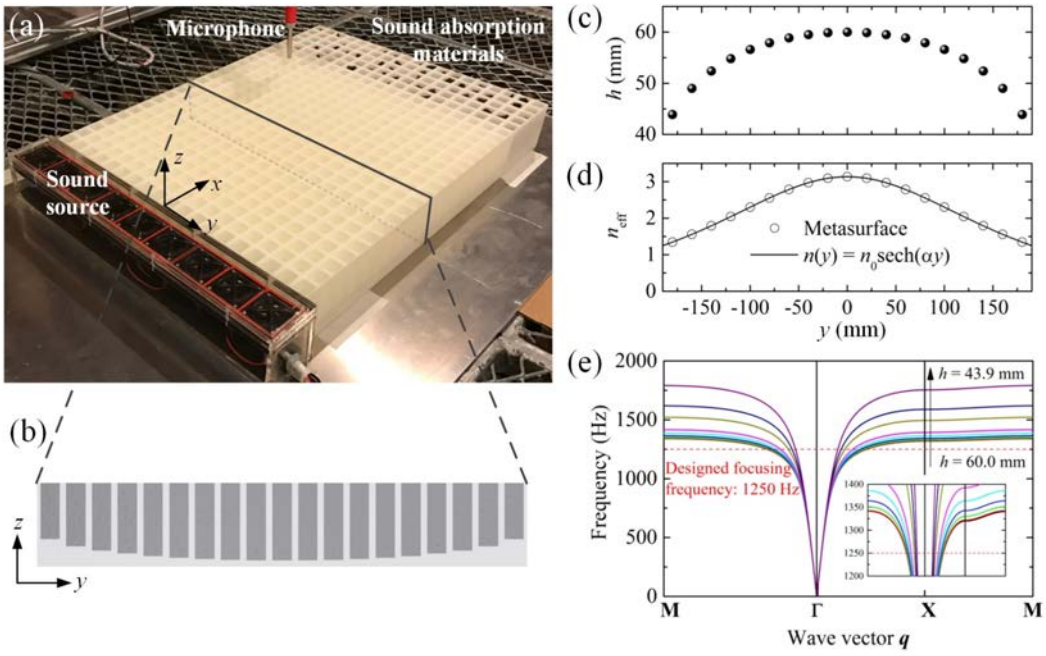

FIG. 3.3. Design of the gradient-index metasurface. (a) Photograph of the metasurface sample and the experimental setup. (b) Schematic illustration of the graded square holes in the yz-plane. (c) Hole depth distribution along the y direction. (d) Effective refractive index distribution at 1250 Hz along the y direction. The solid line is the exact hyperbolic secant index profile of our design, in which $n_0 = 3.13$ and $\alpha = 8.27$, corresponding to a focal length of $L_{\text{focal}} = 190$ mm. (e) Local dispersion curves of the unit cells used in our design. Different colors denote different hole depths ranging from 43.9 mm to 60.0 mm. The inset is a zoomed plot of the curves around 1250 Hz.

3.2.3 Effect of the inherent losses

An important factor that cannot be neglected in practice is the inherent thermal and viscous losses inside the narrow regions, as has been illustrated in Section 2.4. As shown in Fig. 3.4(a), in the presence of these losses, the real part of the wavenumber (red solid line) gradually deviates from the lossless dispersion curve (black solid line) while the imaginary part (blue dashed line) progressively increases as the frequency

rises and approaches the band edge, resulting in slightly raised effective refractive index and obvious attenuation along the wave propagation direction [88,89]. To alleviate this impact, larger hole opening a and relatively lower operating frequency away from the band edge have been selected in our design, where an inevitable tradeoff between high refractive index and low attenuation should be taken into account. It is worth mentioning that the effect of the visco-thermal losses may be theoretically included in the dispersion relation Eq. (3.1) by considering complex effective properties inside the holes [89]. However, this modified dispersion relation, albeit more precise, becomes a complex transcendental equation, and an explicit expression like Eq. (3.2) cannot be derived any more.

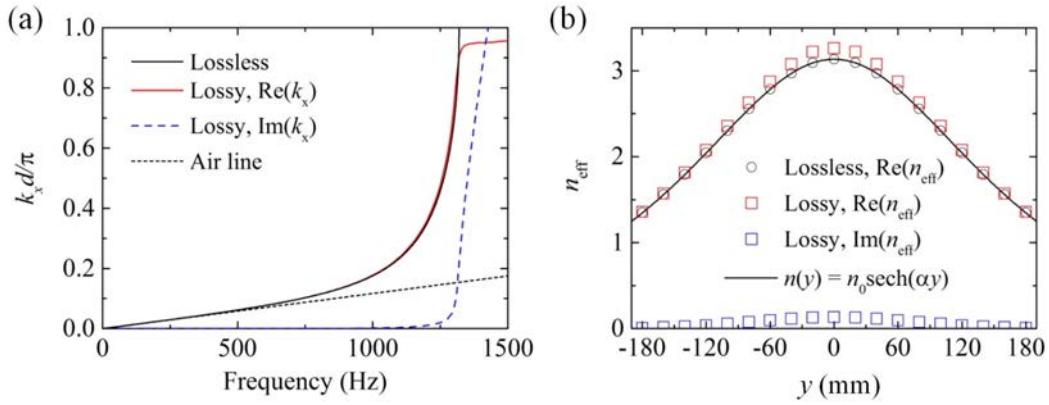

FIG. 3.4. Effect of the inherent thermal and viscous losses. (a) Dispersion relation of the structure-induced surface acoustic waves (SSAWs) in the presence of the inherent losses. The calculation is based on the lossy model presented in Section 2.4 with $a = 15$ mm, $d = 20$ mm and $h = 60$ mm. The wave vector of the SSAWs becomes a complex number for the lossy case (red solid line: real part; blue dashed line: imaginary part). The lossless dispersion curve (black solid line) and the air line (black short-dashed line) are also plotted for comparison. (b) Complex effective refractive index distribution at 1250 Hz in the presence of the inherent losses. Compared to the lossless model (black circles), a slight increase of $\mathrm{Re}(n_{\mathrm{eff}})$ (red squares) can be observed, accompanied by the emergence of $\mathrm{Im}(n_{\mathrm{eff}})$ (blue squares) that is much smaller than $\mathrm{Re}(n_{\mathrm{eff}})$.

Actually, the effect of the inherent losses can be utilized as an additional correction

to the ideal lossless model after a preliminary GRIN design based on Eq. (3.2). To confirm this point, the effective refractive index distribution of the lossy metasurface model is calculated and compared with the lossless one. As can be seen in Fig. 3.4(b), the thermal and viscous losses only induce slightly increased overall refractive indices and moderate attenuation of the SSAWs. In this case, the focal length would move closer to the source, and sound field would be weakened to some extent.

3.3 Subwavelength focusing

3.3.1 Experimental and simulation setup

The GRIN metasurface sample exhibited in Fig. 3.3(a) is fabricated using three-dimensional printing technique (stereolithography), with material (photosensitive resin) being much rigid compared to air. The last 5 columns of holes ($400\ \text{mm} \le x \le 500\ \text{mm}$) are filled with sound absorption materials to mimic a reflectionless boundary for the SSAWs, otherwise obvious interference pattern would appear as the structure is not infinitely extended. As shown in Fig. 3.5, the lock-in amplifier (Zurich Instrument HF2LI) controlled by the computer is used for signal generation and acquisition. It sends sinusoidal signals to the loudspeaker box via an audio power amplifier (Brüel & Kjær, Type 2716C) to generate acoustic waves. The loudspeaker box with a 10-mm-width, 380-mm-long slit acts as a line-like source, which consists of 9 1.5-inch full-range loudspeaker units (Peerless by Tymphany, PMT-40N25AL01-04). The sound field above the metasurface sample is measured by a 1/4-inch free-field microphone with built-in preamplifier (Brüel & Kjær, Type 4935), mounted on a two-dimensional moving stage. The recorded signals are sent back to the lock-in amplifier via a conditioning amplifier (Brüel & Kjær, NEXUS Type 2693A).

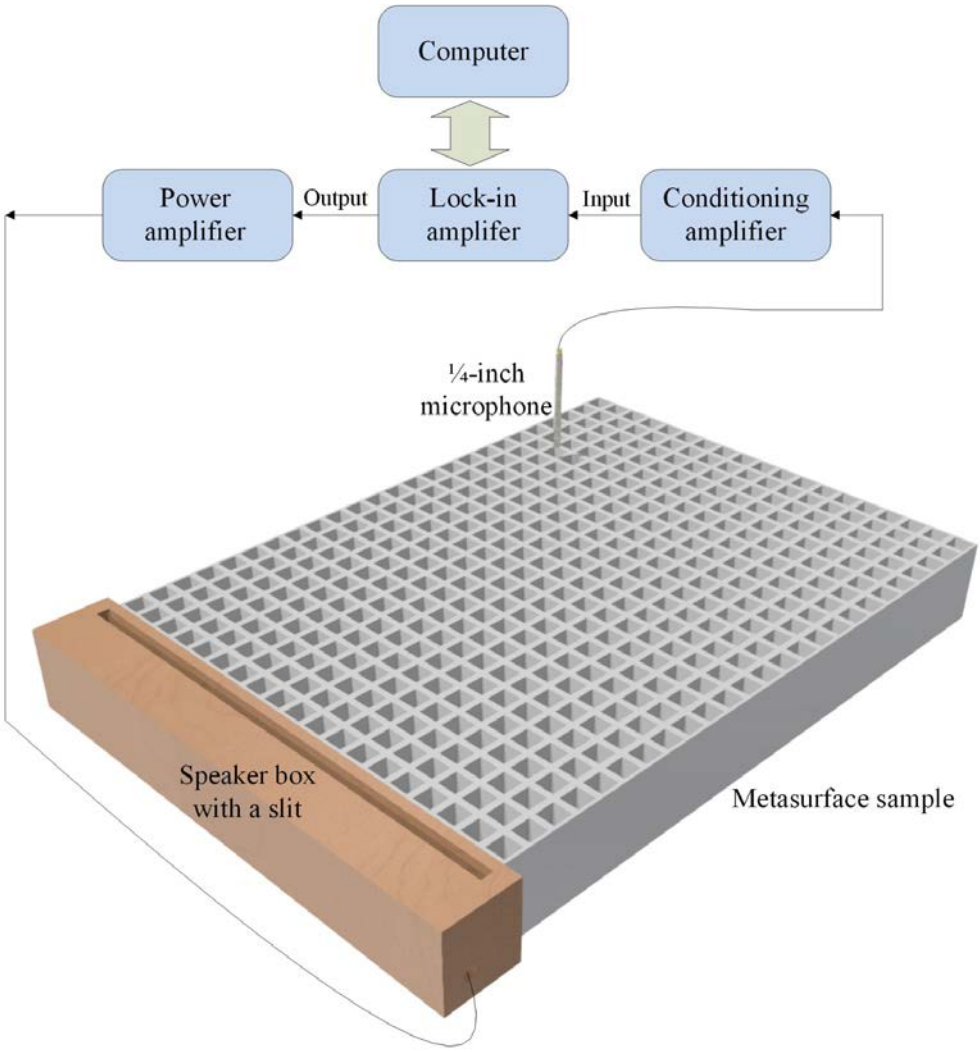

FIG. 3.5. Experimental setup for the measurement of subwavelength focusing. The loudspeaker box with a 10-mm-width, 380-mm-long slit is equivalent to a line-like source that can effectively excite the surface mode.

The simulated sound fields above the GRIN metasurface in the following section are obtained from three-dimensional full-wave FEM simulation in frequency domain. The line-like source is accomplished by applying plane wave radiation condition at a 10 mm × 380 mm area near the metasurface. The inherent losses due to thermal and viscous boundary layers inside the holes are introduced by replacing the purely real physical properties of air with frequency-dependent complex quantities [114-116]. The background medium is air (20 ˚C, standard atmospheric pressure), whose physical properties are: density $\rho_0 = 1.21\ \mathrm{kg/m^3}$, speed of sound $c_0 = 343\ \mathrm{m/s}$, thermal

conductivity $\kappa = 2.58\times10^{-2}$ W/m·K, viscosity $\mu = 1.81\times10^{-5}$ kg/m·s, the specific heat at constant pressure $C_p = 1.005\times10^{3}$ J/kg·K, and the ratio of the specific heats $\gamma = 1.4$. The mesh size is at most one-tenth of the smallest wavelength. Perfectly matched layers are implemented around the metasurface to mimic a semi-infinite space.

3.3.2 Experimental and simulation results

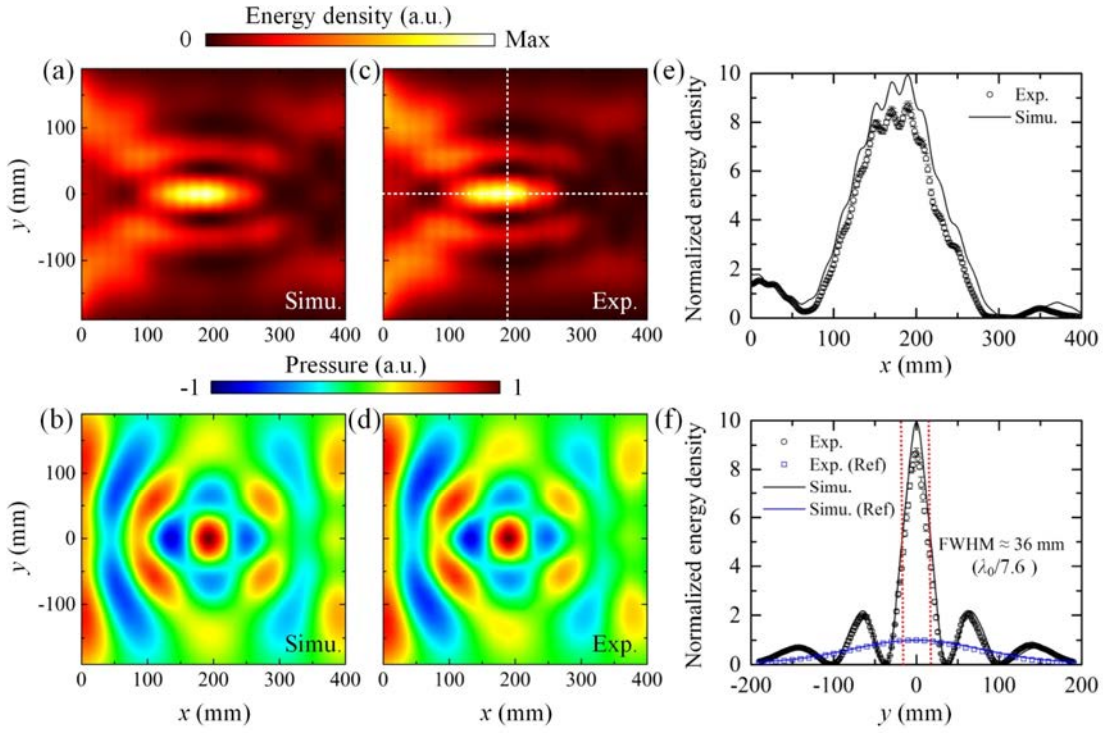

FIG. 3.6. Subwavelength focusing of airborne sound. (a) and (b) Simulated acoustic energy density and pressure fields. (c) and (d) Measured acoustic energy density and pressure fields. The measurements are conducted 10 mm above the metasurface, and the operating frequency is 1250 Hz. (e) and (f) Normalized energy density distributions along $y = 0$ and $x = 190$ mm. The white dashed lines in (c) mark where these curves are extracted. The results are normalized based on the energy density distribution along $x = 190$ mm [blue line and symbol in (f)] of a control experiment as shown in Fig. 3.7. The error bars are generated from 5 repeated measurements.

Figures 3.6(a)-3.6(d) are the simulated/measured acoustic energy density and pressure fields 10 mm above the GRIN metasurface at the designed operating frequency 1250 Hz, in which the overall experimental and simulation results agree very well with

each other. The incident plane SSAWs travelling from left to right gradually bend towards the central axis and converge to a small spot around $x = 190$ mm. At the position about $x = 360 \sim 380$ mm, the wavefront becomes nearly planar again and the sound field beyond that point would continue to be self-focused if the sample is long enough in the x direction. The whole propagation process is rather remarkable in the pressure field patterns given by Figs. 3.6(b) and 3.6(d), following the expected sinusoidal trajectory of a GRIN medium with transverse hyperbolic secant index profile [132]. This is in stark contrast to the control experiment as shown in Fig. 3.7, in which the simulated and measured sound fields above a rigid plain surface are presented.

The detailed acoustic energy density distributions along $x = 190$ mm and $y = 0$ [white dashed lines in Fig. 3.6(c)] are presented in Figs. 3.6(e) and 3.6(f). The focal spot indeed locates around $(190, 0)$ mm [highest peaks in Fig. 3.6(e)], which is consistent with our design. The measured and simulated FWHM are both about 36 mm [red dotted lines in Fig. 3.6(f)], roughly $\lambda_0 / 7.6$, where $\lambda_0 = 274.4$ mm is the wavelength in air at 1250 Hz. The measured energy density at the focal position is about 8.65 times (about 9.94 times in simulation) greater than that obtained from the control experiment as shown Fig. 3.7, revealing an intensively focused and compressed acoustic field. It is worth emphasizing that, unlike Refs. [30] and [98], the subwavelength focusing effect achieved here is not based on time reversal or array shape but induced by the GRIN profile despite that the slow surface mode plays equally crucial roles. This also breaks the restriction of the self-focusing effect inside a GRIN medium [132] or a high refractive index immersion lens [135] as the near-field high spatial frequency information brought by the airborne SSAWs is measurable in the open upper half-space. In this sense, such manipulation of airborne sound can be treated as being on subwavelength scale.

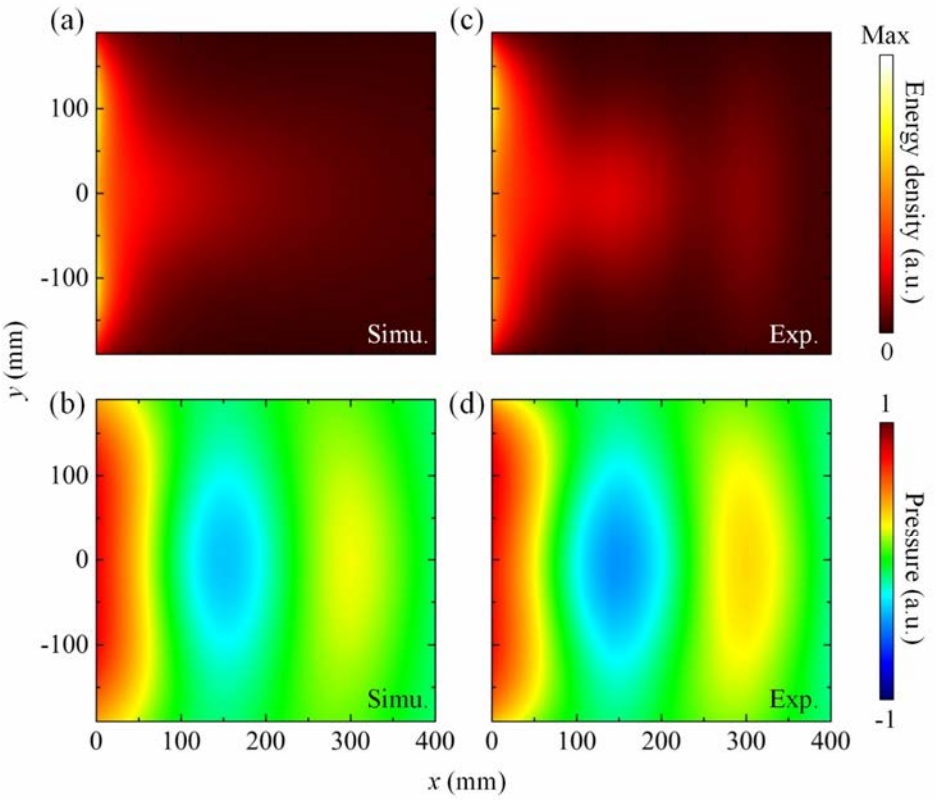

FIG. 3.7. Control experiment: sound fields above a rigid plain surface for the same line-like source at 1250 Hz. (a) and (b) Simulated acoustic energy density and pressure fields. (c) and (d) Measured acoustic energy density and pressure fields. The line-like source generates near plane waves that decay away from the source, with wavelength much larger than those in Figs. 3.6(a)-3.6(d). Weak interference appears in (c) since the plain surface is not infinitely large and there exist trivial reflections from the edge.

In addition, it can be inferred from Eq. (3.2) that the effective refractive index profile offered by the metasurface is frequency-dependent and approximately fits to the function $n(y) = n_0 \,\mathrm{sech}(\alpha y)$ with specific n_0 and α values for operating frequencies other than 1250 Hz. To illustrate this point, the acoustic energy density fields at different frequencies are provided in Fig. 3.8. One may unequivocally observe that the focal spot moves towards the source and becomes smaller as the operating frequency rises, resulting from the increased α and n_0 in $n(y) = n_0 \,\mathrm{sech}(\alpha y)$.

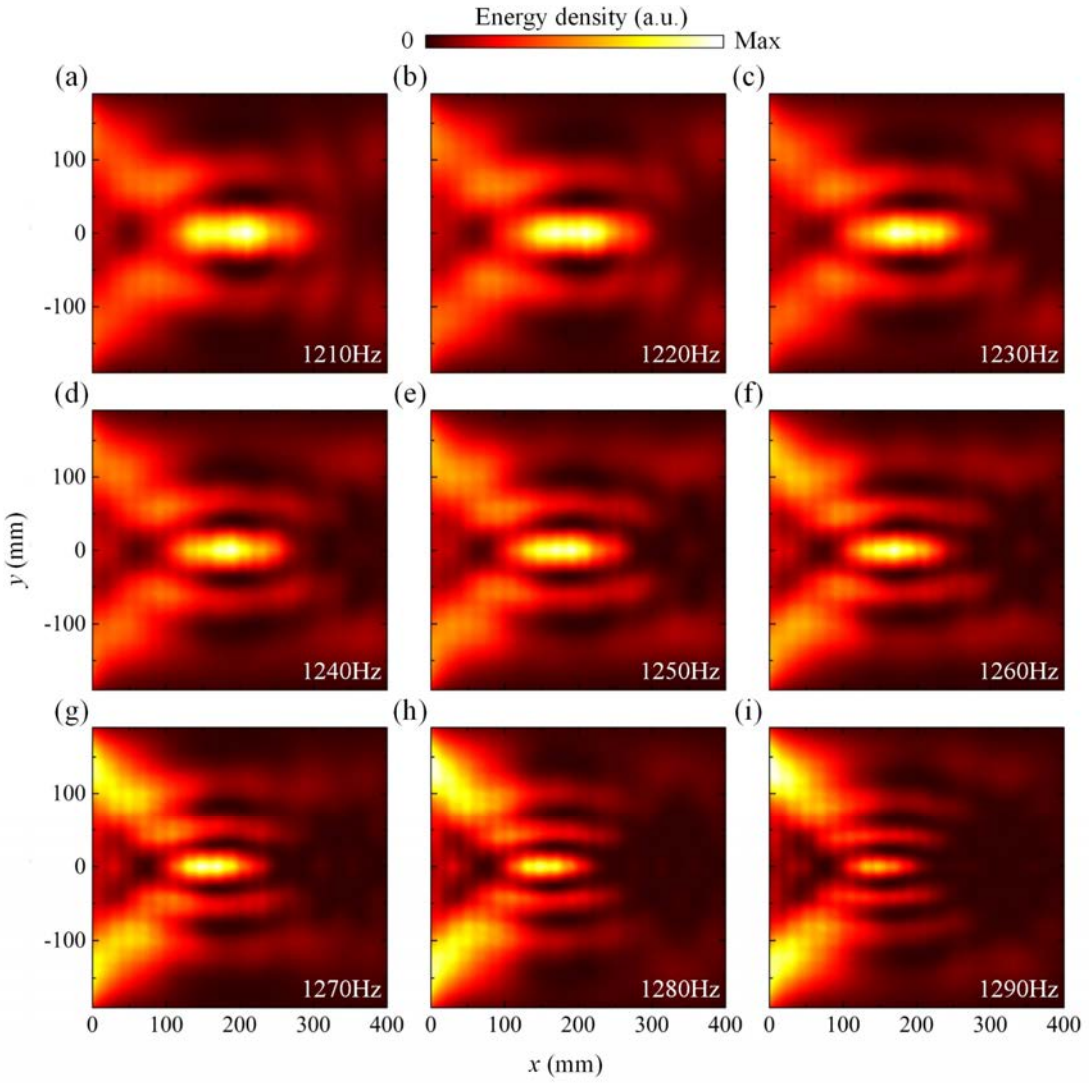

FIG. 3.8. Measured acoustic energy density fields at different frequencies: (a) 1210Hz; (b) 1220Hz; (c) 1230Hz; (d) 1240Hz; (e) 1250Hz; (f) 1260Hz; (g) 1270Hz; (h) 1280Hz; (i) 1290Hz. The field in each sub-figure is normalized to its own maximum value.

One may notice that the focal spot is "surprisingly" smaller than half the minimum wavelength of the SSAWs $\lambda_s = 2\pi / q \approx 87.7$ mm . This seemingly unreasonable phenomenon is due to two facts. First, the overall effective indices are underestimated in the lossless theoretical model of Eq. (3.2), namely, their actual values (in the presence of the inherent visco-thermal losses) should be slightly higher than our initial design [88,89], as evidenced in Fig. 3.4. Second, the energy density field within the opening area of a unit cell, namely, the inlet of the resonator, is stronger than that of its remaining

area, which is especially obvious for lower measuring height. Consequently, the sharpened focal spot leads to the small FWHM in Fig. 3.6(f). To explain the second point, we further examine the measured energy density fields at different heights above the metausrface [see Fig. 3.9]. It can be inferred from these results [Fig. 3.9(b)] that, the lower the measuring height, the more the FWHM approaches the side length of the holes. As has been pointed out by Refs. [30,98,131], the FWHM here is associated with yet not equivalent to the minimum spatial resolution, and the latter is determined by the highest effective refractive index of the SSAWs.

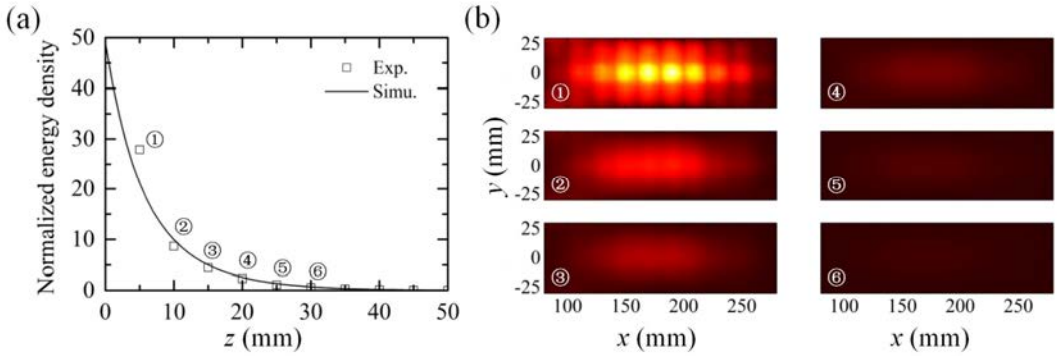

FIG. 3.9. Measured acoustic energy density fields at different heights above the gradient-index metasurface. (a) Normalized acoustic energy density values of the focal spot at different heights. The result is normalized based on the control experiment. Clearly, the energy density value decays exponentially away from the metasurface. (b) Measured energy density fields around the focal spot. ①-⑥ correspond to different heights marked in (a), which are normalized to the maximum value among all the results.

3.4 Subwavelength imaging

3.4.1 Sound fields subject to point-like sources

The essential reason of the so-called diffraction limit stems from the evanescent wave field which carries rich sub-wavelength information but decays exponentially outside the source region. As we have demonstrated above, the metasurface is capable of coupling the non-propagative evanescent fields into the propagating SSAWs with

large wave vectors, during which the information of high spatial frequency can be well preserved. It suggests that sub-diffraction-limited imaging should also be available with the same configuration. To find the image plane of the GRIN metasurface, now let us experimentally examine the sound fields subject to: (1) a single point-like source; (2) a pair of in-phase point-like sources; (3) a pair of out-of-phase point-like sources. The source is 10 mm × 10 mm in size, which can be regarded as a point compared to the wavelength in air. The experimental setup is depicted in Fig. 3.10.

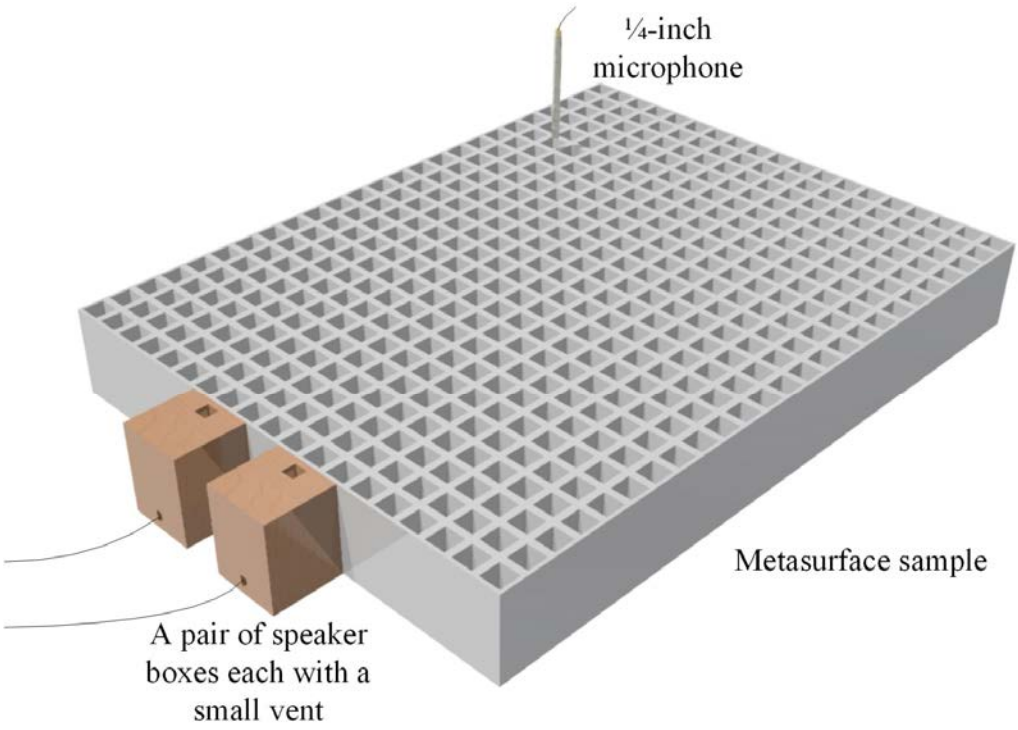

FIG. 3.10. Experimental setup for the measurement of sound fields subject to point-like source(s). Each loudspeaker box has a 10 mm × 10 mm square aperture, whcih is much smaller than the wavelength and can be regarded as a point-like source.

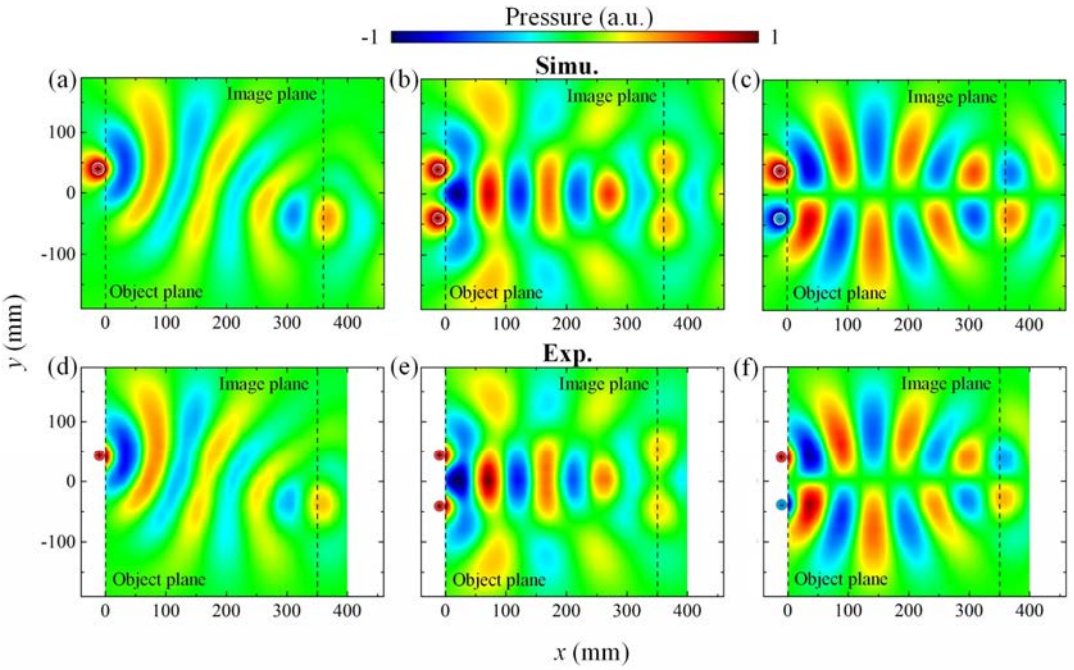

FIG. 3.11. Simulated and measured acoustic pressure fields at 1250 Hz subject to: (a) and (d) a single point-like source; (b) and (e) a pair of in-phase point-like sources; (c) and (f) a pair of out-of-phase point-like sources. The solid circles are the point-like sources, with colors denoting their phases. The object and image planes are marked by the black dashed lines. The simulation results are consistent with the those of the experiment, except that the location of the image plane (simulation: $x \approx 360$ mm; experiment: $x \approx 350$ mm) is slightly farther away from the source.

As shown in Figs. 3.11(a) and 3.11(d), in both simulation and experiment, the wavefront of the SSAWs generated by a single point-like source is modulated by the GRIN metasurface and refocused in the opposite side of the y-axis at about $x = 340 \sim 360$ mm, forming an inverted image with sub-diffraction-limited resolution. In Figs. 3.11(b)-3.11(c) and 3.11(e)-3.11(f), we further present the simulated and measured acoustic pressure fields induced by a pair of in-phase or out-of-phase point-like sources to demonstrate this fact. The center-to-center distance between the two sources is 80 mm, approximately $\lambda_0 / 3.4$ at 1250 Hz. It can be observed that the two point-like sources are distinguishable at about $x = 340 \sim 360$ mm after propagating along the GRIN metasurface. The overall measured pressure patterns [Fig. 3.11(d)-

3.11(f)] are consistent with those of the simulation [Fig. 3.11(a)-3.11(c)], but with minor differences in the location of the image plane along the x direction. Based on these results, we choose $x = 350$ mm [dashed lines in Figs. 5(d)-5(f)] as the image plane of the system. It slightly shifts towards the object plane ($x = 0$) in comparison with the simulation results [dashed lines in Fig. 3.11(a)-3.11(c)], which may be caused by the near-surface boundary layer losses (only losses inside the holes are considered in simulations), the environmental factors, the fabrication errors, etc.

3.4.2 Two-dimensional imaging

We note that the enhanced sound field of the SSAWs is confined to the GRIN metasurface and attenuates exponentially with the increase of z as shown in Fig. 3.9. It implies that the subwavelength imaging may potentially be extended to two-dimensional case since only the evanescent components near the metasurface can be effectively coupled to the propagative SSAWs. To this end, we perform a scanning of the object plane along the z direction and synthesize the measured energy density distributions in the image plane for different scanning heights z_h, as schematically illustrated in Fig. 3.12(a). Here a relatively complex object shaped like the letter “C” with subwavelength features [Fig. 3.12(b)] is used as a representative example. In experiment, the C-shaped object plane is implemented by inserting a carved thin plate that can move up and down in the z direction, between the line-like source and the metasurface sample [see Fig. 3.12(a)]. The carved plate is several times larger than the wavelength to suppress diffraction at the plate edges, and it is 10-mm away from both the speaker box and the metasurface sample so that the sound radiation is relatively stable for different scanning height z_h. The scanning height is controlled by adjusting the vertical position of the C-shaped opening. The energy density distribution 10-mm above the metasurface sample along $x = 350$ mm is then measured for each scanning

height.

As can be seen from Figs. 3.12(c)-3.12(e), most subwavelength features of the C-shaped object, e.g. edges and gaps, no matter along the y or z direction, are successfully rebuilt in the synthesized image plane and well validated by the experiment. Hence it is evidenced that the subwavelength imaging can be extended to two-dimensional case, without necessarily stacking the metasurfaces in the third direction to form a bulky structure.

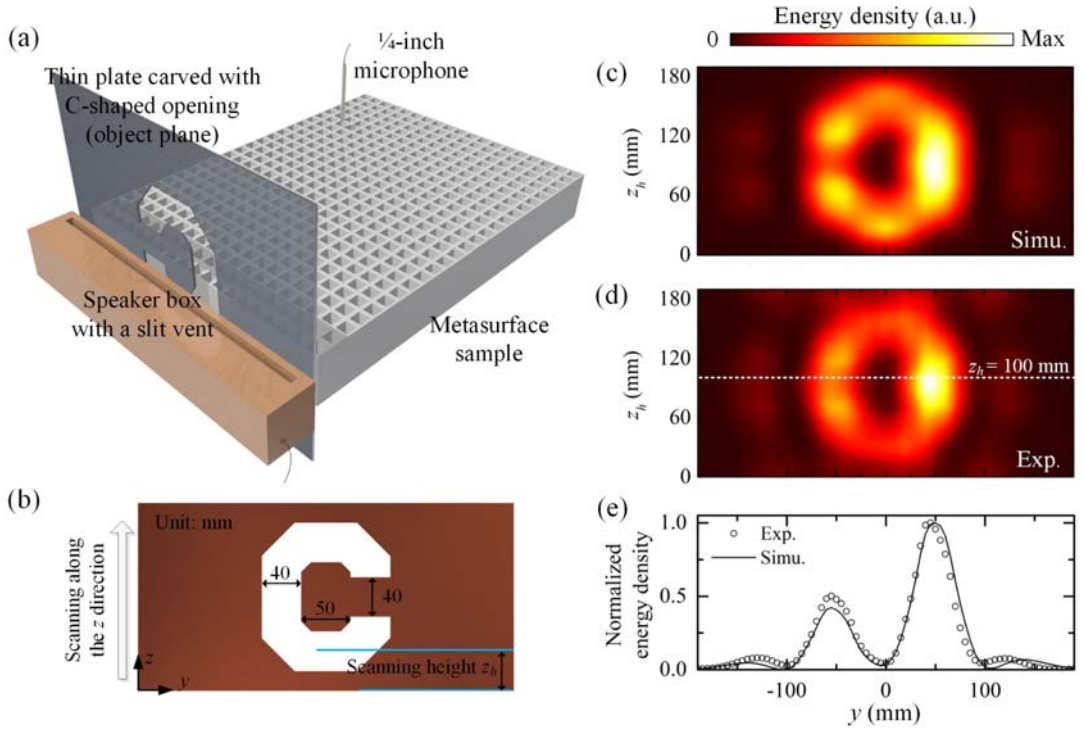

FIG. 3.12. Two-dimensional subdiffraction imaging. (a) Schematic illustration of the experimental setup. (b) C-shaped object plane. The scanning is conducted along the z direction. (c) and (d) Synthesized image planes in simulation ($x = 360$ mm) and experiment ($x = 350$ mm). The image planes are synthesized by combining all the energy density distributions obtained at different scanning heights z_h. (e) Normalized energy density distribution for $z_h = 100$ mm. The location of $z_h = 100$ mm is marked by dashed white line in (d). The circles and solid line denote experimental and simulation results, respectively.

3.5 Summary

This chapter has experimentally demonstrated the subwavelength focusing and imaging effects, with a gradient-index (GRIN) metasurface for the structure-induced surface acoustic waves (SSAWs) with large wave vectors. The design of this type of GRIN metasurfaces is greatly simplified benefited from the explicit mapping relation between the effective refractive index and the hole depth, avoiding massive time-consuming calculations. In this sense, the proposed GRIN design method offers a straightforward way to the subwavelength manipulation of airborne sound, not limited to the effects of focusing and imaging demonstrated here. Other GRIN-enabled devices [134] such as acoustic Eaton lens, Luneburg lens, Maxwell-fish-eye lens and black hole, or functionalities such as airy beam and Talbot effect under conformal transformation [136], can also be realized following similar approaches. Meanwhile, it is not difficult to imagine that even deeper subwavelength scale would become accessible if space-coiling [14,137] or helical-structured [138] metamaterials are adopted during the unit cell design.

In addition, the system is open to the surrounding environment and the enhanced wave field is measurable in the upper half-space near the metasurface. It is therefore an ideal platform to directly observe and investigate in experiment the propagation and energy flow of sound “inside” the metamaterials or sonic crystals counterparts. For instance, the phenomenon of backscattering-immune wave guiding in an acoustic topological insulator can be experimentally visualized in the subwavelength regime through measuring the topological structure-induced surface acoustic polaritons [101], which remains difficult for bulk composites or structures. Moreover, the non-leaky slow surface mode can further be coupled into a radiative mode, or vice versa, based on wave-vector matching via acoustic antennas [86,100]. It may enable more flexible ways

of sound manipulation and open new possibilities to innovative applications for acoustic focusing, imaging, sensing and detection beyond the diffraction limit.

Chapter 4:

All passive acoustic parity-time-symmetric metamaterials crystal

4.1 Introduction

The meta-structured surfaces can manipulate not only the structure-induced surface acoustic waves (SSAWs) but also the acoustic waves within waveguides. By replacing the rigid inner boundaries of acoustic waveguides with meta-structured surfaces, the resultant metamaterials can be used to modulate the refractive index in complex plane, which offers an intriguing opportunity to the study of parity-time (PT) symmetry in passive acoustic system.

The concept of PT symmetry originated from quantum mechanics and is regarded as a complex generalization of conventional quantum theory. Consider a Hamiltonian $\hat{H} = \hat{p}^2 / 2m + V(\hat{x})$ that specifies the energy levels and time evolution of a quantum system, where $\hat{p}$ is momentum operators, $\hat{x}$ is position operator, m is mass and V is the potential, respectively. It is Hermitian if it is invariant under conjugate transpose. Hermiticity guarantees that the energy spectrum is real, and that time evolution is unitary (probability-preserving). The introduction of complex potential $V(\hat{x}) = V_R(\hat{x}) + iV_I(\hat{x})$ would result in non-Hermiticity. It had long been believed that non-Hermitian Hamiltonians do not possess real eigenvalues. However, in 1998, Bender and Boettcher [139] demonstrated that non-Hermitian Hamiltonians can still exhibit real spectra and conserved probability as long as they respect PT symmetry, namely, they commute with combined PT operator $PT\hat{H} = \hat{H}PT$. And the symmetry is unbroken provided that the Hamiltonian and PT operator share the same eigenvectors. The action of parity operator P is the spatial reflection that flips the sign of momentum and position, defined as $\hat{p} \to -\hat{p}, \hat{x} \to -\hat{x}$. The action of time reversal

operator T flips the sign of momentum and leads to complex conjugation, defined as $\hat{p} \to -\hat{p}, \hat{x} \to \hat{x}, i \to -i$. Thus, a necessary (but not sufficient) condition of PT symmetry is that the complex potential obeys $V(\hat{x}) = V^*(-\hat{x})$. This is to say that it is spatially even in its real part $V_R(\hat{x}) = V_R(-\hat{x})$ and odd in its imaginary part $V_I(\hat{x}) = -V_I(-\hat{x})$.

For many years, PT-symmetric quantum mechanics had only been treated as an interesting mathematical discovery with hardly any practical application, because the experimental realization of complex potential in quantum system is extremely difficult. This changed in 2007, soon after the concept being introduced to optics, based on the analogy between the time dependent Schrodinger equation and the paraxial wave equation [140]. The PT-symmetric potential in quantum mechanics corresponds to a complex spatial distribution of refractive index in optical system, namely, symmetric in its real part and antisymmetric in its imaginary part, which can be expressed as $n(x) = n^*(-x)$. Such index distribution suggests a practical implementation of PT symmetry by using balanced optical gain and loss, and optics provide a fertile ground where PT symmetry physics can be widely exploited [141-146].

The most intriguing feature of PT-symmetric systems is the spontaneous PT symmetry breaking. As the non-Hermiticity parameters exceed a certain threshold, the eigenvalues of the Hamiltonian abruptly change from real to complex, and the system experiences a phase transition, from the unbroken to broken PT symmetry phase. At the broken PT symmetry phase, the condition $PT\hat{H} = \hat{H}PT$ is still valid, but $\hat{H}$ and PT cease to share the same eigenvectors. This phase transition signifies a non-Hermitian singularity or the so-called exceptional point, where the eigenstates become degenerate. In classical wave systems, exceptional point is associated with many

counter-intuitive phenomena and functionalities, which alternatively sheds new lights on a series of physical problems that have been described with frameworks other than PT symmetry. In the past decade, great effort has been dedicated to the realization of PT-synthetic medium [141-146] that can meet the requirement of complex PT-symmetric potentials through balanced gain/loss modulation. Unconventional phenomena, such as Bloch oscillations [147,148], unidirectional reflectionless resonance [149-153], coherent perfect laser/absorber [154-156], single-mode or vortex lasing [157-159], and low-power all-optical switch [160], have been demonstrated. However, the experimental investigations of PT-synthetic medium for optical systems are hitherto based on one-dimensional waveguides, in which the wave propagation direction is parallel or perpendicular to the PT-symmetric potential. The study of PT symmetry in higher dimensional space has only been theoretically discussed [161-166].

PT symmetry has also been introduced to acoustic wave system [45-48,50,167,168]. Although still in an early stage, it has already exhibited significant value and potential in many aspects including one-way cloak [45], invisible acoustic sensing [46], and phonon lasing [167]. Those designs followed the similar approach of one-dimensional gain/loss dimer configuration. To overcome the absence of acoustic gain medium in nature, active sound generating unit (e.g. electro-acoustic components) [43,46,48] or additional fluid field [168] has been applied to experimentally mimic the sound amplification behavior. Yet, the complicated circuit set-up and external energy supply unavoidably reduce the robustness and usability of these systems. Nevertheless, airborne sound is an ideal candidate that shows great flexibility in expanding PT-symmetry in higher-dimensional space due to its longitudinal wave nature (without the necessity to consider polarization) as well as the zero cut-off within waveguides.

To demonstrate the capability of passive acoustic system to carry the PT symmetry

study and manipulate the unpaired wave vectors in two-dimensional space, this chapter shows the realization of a one-way sound focusing effect, with an all passive acoustic PT-symmetric metamaterials crystal. For our design, the groove-structured and holey-structured acoustic metamaterials are interleaved to modulate the refractive index distribution in the complex plane, forming the so-called acoustic metamaterials crystal [121]. It offers intrinsic passive PT-symmetric potential that is equivalent to unidirectional wave vectors applying to the incoming acoustic waves. We systematically show how such passive PT symmetry is evolved from the exact PT symmetry, theoretically examined by the coupled-mode theory and the transfer matrix calculation. Making full use of the unique feature of the passive PT-symmetric system in two-dimensional space, one-way sound focusing effect along with reflectionless transparency in the opposite direction is achieved in both simulation and experiment. The proposed work presents a feasible way to implement PT-related novel devices, breaking the restrictions of gain medium. It may enable many unconventional functionalities and applications that are not available with Hermitian systems, e.g., one-way transmission and vortex radiation. More importantly, our passive acoustic PT-symmetric metamaterials crystal provides an entire new platform to investigate general quantum-analogs phenomena and to tailor the unpaired wave vectors in two-dimensional space. This chapter has been published in Ref. [169]

4.2 Passive acoustic parity-time symmetry

4.2.1 Evolution from the exact to the passive parity-time symmetry

The evolution from the exact to the passive PT-symmetric potential in one-dimensional space is illustrated in Fig. 4.1(a). The exact PT-symmetric potential, namely, a complex exponential modulation of the acoustic refractive index, can be written in a generalized form as

$$\Delta n(x) = n(x) - n_0 = n' \cos(qx) + i\delta n' \sin(qx) \tag{4.1}$$

with $n' \ll n_0$ and $q = 2k_0$, where n_0 is the background refractive index, n' is the modulation amplitude, k_0 is the wave number, and δ denotes the amplitude ratio between the imaginary and real parts. For a balanced modulation ($\delta = 1$), note that $\Delta n(x) = n' \exp(iqx)$, equivalent to an unpaired wave vector applied to incoming waves. The sinusoidal modulation is then simplified to a square-wave modulation [I→II, Fig. 4.1(a)] to reduce the structure design requirement since both modulations share similar scattering properties at the Bragg wavelength [45], which is expressed as

$$\Delta n^{(\mathrm{e})}(x)/n' = \begin{cases} 1+\delta i, & \dfrac{2m\pi}{q} \le x \le \dfrac{2m\pi}{q} + \dfrac{\pi}{2q} \\ -1+\delta i, & \dfrac{2m\pi}{q} + \dfrac{\pi}{2q} \le x \le \dfrac{2m\pi}{q} + \dfrac{\pi}{q} \\ -1-\delta i, & \dfrac{2m\pi}{q} + \dfrac{\pi}{q} \le x \le \dfrac{2m\pi}{q} + \dfrac{3\pi}{2q} \\ 1-\delta i, & \dfrac{2m\pi}{q} + \dfrac{3\pi}{2q} \le x \le \dfrac{2m\pi}{q} + \dfrac{2\pi}{q} \end{cases}, \tag{4.2}$$

where $m \in \mathbb{Z}$. Alternatively, the sinusoidal modulation can be regarded as the first-order Fourier expansion of a square-wave modulation. Due to the lack of gain medium for sound, Eq. (4.2) is truncated by only considering $x \in [4m\pi/q + \pi/q, 4m\pi/q + 2\pi/q]$, and rewritten as

$$\Delta n^{(\mathrm{p})}(x)/n' = \begin{cases} -1-\delta i, & \dfrac{4m\pi}{q} + \dfrac{\pi}{q} \le x \le \dfrac{4m\pi}{q} + \dfrac{3\pi}{2q} \\ 1-\delta i, & \dfrac{4m\pi}{q} + \dfrac{3\pi}{2q} \le x \le \dfrac{4m\pi}{q} + \dfrac{2\pi}{q} \end{cases}, \tag{4.3}$$

After truncation [II→III, Fig. 4.1(a)], only one negative half cycle out of two periods of the imaginary part modulation is retained, making the modulation period T_m doubled (from $T_m^{(\mathrm{e})} = 2\pi/q$ to $T_m^{(\mathrm{p})} = 4\pi/q$), where the second-order Bragg scattering of the system is considered [152] (hereinafter, we use the superscript (e) or (p) to

denote the exact or passive case). This treatment allows us to conduct an in-phase shift of the real part so that the spatial overlap between the two modulations can be separated, as we will present later.

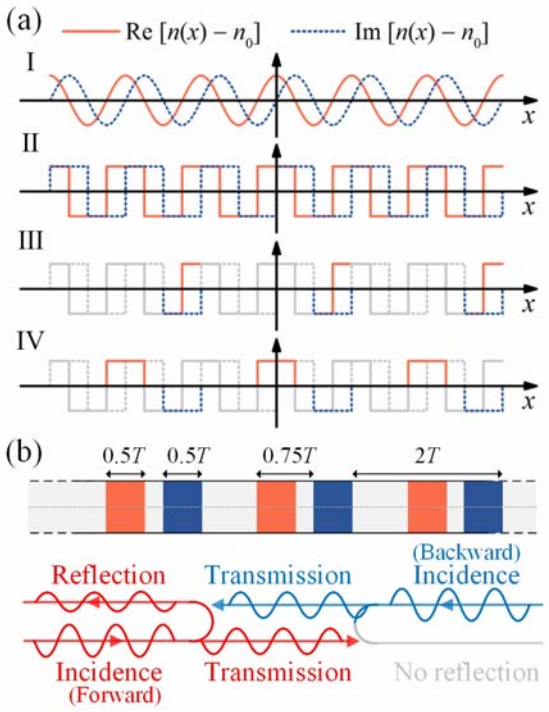

FIG. 4.1. Exact and passive acoustic PT-symmetric potentials [169]. (a) Evolution of the acoustic PT-symmetric potential through refractive index modulations: I. Exact PT-symmetric potential (complex exponential modulation) → II. Exact PT-symmetric potential (complex square-wave modulation) → III. Passive PT-symmetric potential (truncated complex square-wave modulation) → IV. Passive PT-symmetric potential ($3\pi/2$ in-phase shift of the real part modulation). The red/blue curves denote the real/imaginary part modulations. (b) Arrangement of the real part and imaginary part refractive index modulators. The modulation period is $T_m = 2T$. The passive PT-symmetric system experiences an exceptional point where a π phase-shift occurs with backward reflection vanished.

The scattering matrix of such exact or passive PT-symmetric potential (square-wave modulation) can be derived based on the coupled-mode theory. Consider the pressure field with time dependence $e^{i\omega t}$ ($\omega = 2\pi f$ is the angular frequency) inside the modulated region that contains forward and backward plane waves:

$$P = P_f(x)e^{-ikx} + P_b(x)e^{ikx}, \tag{4.4}$$

where $P_f(x)$ and $P_b(x)$ are respectively the amplitudes of forward and backward propagating components. In weak coupling regime ($n' \ll n_0$), the coupled-mode equations take the form

$$\begin{cases} \dfrac{\mathrm{d}P_f(x)}{\mathrm{d}x} = -iC_0\alpha P_f(x) - iC_{-q}\kappa P_b(x) \\ \dfrac{\mathrm{d}P_b(x)}{\mathrm{d}x} = iC_q\kappa P_f(x) + iC_0\alpha P_b(x) \end{cases}. \tag{4.5}$$

Here α is the attenuation coefficient inside the modulated region, and κ is the coupling coefficient between forward and backward propagating modes. The coefficients C_0 , C_q and C_{-q} can be determined by applying the Fourier transformation to Eqs. (4.2) and (4.3) as $\Delta n(x)/n' = C_q \exp(iqx) + C_{-q}\exp(-iqx) + C_0$ and averaging over the entire modulation period T_m ($T_m^{(\mathrm{e})} = 2\pi/q$ and $T_m^{(\mathrm{p})} = 4\pi/q$)

$$\begin{aligned} C_0 &= \frac{1}{T_m}\int_0^{T_m} \frac{\Delta n(x)}{n'}\mathrm{d}x, \\ C_q &= \frac{1}{T_m}\int_0^{T_m} \frac{\Delta n(x)}{n'}e^{-iqz}\mathrm{d}x, \\ C_{-q} &= \frac{1}{T_m}\int_0^{T_m} \frac{\Delta n(x)}{n'}e^{iqz}\mathrm{d}x, \end{aligned} \tag{4.6}$$

which yields

$$C_0^{(\mathrm{e})} = 0,\ C_q^{(\mathrm{e})} = 2(\frac{1+\delta}{\pi}),\ C_{-q}^{(\mathrm{e})} = 2(\frac{1-\delta}{\pi}).$$

$$C_0^{(\mathrm{p})} = -i\frac{\delta}{4},\ C_q^{(\mathrm{p})} = \frac{1}{2}(\frac{1+\delta}{\pi}),\ C_{-q}^{(\mathrm{p})} = \frac{1}{2}(\frac{1-\delta}{\pi}).$$

Comparing these two groups of coefficients we may found that : the attenuation terms C_0 is not zero any more for the passive PT-symmetric case due to the absence of gain medium; there exists a factor of 4 in C_q and C_{-q} , namely, $C_q^{(\mathrm{e})} = 4C_q^{(\mathrm{p})}$ and

$C_{-q}^{(e)} = 4C_{-q}^{(p)}$. For the modulations as given in Eqs. (4.2) and (4.3) ranging from $x = 0$ to $x = L$ ($L \gg 4\pi/q$), the elements of the transfer matrix

$$\begin{pmatrix} P_f(L) \\ P_b(L) \end{pmatrix} = \begin{pmatrix} M_{11} & M_{12} \\ M_{21} & M_{22} \end{pmatrix} \begin{pmatrix} P_f(0) \\ P_b(0) \end{pmatrix} \tag{4.7}$$

are deduced as (n' is omitted for simplicity)

$$M_{11}^{(e)} = \cosh(\gamma^{(e)}L), \quad M_{12}^{(e)} = -i\frac{2(1-\delta)}{\pi}\frac{\kappa}{\gamma^{(e)}}\sinh(\gamma^{(e)}L),$$

$$M_{21}^{(e)} = i\frac{2(1+\delta)}{\pi}\frac{\kappa}{\gamma^{(e)}}\sinh(\gamma^{(e)}L), \quad M_{22}^{(e)} = \cosh(\gamma^{(e)}L),$$

$$M_{11}^{(p)} = \cosh(\gamma^{(p)}L) + \frac{\delta}{4}\frac{\alpha}{\gamma^{(p)}}\sinh(\gamma^{(p)}L), \quad M_{12}^{(p)} = -i\frac{1-\delta}{2\pi}\frac{\kappa}{\gamma^{(p)}}\sinh(\gamma^{(p)}L),$$

$$M_{21}^{(p)} = i\frac{1+\delta}{2\pi}\frac{\kappa}{\gamma^{(p)}}\sinh(\gamma^{(p)}L), \quad M_{22}^{(p)} = \cosh(\gamma^{(p)}L) - \frac{\delta}{4}\frac{\alpha}{\gamma^{(p)}}\sinh(\gamma^{(p)}L),$$

where

$$\gamma^{(e)} = 2\kappa\sqrt{(1-\delta^2)}/\pi.$$

$$\gamma^{(p)} = \sqrt{(\delta\alpha/4)^2 + (1-\delta^2)\kappa^2/4\pi^2}.$$

The scattering matrix is subsequently derived as

$$S = \begin{pmatrix} t & r_b \\ r_f & t \end{pmatrix} = \begin{pmatrix} M_{22}^{-1} & M_{12}M_{22}^{-1} \\ -M_{21}M_{22}^{-1} & M_{22}^{-1} \end{pmatrix}. \tag{4.8}$$

where t, r_f and r_b represent the transmission, forward-reflection, and backward-reflection coefficients, respectively. The eigenvalues of S can thus be acquired by substituting the elements of the transfer matrix into Eq. (4.8) as

$$\lambda_{1,2} = t \pm \sqrt{r_f r_b}, \tag{4.9}$$

specifically, for the studied exact and passive PT-symmetric systems

$$\lambda_{1,2}^{(e)} = \frac{1 \pm i\frac{2}{\pi}\frac{\kappa}{\gamma^{(e)}}\sinh(\gamma^{(e)}L)\sqrt{1-\delta^2}}{\cosh(\gamma^{(e)}L)} = \frac{1 \pm i\sinh(\gamma^{(e)}L)}{\cosh(\gamma^{(e)}L)} \tag{4.10}$$

$$\lambda_{1,2}^{(\mathrm{p})}=\frac{1\pm i\frac{1}{2\pi}\frac{\kappa}{\gamma^{(\mathrm{p})}}\sinh(\gamma^{(\mathrm{p})}L)\sqrt{1-\delta^2}}{\cosh(\gamma^{(\mathrm{p})}L)-\frac{\delta}{4}\frac{\alpha}{\gamma^{(\mathrm{p})}}\sinh(\gamma^{(\mathrm{p})}L)}. \tag{4.11}$$

Still, we can find that a factor of 4 is involved in the coefficient before the hyperbolic sine function of the numerator between Eqs. (4.10) and (4.11). To clarify the physical meaning of the expression of $\lambda_{1,2}^{(\mathrm{p})}$, a loss factor $a=\sqrt{1+M_{12}^{(\mathrm{p})}M_{21}^{(\mathrm{p})}}\cdot(M_{22}^{(\mathrm{p})})^{-1}$ is introduced and one may further obtain

$$S^{(\mathrm{p})\prime}=S^{(\mathrm{p})}/a=\begin{pmatrix}\frac{1}{\sqrt{1+M_{12}^{(\mathrm{p})}M_{21}^{(\mathrm{p})}}} & \frac{M_{12}^{(\mathrm{p})}}{\sqrt{1+M_{12}^{(\mathrm{p})}M_{21}^{(\mathrm{p})}}}\\ \frac{-M_{21}^{(\mathrm{p})}}{\sqrt{1+M_{12}^{(\mathrm{p})}M_{21}^{(\mathrm{p})}}} & \frac{1}{\sqrt{1+M_{12}^{(\mathrm{p})}M_{21}^{(\mathrm{p})}}}\end{pmatrix}, \tag{4.12}$$

$$\lambda_{1,2}^{(\mathrm{p})\prime}=\lambda_{1,2}^{(\mathrm{p})}/a=\frac{1\pm i\frac{1}{2\pi}\frac{\kappa}{\gamma^{(\mathrm{p})}}\sinh(\gamma^{(\mathrm{p})}L)\sqrt{1-\delta^2}}{\sqrt{1+\frac{1}{4\pi^2}\frac{\kappa^2}{(\gamma^{(\mathrm{p})})^2}\sinh^2(\gamma^{(\mathrm{p})}L)(1-\delta^2)}}. \tag{4.13}$$

It is evident that the eigen-spectrum of the passive PT-symmetric system ($\lambda_{1,2}^{(\mathrm{p})}$) is that of an exact PT-symmetric system ($\lambda_{1,2}^{(\mathrm{p})\prime}$) multiplied by a additional factor $a<1$ that shifts the eigenvalues towards losses. When $0\le\delta<1$, $\lambda_{1,2}^{(\mathrm{p})\prime}$ are conjugated and unimodular. The system operates in the passive unbroken PT symmetry phase, corresponding to the unbroken PT symmetry phase in an exact PT-symmetric system with balanced gain and loss. If $\delta>1$, $\lambda_{1,2}^{(\mathrm{p})\prime}$ are nonunimodular with a pair of reciprocal moduli. The system operates in the passive broken PT symmetry phase, corresponding to the broken PT symmetry phase in an exact PT-symmetric system. When $\delta=1$, the eigenvalues become degenerate with $\lambda_{1,2}^{(\mathrm{p})\prime}=1$ and $\lambda_{1,2}^{(\mathrm{p})}=a=\exp(-\alpha L/4)$. In this case, similar to the phase transition behavior from the unbroken to broken PT symmetry

phase in a complete PT-symmetric system, the passive system experiences a spontaneous PT symmetry breaking, or the so-called exceptional point, where a π phase-shift occurs with backward reflection vanished.

In order to remove the overlap with the imaginary part modulation, the real part modulation is then shifted $3\pi/2$ in phase [III→IV, Fig. 4.1(a)]. It permits us to go a step further towards the simple and practical impelmentation of the passive PT-symmetric system as now the real and imaginary part modulators can be independently design. In the next section, the transfer-matrix calculations are performed to examine the effectiveness of our treatment in a rigorous and straightforward way. As we show in the following, the studied acoustic system [IV, Fig. 4.1(a)] is equivalent to the exact PT-symmetric system with balanced gain and loss, except that an additional loss factor a is introduced owing to the purely passive modulation. Alternatively, such passive PT-symmetric modulation can be regarded as a balanced gain-loss modulation applied to the background medium with global loss. It can still provide an unpaired wave vector to incoming waves [149,152] so that the backward reflection vanishes.

4.2.2 Transfer matrix modeling

The phenomenon of unidirectional reflectionlessness predicted by the coupled-mode theory may be explained from the view of a multiple-reflection/transmission process, in which each interface of a one-dimensional passive PT-symmetric system can be regarded as a secondary plane source. As shown in Fig. 4.2, incident plane waves (continuous waves) penetrating upon the passive PT-symmetric medium generate multiple transient reflections and transmissions that bounce back and forth within each layer. At steady-state, the stationary reflection/transmission of each interface is the sum of an infinite number of transient reflections/transmissions at that interface. In this sense, each interface (e.g. $x = x_{(m,j)}$) is equivalent to a secondary plane source that radiates

forward-traveling component $P_f^{(m+1,j)}$ and backward-traveling component $P_b^{(m,j)}$. Therefore, the out-going components at the two outside boundaries of the stratified medium suggest the overall reflections r_f and r_b of the one-dimensional passive PT-symmetric system. Note that the transient reflections are in-phase in the forward direction, whereas out-of-phase in the backward direction. In other words, they constructively interfered with each other to generate forward-reflection and cancel out with each other to eliminate the backward-reflection.

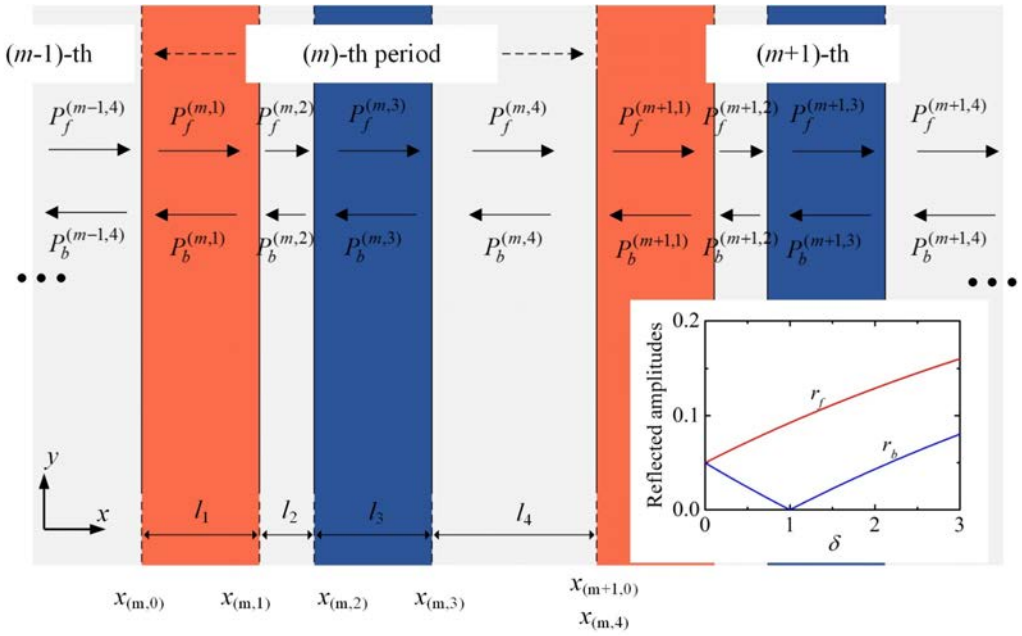

FIG. 4.2. Transfer-matrix calculation of the reflections from a one-dimensional passive PT-symmetric medium [169]. Each period contains four layers of homogenous media, and each interface located at $x = x_{(m,j)}$ can be treated as a secondary plane source. The inset is the amplitudes of the reflections for forward and backward incidences as a function of δ. In the calculation, the modulation amplitude is set as $n' = 0.001n_0$ and the total length is $L = 100T$, with operating frequency being the Bragg frequency.

These components can be easily determined using the transfer matrix method. Here each period of the studied passive PT-symmetric potential as shown in Fig. 4.2 contains four layers: one layer of real part modulation, one layer of imaginary part modulation, and two layers of background medium. Consider the pressure field and the associated

particle velocity field of the forward and backward propagating waves in the *j*-th layer, *m*-th period ($j = 1, 2, 3, 4$ and m is an integer)

$$P = P_f^{(m,j)} e^{-ik_j x} + P_b^{(m,j)} e^{ik_j x}, \tag{4.14}$$

$$V = -\frac{1}{i\omega\rho_j}\frac{\partial P}{\partial x} = \frac{P_f^{(m,j)}}{\rho_j c_j} e^{-ik_j x} - \frac{P_b^{(m,j)}}{\rho_j c_j} e^{ik_j x}, \tag{4.15}$$

where ρ_j, c_j, and k_j are the density, the speed of sound, and the wavenumber in the *j*-th layer of thickness l_j. The pressures and particle velocities on both ends of the layer are connected through a transfer matrix $\mathbf{T}_j$

$$\begin{bmatrix} P(x_{(m,j-1)}) \\ V(x_{(m,j-1)}) \end{bmatrix} = \mathbf{T}_j \begin{bmatrix} P(x_{(m,j)}) \\ V(x_{(m,j)}) \end{bmatrix}, \tag{4.16}$$

where

$$\mathbf{T}_j = \begin{bmatrix} \cos(k_j l_j) & i\rho_j c_j \sin(k_j l_j) \\ i\sin(k_j l_j)/\rho_j c_j & \cos(k_j l_j) \end{bmatrix}, \quad j = 1, 2, 3, 4 \tag{4.17}$$

For a passive PT-symmetric system consisting of N_m periods, the overall transfer matrix in the forward and backward directions can be written in the form

$$\mathbf{T}^{(f)} = [\mathbf{T}_1 \cdot \mathbf{T}_2 \cdot \mathbf{T}_3 \cdot \mathbf{T}_4]^{N_m}, \tag{4.18}$$

$$\mathbf{T}^{(b)} = [\mathbf{T}_4 \cdot \mathbf{T}_3 \cdot \mathbf{T}_2 \cdot \mathbf{T}_1]^{N_m}. \tag{4.19}$$

The reflection coefficient can be obtained from the elements in $\mathbf{T}^{(f)}$ or $\mathbf{T}^{(b)}$ as

$$r = \frac{T_{11} + (T_{12}/\rho_0 c_0) - \rho_0 c_0 T_{21} - T_{22}}{T_{11} + (T_{12}/\rho_0 c_0) + \rho_0 c_0 T_{21} + T_{22}}, \tag{4.20}$$

where ρ_0 and c_0 are the density and the speed of sound in the background medium.

We then use the transfer matrix method to examine the overall reflections from a passive PT-symmetric medium with $n' = 0.001 n_0$ and $L = 100T$ ($T_m^{(\mathrm{p})} = 2T_m^{(\mathrm{e})} = 2T$). As shown in the inset of Fig. 4.2, the backward reflection vanishes when the real and

imaginary part modulations become balanced, namely, when $\delta = 1$, which corresponds to the vicinity of exceptional point. With the transfer matrix model, we may conclude that, from the view of a multiple-reflection process, the unidirectional reflectionlessness phenomenon is a result of the constructive and destructive interferences of all the reflections and transmissions within the passive PT-symmetric medium. The absolute value of the eigenvalues $\lambda_{1,2} = t \pm \sqrt{r_f r_b}$ and the second components $\pm\sqrt{r_b / r_f}$ of the eigenvectors $(1 \quad \pm\sqrt{r_b / r_f})^T$ for both the exact and passive PT-symmetric systems [II and IV in Fig. 4.1(a)] are also calculated to more fundamentally examine the studied passive system. The black and red curves/circles presented in Fig. 4.3(a) overlap with each other (due to conjugation) in exact/passive unbroken PT symmetry phase ($0 \le \delta < 1$), degenerate at the exceptional point ($\delta = 1$), and are unequal in the exact/passive broken PT symmetry phase ($\delta > 1$). This is further confirmed by Fig. 4.3(b), in which $\pm\sqrt{r_b / r_f}$ are either purely real at $0 \le \delta < 1$ or purely imaginary at $\delta > 1$ [45]. The results unequivocally show similar underlying physics and behavior in PT phase evolution between the two systems.

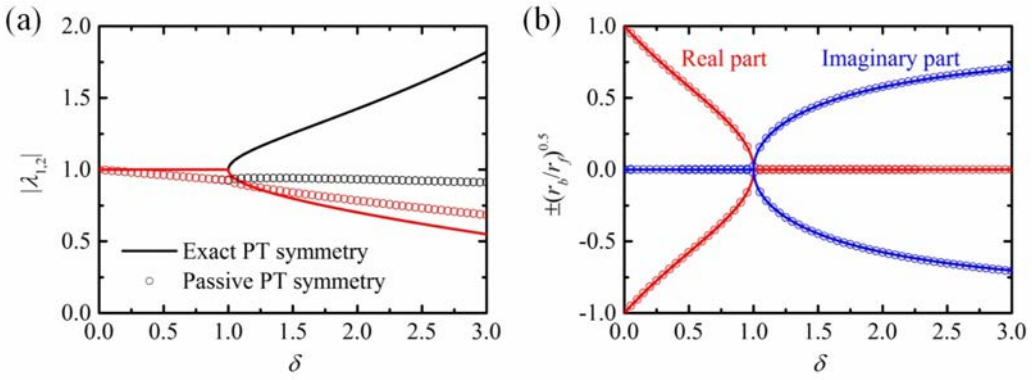

FIG. 4.3. Transfer-matrix calculation of the scattering matrix [169]. (a) Absolute value of the eigenvalues and (b) the second term of the eigenvectors of the scattering matrix, where lines and circles denote the exact and passive PT-symmetric potentials [II and IV in Fig. 4.1(a)].

4.2.3 Setting the amplitude and number of modulation periods

The coupled-mode theory requires that the modulation amplitude of the passive acoustic PT-symmetric potential to be as low as possible, compared with the refractive index of background medium. Hence the number of modulation periods should be sufficiently large to observe the unidirectional reflection effect. For example, for the theoretical calculations shown in Figs. 4.2, 4.3(a) and 4.3(b), $n' = 0.001 n_0$ and $L = 50 T_m$ ($T_m^{(\mathrm{p})} = 2T_m^{(\mathrm{e})} = 2T$). However, two elements have prevented us from applying those parameters into the final design. First, to provide a low-amplitude modulation, the features of designed structures must be small enough. Considering the audible frequency range (with wavelength about $10^{-2} \sim 10^{1}\,\mathrm{m}$), the required highly precise machining is hard to accomplish and high in cost. Secondly, a large amount of modulation periods will eventually lead to unpractically large size of the final sample.

It is then necessary to discuss how the number of modulation periods N_m affects the reflection and transmission characteristics. Here the modulation amplitude and period are set as $n' = 0.05 n_0$ and $T_m^{(\mathrm{p})} = 2T = 4\pi/q = 120$ mm, and conduct transfer-matrix-based calculations. Figure 4.4(a) shows the broadband reflection/transmission characteristics for different N_m: larger N_m results in higher amplitude of the forward-reflection r_f (red lines) around the Bragg frequency and narrower overall bandwidth, until N_m reaches about 40; the overall amplitude of the backward-reflection r_b is very low over the studied spectrum for any N_m; the amplitude of the transmission t declines and tends to be diminished as N_m increases. The reflectance and transmittance $|r_f|^2$, $|r_b|^2$ and $|t|^2$ as a function of N_m at 2820 Hz (near the peak that corresponds to the Bragg resonance) are further plotted in Fig. 4.4(b) to clearly

demonstrate this behavior. These calculations help us to determine a proper N_m to experimentally investigate the phenomenon of unidirectional reflectionlessness with a practical design. For instance, in our design (5% modulation amplitude), a reasonable number of modulation periods ($N_m = 3 \sim 10$) is sufficient to generate obvious reflection from only one side together with partial transparency, a unique and typical functionality of the passive PT-symmetric system.

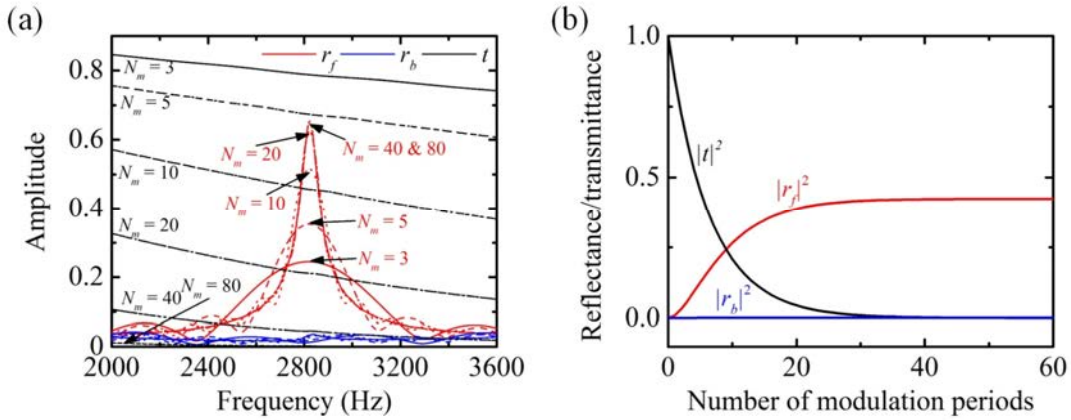

FIG. 4.4. Effects of the number of modulation periods on the reflection and transmission characteristics [169]. (a) Broadband reflection and transmission coefficients for different numbers of modulation periods N_m. (b) Reflectance and transmittance versus the number of modulation periods at 2820 Hz. For all the calculations, the modulation amplitude and period are set as $n' = 0.05n_0$ and $T_m^{(p)} = 2T = 4\pi/q = 120$ mm , respectively.

After careful evaluation, we set the modulation amplitude as $0.05n_0$ (still can be treated as weak modulation) and limit the number of the combined real/imaginary modulations to 5 pairs (total length corresponding to 10 periods of the exact PT-symmetric modulation) in the following metamaterials crystal design. Such treatment allows us to clearly observe the phenomenon of unidirectional reflection, while restricting the overall scale of the system within a reasonable range.

4.3 Acoustic metamaterials crystal respecting passive parity-time symmetry

4.3.1 Effective medium simulation

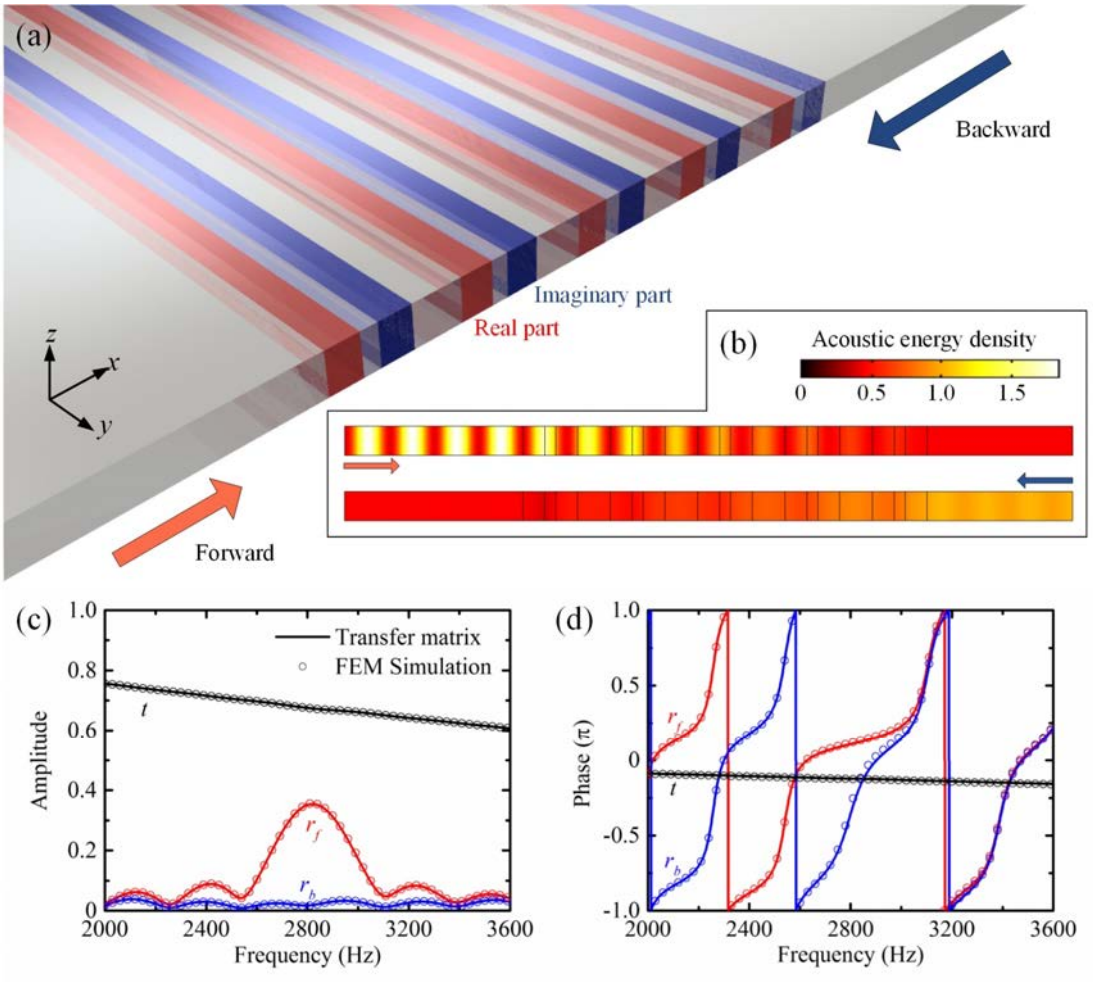

FIG. 4.5. Effective medium design and simulation of the one-dimensional passive acoustic PT-symmetric medium [169]. (a) Schematic of the effective medium model. The red and blue regions represent the real and imaginary part modulators, respectively. The length of the modulators is 30 mm and the center-to-center distance between the real and imaginary modulators is 45 mm. (b) Simulated energy density fields in *xz*-plane for forward and backward incidences. The amplitude is normalized per the background field. (c) and (d) are the spectral amplitude and phase responses, including reflection (red, forward; blue, backward) and transmission (black) coefficients in both directions. The reference point of the phase responses locates at the output surfaces of the PT-symmetric medium. The transfer-matrix calculation (solid line) and the numerical result (circle) are consistent with each other.

Before designing metamaterials for the real and imaginary part acoustic

modulations, the one-dimensional passive PT-symmetric metamaterials crystal model was analyzed with effective medium approach in simulation, as shown in Fig. 4.5(a). The effective speeds of sound in the real and imaginary part modulators are defined as $c_{\mathrm{Re}} = 326.67\ \mathrm{m/s}$ and $c_{\mathrm{Im}} = 342.14 - i17.107\ \mathrm{m/s}$, respectively. Their densities are the same as that of the background medium. The background medium is air with density $\rho_0 = 1.21\ \mathrm{kg/m^3}$, speed of sound $c_0 = 343\ \mathrm{m/s}$, and refractive index $n_0 = 1$. The designed modulation period is $T_m = 2T = 120\ \mathrm{mm}$ and the height of the waveguide is $2H = 40\ \mathrm{mm}$ .The full-wave numerical simulations were performed with finite-element method (FEM) using COMSOL Multiphysics. The mesh size is at most one-tenth of the smallest wavelength. Perfectly-matched layers were employed around the passive PT-symmetric medium to mitigate the reflection of sound waves.

Simulated energy density fields in Fig. 4.5(b) exhibit asymmetric reflection patterns when incident waves come from opposite directions. In the forward direction (left to right), remarkable interference indicates strong sound reflections from the passive PT-symmetric material. The energy density field induced by the backward incidence is rather homogenous without much fluctuation. Figures 4.5(c) and 4.5(d) present the amplitude and phase responses of the passive acoustic PT-symmetric medium over the studied spectrum, including reflection and transmission coefficients in the forward and backward directions. The difference of amplitudes between reflected waves r_f (forward-direction incidence) and r_b (backward-direction incidence) can be clearly observed over the simulated frequency range, with the contrast reaching maximum at the actual Bragg frequency near 2820 Hz [Fig. 4.5(c)]. Compared with the designed frequency 2858 Hz, there is a 38 Hz red shift. It is due to a slightly increased average refractive index of the passive PT-symmetric medium, arising from the removed negative half cycles of the square-wave modulation. The phase difference of

r_f and r_b experiences a π transition, from out-of-phase to in-phase, around the Bragg frequency [Fig. 4.5(d)], showing a typical PT phase evolution in terms of frequency. A transfer matrix calculation of the same model is also rendered in Figs. 4.5(c) and 4.5(d), which is in good agreement with the simulation result.

4.3.2 Acoustic metamaterials crystal design

Our theoretical analysis and numerical simulation have proved that a well-designed passive system still possesses PT-symmetric characteristics, even without gain medium. However, tailoring the loss behavior or the material properties in real space remains a tough challenge. Because the refractive index modulation respecting passive PT-symmetry should be of small amplitude, we need not only fine-tuned subwavelength structures for delicate manipulation of the effective properties, but also large amount of such structures for prominent performance. It differs from the design of conventional metamaterials (e.g. near-zero- or negative-index materials) whose function can be regarded as strong modulations of the dynamic properties.

During our design and the corresponding simulations for the real/imaginary part modulators, we directly replace the effective medium with metamaterials and perform a parametric sweep to fit the desired amplitudes and phases of the reflection and transmission coefficients simultaneously. This is reasonable as the scattering matrix of a passive and linear system is uniquely determined by the effective properties.

The real part modulation within an acoustic waveguide is achieved by introducing deep-subwavelength periodic grooves decorated on the waveguide walls, namely, the groove-structured inner surfaces, as depicted in Fig. 4.6(a). With this so-called groove-structured metamaterial for waveguide, the desired weak and accurate modulation of the real part of the refractive index part can be realized. FEM simulations for both the effective medium and actual structures are performed to examine the effectiveness. As

shown in Figs. 4.6(b) and 4.6(c), excellent agreement can be found between the two groups of simulation results, which verifies that the groove-structured metamaterials indeed function well as a real part modulation of the refractive index. Note that for the purely real or imaginary part modulation, the forward and backward reflections are identical as the system is spatially symmetric, and thus only one reflection coefficient is presented.

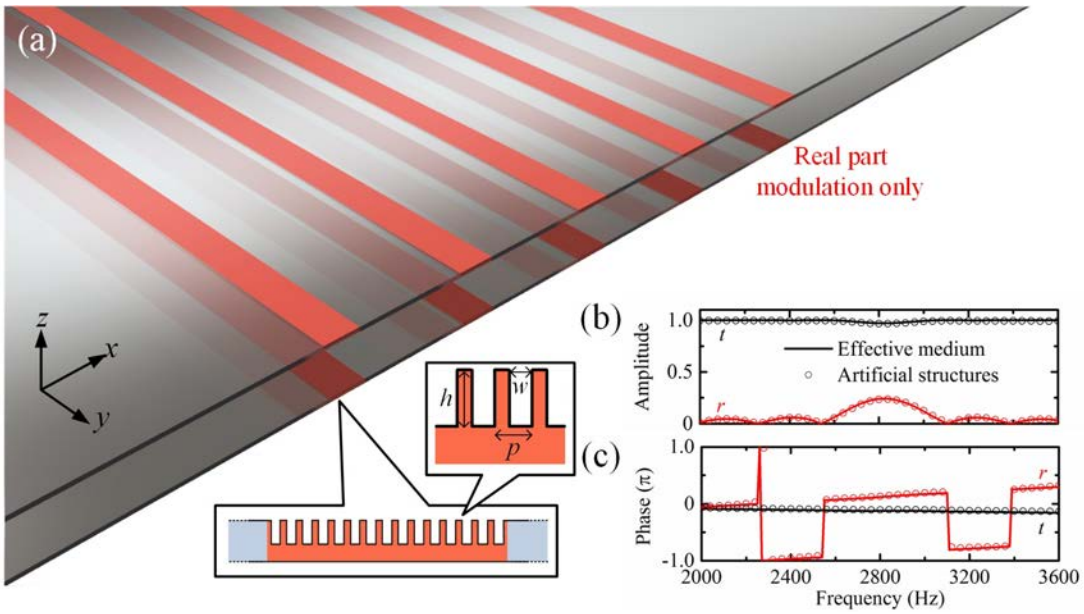

FIG. 4.6. Acoustic metamaterial design for the real part modulation. (a) Schematic of the groove-structured metamaterial [169]. (b) and (c) are the simulated amplitude and phase of the reflection (red) and transmission (black) coefficients. The results of both the effective medium (solid line) and the groove-structured metamaterial (circle) are included. The geometrical parameters of the grooves [inset of (a)] in the simulations are $w = 1.2$ mm, $h = 3$ mm and $p = 2$ mm.

For the modulation on the imaginary part demanded by our passive acoustic PT-symmetric medium, a deliberate control of sound loss is required. It has been revealed that the leakage induced by vent slits is feasible to acquire the attenuation effect, but only at a few specific frequencies [48]. According to the lumped element model, such structure is equivalent to a shunt resistor and a shunt inductor in series, resulting in the frequency-dependent leakage. It behaves as a high-pass filter for wave propagation in

waveguides. The associated complex acoustic impedance can be roughly estimated using the theories developed by Lord Rayleigh [170]. For arrangement with slits of 1-mm opening width, the reactance is comparable to or even larger than the resistance throughout the entire audio frequency range, giving rise to the inherent dispersion. However, the ideal loss medium with a fixed imaginary part of the refractive index ($n' \ll n_0$) is equivalent to a low-pass filter with a very smooth roll-off, which can be perceived from the simulation result given by Fig. 4.5(c). In order to modulate the sound loss with leakage structures in a relatively broader bandwidth, further steps are needed to reduce the frequency dependence of the acoustic impedance.

Our proposed leakage metamaterial consists of multiple holes connecting the waveguide with outside. For simplicity, we investigate the acoustic wave propagation within a short circular tube in which the fluid viscosity is considered. Based on the approximate solutions of the Kirchhoff theory [171] suggested by Zwikker and Kosten [172] and Maa [173], the acoustic impedance of the short tube can be expressed as

$$Z = R + iX = \begin{cases} \dfrac{32\eta t}{\pi d^4}\left(1 + i\dfrac{K}{6}\right), & K < 1 \\ \dfrac{32\eta t}{\pi d^4}\left(1 + \dfrac{K^2}{32}\right)^{1/2} + i\dfrac{4\omega\rho_0 t}{\pi d^2}\left[1 + \left(3^2 + \dfrac{K^2}{2}\right)\right], & 1 \le K \le 10. \\ \dfrac{16\sqrt{2}\eta t}{\pi d^4}K + i\left(\dfrac{4\omega\rho_0 t}{\pi d^2} + \dfrac{16\sqrt{2}\eta t}{\pi d^4}K\right), & K > 10 \end{cases} \quad (4.21)$$

where $K = 0.5d\sqrt{\omega\rho_0/\eta}$, η is the viscosity, d and t are the diameter and the thickness of the tube. It can be concluded from the equations that, as long as $K > 1$, both the resistance R and the reactance X are functions of frequency and the latter is non-negligible. Only when $K < 1$, R becomes a frequency-independent constant. The reactance is proportional to K, which indicates that the tube can be treated as a purely resistive acoustic component if the diameter is sufficiently small.

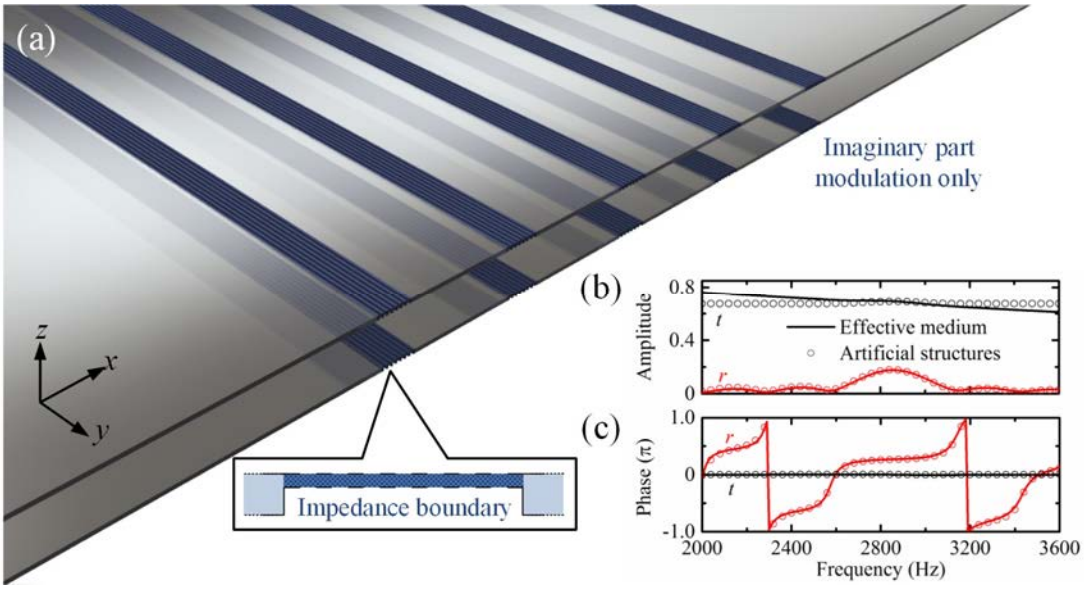

FIG. 4.7. Acoustic metamaterial design for the imaginary part modulation [169]. (a) Schematic of the acoustic metamaterial (impedance boundary equivalent to the holey-structured metamaterial). (b) and (c) are the simulated amplitude and phase of the reflection (red) and transmission (black) coefficients. The results of both the effective medium (solid line) and the acoustic metamaterial (circle) are included. The acoustic impedance is set as 4000 Pa·s/m.

The impedance boundary conditions are subsequently utilized during the holey-structured metamaterial design and simulation [Fig. 4.7(a)], through which the complex structures can be easily modeled by an effective acoustic impedance homogeneously distributed at the boundaries. This would largely reduce the computational consumption as the wavelength is more than one thousand times of the required hole diameter. As shown in Figs. 4.7(b) and 4.8(c), the reflection coefficient that results from the well-arranged impedance boundaries fits that of the effective medium well both in amplitude and phase. The amplitude of transmitted signal remains smooth and flat over the studied frequency range, intersecting the effective medium result near the Bragg frequency. As has been discussed above, the side-branch leakage that contains reactive components has a high-pass acoustic response. Hence the transmission curve resembles a straight line with positive slope. It is worth noting that the decrease of resistance-reactance ratio

would result in the increase of such slope, deviating the transmission curve from that of the suitable effective medium. Clearly, a purely resistive leakage is preferred for the imaginary part modulation in a broader bandwidth.

For further verification, the effective properties as functions of frequency are also retrieved, which are given in Fig. 4.8. The curves are obtained based on a standard retrieving procedure [174] in simulation. The imaginary part of the effective refractive index of the real part modulator is not exactly zero [squares in Fig. 4.8(a)] since we take into consideration the inherent losses within the grooves during the simulation. As expected, the results well fit our design target, namely, a balanced complex modulation with an amplitude of about 5%.

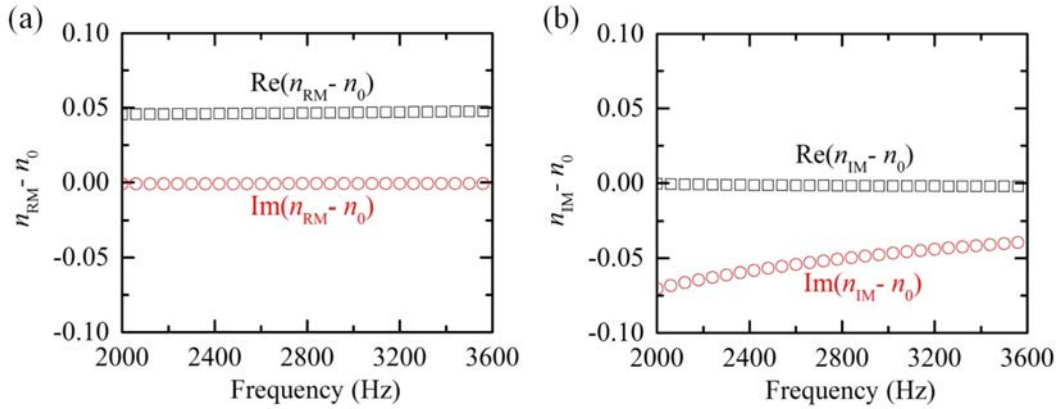

FIG. 4.8. Retrieved effective properties of the metamaterial modulators [169]. (a) Real part modulation (groove-structured metamaterial). (b) Imaginary part modulation (holey-structured metamaterial). n_{RM} and n_{IM} denote the retrieved complex refractive indices of the real and imaginary part modulations, respectively. Squares (black) and circles (red) respresent the real and imaginary parts of n_{RM} and n_{IM}.

Eventually we combine the two modulators into the form of a metamaterials crystal as illustrated in Fig. 4.9(a) and perform the full-wave simulation accordingly. The simulated energy density fields at 2820 Hz [Fig. 4.9(b)] match well with those of the effective medium [Fig. 4.5(b)]. Unambiguous interference fringe emerges only for the incidence in the forward direction, witnessed by the reflection spectra presented in Figs.

4.9(c) and 4.9(d). The transmission coefficient around the Bragg frequency is consistent with the result of effective medium simulation and becomes diverged as the frequency shifts away. Yet, the unique unidirectional reflection effect persists, leading to the obvious amplitude difference between the forward and backward reflections.

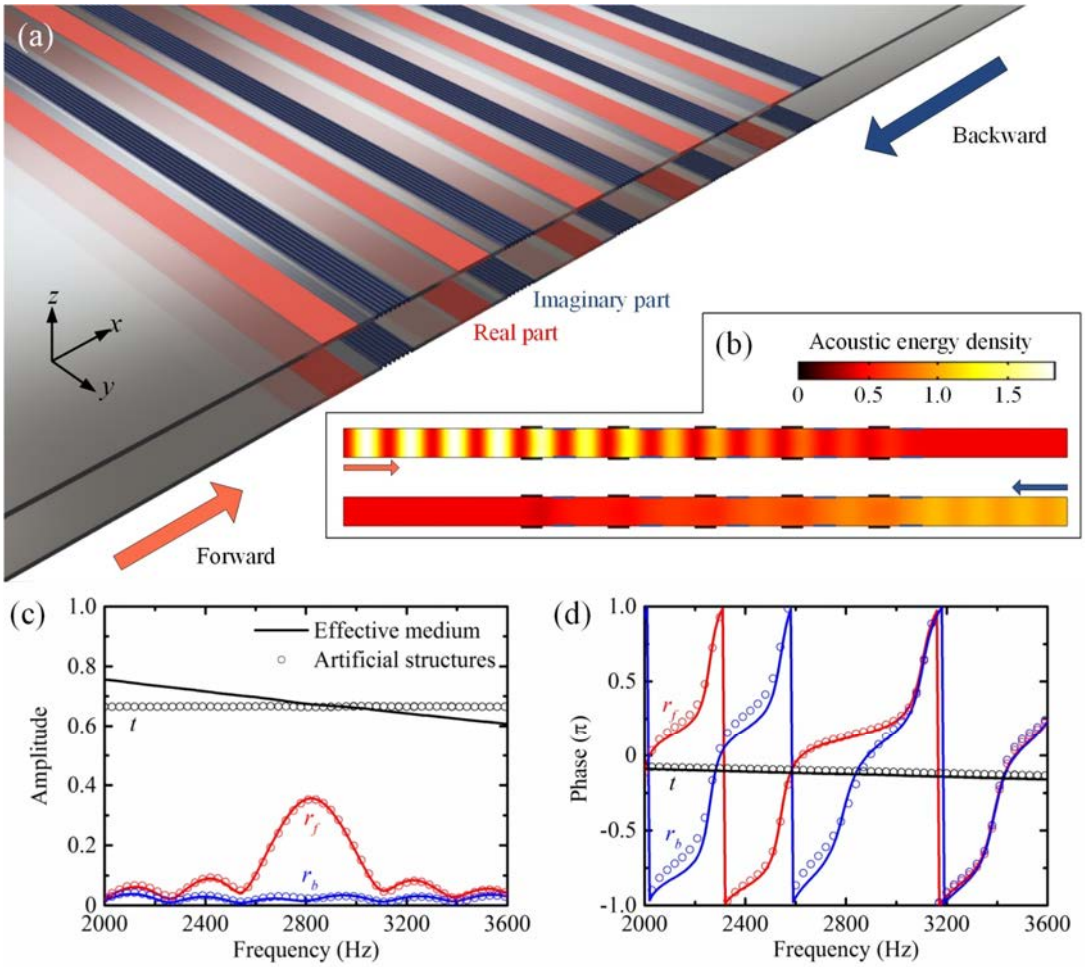

FIG. 4.9. One-dimensional passive acoustic PT-symmetric medium constructed by metamaterials [169]. (a) Schematic of the passive acoustic PT-symmetric metamaterials crystal merging the real (red) and imaginary (blue) part modulations. (b) Simulated energy density fields in *xz*-plane for forward and backward incidences. The amplitude is normalized per the background field. (c) and (d) are the spectral amplitude and phase responses, including reflection (red, forward; blue, backward) and transmission (black) coefficients in both directions. The solid lines and circles denote the results of the effective medium and the acoustic metamaterials, respectively.

4.4 Interaction between unpaired wave vectors and oblique incidences

Before extending the passive PT-symmetric potential in two-dimensional space to realize the unidirectional focusing effect, the interplay between unpaired wave vectors and oblique incidences is explored in this section. We present two numerical examples to demonstrate that, strong reflection takes place when the incidence wave vector $\boldsymbol{k}_i$, the reflection wave vector $\boldsymbol{k}_r$, and the unidirectional wave vector $\boldsymbol{q}$ provided by the passive PT-symmetric modulation satisfy the rule of two-dimensional vector addition, namely, the so-called wave-vector matching condition [175]. Otherwise, the mismatched wave vectors hardly generate any reflection. For the following numerical examples, the passive PT-symmetric medium is immersed in air and occupies a rectangular area, in which the passive PT-symmetric potential is designed to be along a specific direction non-parallel to the incident acoustic waves.

In numerical example 1, the passive PT-symmetric medium is constructed using 9 pairs of complex modulations with a modulation amplitude of 3% to provide an unpaired wave-vector of magnitude $\sqrt{2}k_0$ towards lower left (45° to the horizontal), as shown in Fig. 4.10. The complex modulation of refractive index is based on the one-dimensional configuration in Fig. 4.5. It satisfies wave-vector matching condition for the incidence of wavenumber k_0 (4042.3 Hz) pointing to the $+x$ direction. As shown in Fig. 4.10(a), a side-way scattering can be observed, which is not determined by the shape of the medium, but the unpaired wave vector offered by the passive PT-symmetric potential. For wave propagating in the reverse direction, there is no side-way scattering [Fig. 4.10(b)].

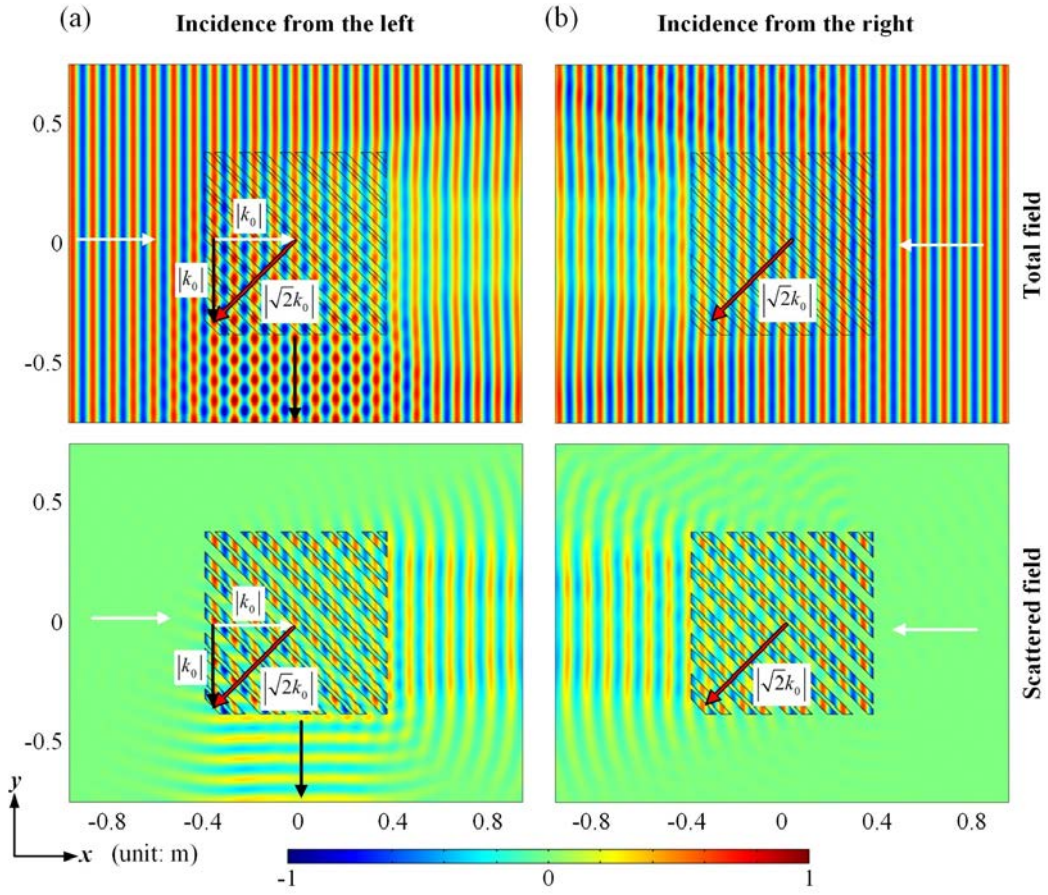

FIG. 4.10. Interaction between unpaired wave vectors and incidence (example 1: unidirectional side-way scattering) [169]. Total (upper) and scattered (lower) acoustic pressure fields for incidences (a) from the left and (b) from the right. The passive PT-symmetric medium provides an unpaired wave-vector of magnitude $\sqrt{2}k_0$ towards lower left (red arrows, 45˚ to the horizontal). The white and black arrows denote the incidence and reflection directions. All the amplitudes are normalized per maximum.

In numerical example 2, the designed passive PT-symmetric medium consists 9 pairs of complex modulations with a modulation amplitude of 3%, which provides a unidirectional wave vector of magnitude k_0 that is 60˚ to the horizontal, as shown in Fig. 4.11. Again, the complex modulation follows the one-dimensional configuration given in Fig. 4.5. The wave-vector matching condition is satisfied when the acoustic wave of wavenumber k_0 (5716.7 Hz) is incident from the left-hand side [see Fig. 4.11(a)], leading to a nontrivial phenomenon of forward scattering. On the contrary, for

acoustic wave propagating in the reverse direction as presented in Fig. 4.11(b), the forward scattering phenomenon does not happen.

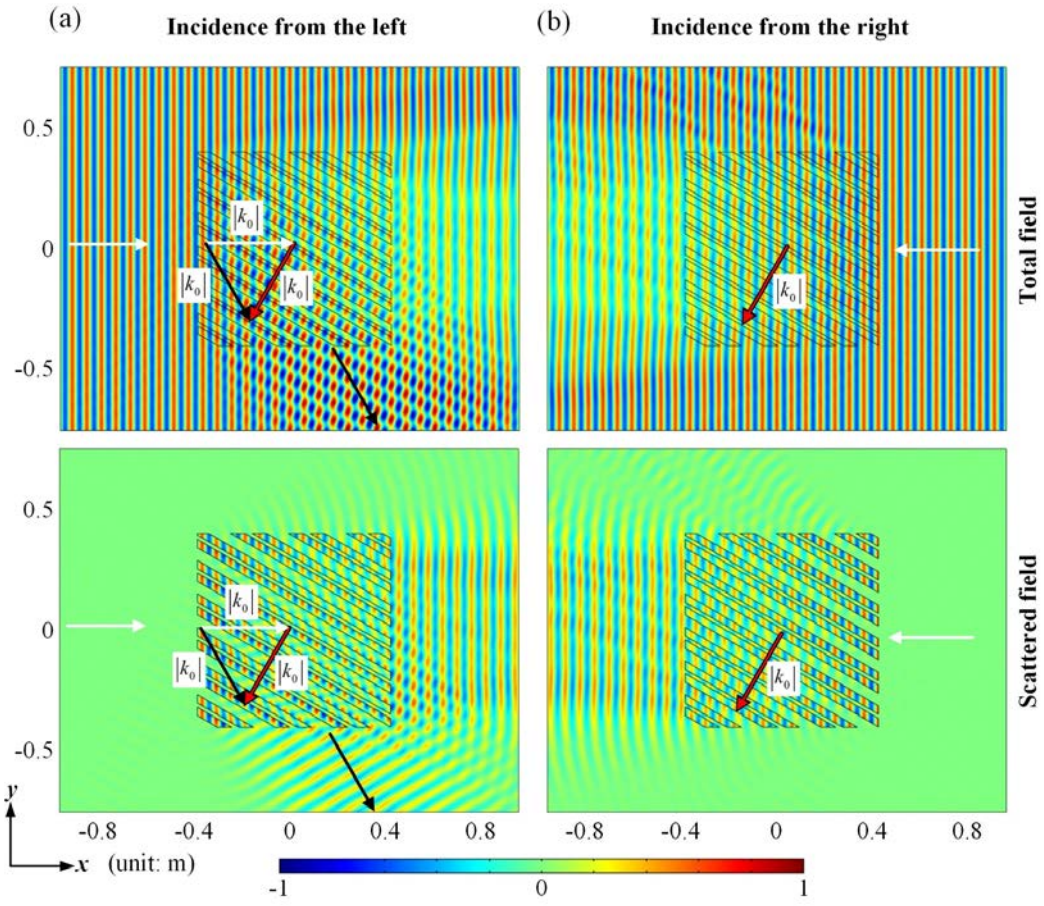

FIG. 4.11. Interaction between unpaired wave vectors and incidence (example 2: unidirectional forward scattering) [169]. Total (upper) and scattered (lower) acoustic pressure fields for incidences (a) from the left and (b) from the right. The passive PT-symmetric medium provides an unpaired wave-vector of magnitude k_0 towards lower left (red arrows, 60˚ to the horizontal). The white and black arrows denote the incidence and reflection directions. All the amplitudes are normalized per maximum.

4.5 Unidirectional sound focusing based on directional wave-vector matching

4.5.1 Extending parity-time-symmetric potential in two-dimensional space

As shown in Fig. 4.12, by curling the one-dimensional passive PT-symmetric potential circumferentially, the resultant passive acoustic PT-symmetric medium in two-dimensional space offers radial unidirectional wave vectors for incoming sound

waves, through modulating the acoustic refractive index along the radial direction,

$$\Delta n(r) = n' \exp[iq(r - r_0)], \quad n' \ll n_0 \tag{4.22}$$

where r_0 is the starting radius of the PT-symmetric potential sector.

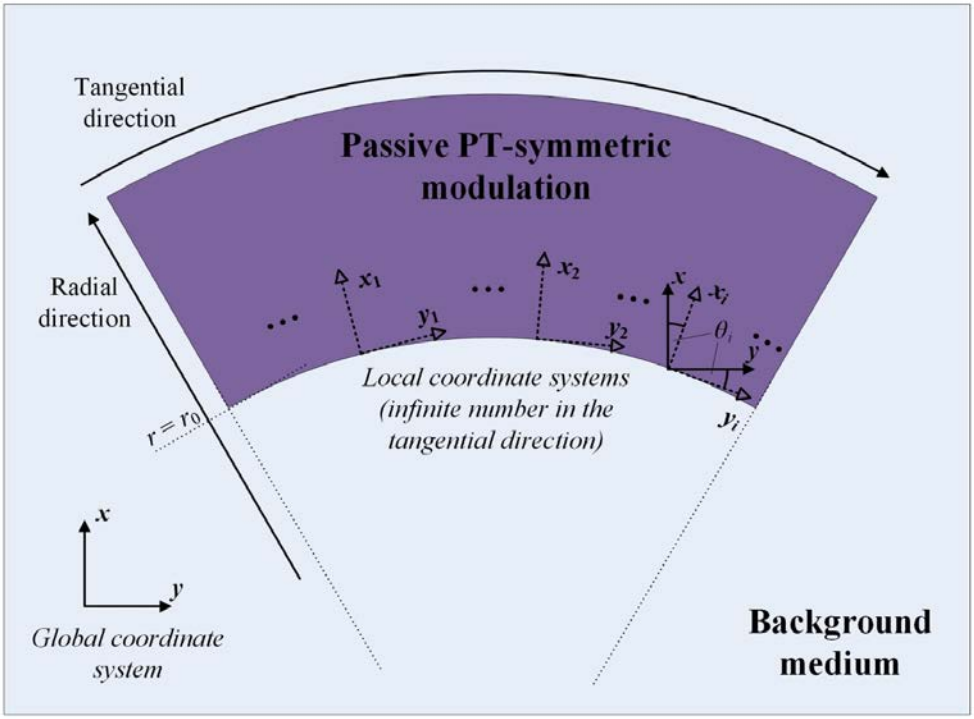

FIG. 4.12. Schematics of the global and local coordinates in two-dimensional space for the studied passive PT-symmetric medium [169]. The purple area denotes the passive PT-symmetric medium, where the complex index is modulated along the radial direction but uniform along the tangential direction. Define global coordinate system (x-y), and local coordinate systems (x_i-y_i, i=1, 2, …). In each local coordinate system, the modulation offers a one-dimensional passive PT-symmetric potential along x_i.

Now let us explain how such extension is implemented. In a two-dimensional plane of global coordinates (x-y), we can define local coordinates (x_i-y_i, i=1, 2, …), e.g. the local coordinates x_1-y_1 and x_2-y_2 as shown in Fig. 4.12. Here, a passive PT-symmetric structure with balanced real-imaginary-part modulations is designed along the local coordinates of x_i. Here, the P operator in each local coordinate is acting in the same

way as the one in a one-dimensional system, *viz.*, $P:\hat{p}(x_i)\to-\hat{p}(x_i),\ x_i\to-x_i$. Note that those local coordinates are not necessarily parallel with each other. The action of P operator in the global coordinates (*x*-*y*) can be deduced from the coordinate transformation

$$\begin{aligned} x_i &= x\cos\theta_i + y\sin\theta_i, \\ y_i &= -x\sin\theta_i + y\cos\theta_i, \end{aligned} \tag{4.23}$$

where θ_i is the angle between x_i and x. As a result, the action of P operator in the two-dimensional case is obtained as

$$\begin{aligned} P:\hat{p}(x\cos\theta_i + y\sin\theta_i) &\to -\hat{p}(x\cos\theta_i + y\sin\theta_i), \\ x\cos\theta_i + y\sin\theta_i &\to -x\cos\theta_i - y\sin\theta_i. \end{aligned} \tag{4.24}$$

Basically, there exist an infinite number of ports in two-dimensional system. For simplicity, we only consider the ports along certain directions, e.g. x_1 and x_2. It is worth mentioning that this is a different treatment compared to the transformation acoustics as we are not trying to map a rectangular-shaped domain into a fan-shaped domain, which would result in radially dependent material parameters. What studied is a curved passive PT-symmetric potential in two-dimensional space where the balanced real and imaginary part modulations are preset to be radius-independent in both local and global coordinates. Here only an operation of rotation is conducted, without distorting the space. As shown in Fig. 4.13, the complex modulation of refractive index along the radial direction is the same as the one-dimensional configuration in Fig. 4.5 (5 modulation periods with a modulation amplitude of 5%). It provides unpaired wave vectors of magnitude $2k_0$ pointing to the intersection of x_1 and x_2 axes. The incident waves with a wavenumber of k_0 experience one-way reflectionlessness when propagating along x_1 and x_2, which indicates the unidirectional reflectionless resonance happened nearby an exceptional point [149].

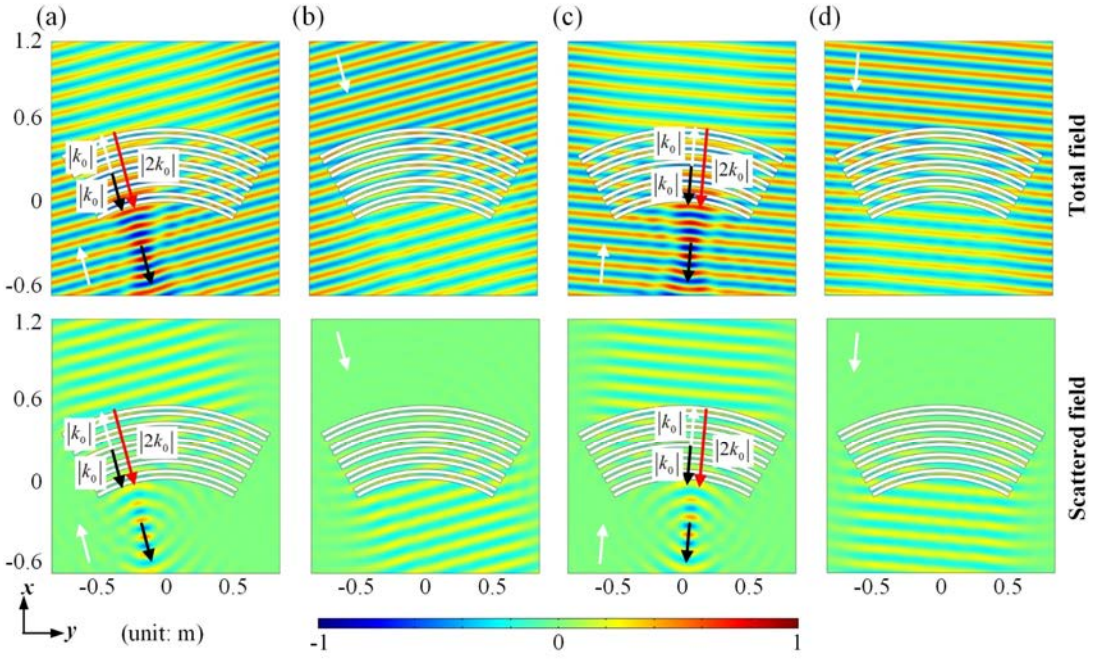

FIG. 4.13. Unidirectional reflectionlessness for the passive PT-symmetric medium extended in two-dimensional space [169]. Incident angles: (a) –15˚, (b) 165˚, (c) 5˚, and (d) 185˚. The white, black, and red arrows represent the incident, the reflected, and the unpaired modulation wave vectors, respectively. For each incidence, both the total (upper) and scattered (lower) acoustic fields are presented, which are normalized per maximum.

4.5.2 Directional wave-vector matching and its implementation

As illustrated in Fig. 4.14, the passive acoustic PT-symmetric metamaterials crystal curved in two-dimensional space is realized through interleaving two different types of passive metastructures along the radial direction inside a planar acoustic waveguide between two rigid plates: the groove-structured and the holey-structured acoustic metamaterials, arranged in such a way that they form a circumferentially expanded Bragg reflector. Subtle combination of the two metamaterials offers balanced real and imaginary part modulations, required by the passive PT-symmetric potential, to the refractive index. This complex modulation creates an unpaired wave vector [149,152] $\boldsymbol{q} = -2k_B\boldsymbol{r}/r$ towards the sector center. Here k_B is the wavenumber at the Bragg

frequency $f_B = c_0 / 2T$, where the Bragg resonance happens, with c_0 and T being the speed of sound and the lattice constant, respectively.

For the unidirectional reflectionlessness phenomenon in one-dimensional scenario as we discussed in Section 4.3, when the operating frequency f is away from f_B, the incidence wave vector $\boldsymbol{k}_i$, the reflection wave vector $\boldsymbol{k}_r$, and the unidirectional wave vector $\boldsymbol{q}$ provided by the complex modulation are mismatched for both forward and backward incidences, giving rise to a trivial bidirectional reflectionless effect. When the system operates at f_B, the wave-vector matching condition $\boldsymbol{k}_r = \boldsymbol{q} + \boldsymbol{k}_i$ ($|\boldsymbol{k}_i| = |\boldsymbol{k}_r| = k_B$) is satisfied only along the forward direction, leading to a nontrivial effect of unidirectional reflectionlessness. For the proposed passive acoustic PT-symmetric metamaterials crystal in two-dimensional space, the wave-vector matching obeys the rule of vector addition [175] and thus strong specular reflection occurs at particular positions where $\boldsymbol{k}_i$, $\boldsymbol{k}_r$, and $\boldsymbol{q}$ (that are not necessarily parallel) become matched [the inset of Fig. 4.14(a)], allowing the frequency of reflection to be possibly higher than f_B ($|\boldsymbol{k}_i| + |\boldsymbol{k}_r| > |\boldsymbol{q}|$ when $f > f_B$), so that the unidirectional focusing phenomenon can be observed over the spectrum (see Appendix B). Note that such wave-vector match does not require the local incident angle to be small with respect to the unpaired wave vector $\boldsymbol{q}$ as has been demonstrated in Section 4.3, and thus it is not simply the case of paraxial wave propagation in one-dimensional PT-symmetric medium, but rather a physical problem of the interaction between incident waves and passive PT-symmetric potential in a two-dimensional space.

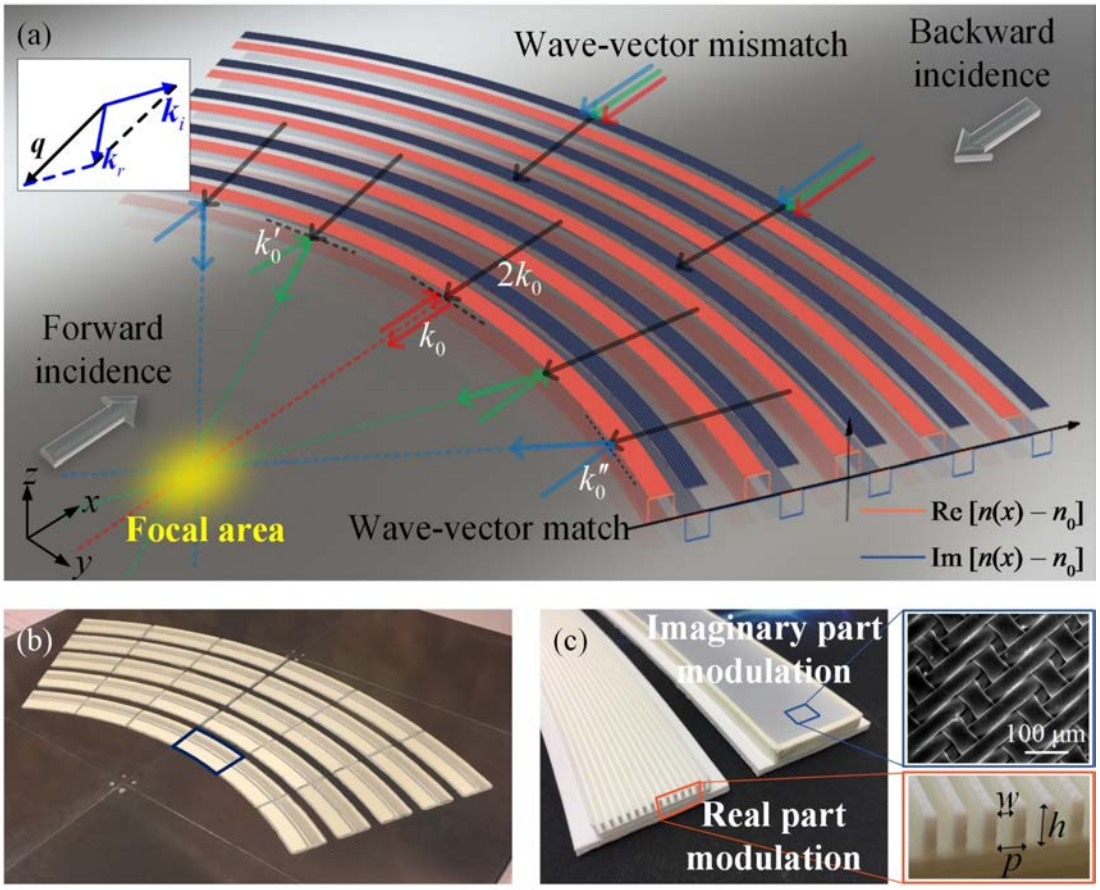

FIG. 4.14. All passive acoustic PT-symmetric metamaterials crystal [169]. (a) Unidirectional focusing based on directional wave-vector matching. The upper-left inset illustrates the two-dimensional wave-vector matching $\boldsymbol{k}_r = \boldsymbol{q} + \boldsymbol{k}_i$. For different spatial frequencies $k_0(\text{red}) < k_0'(\text{green}) < k_0''(\text{blue})$, the reflections exist at different areas along the arc to form focused sound field. The wave vectors are mismatched for backward incidence, thus leading to no reflection. (b) The fabricated acoustic metamaterials crystal. The circumferential opening angle 60° in the *xy*-plane is divided into 6 segments of equal opening angle 9.7°. The waveguide height is $H = 20$ mm. (c) The real and imaginary part modulations. Real part modulation (lower-right inset: enlarged photo): groove-structured metamaterial of $w = 1.2$ mm, $h = 3$ mm and $p = 2$ mm. Imaginary part modulation (upper-right inset: scanning electron microscope image): holey-structured metamaterial, *viz*., the 60-μm-thick mesh fabrics. The average pore size and open area are 7 μm and 2%. Its acoustic impedance is about 4000 Pa·s/m.

In experiment, the rigid plates are carved with curved slot openings for the

installment of the index modulators [see Fig. 4.14(b)]. The real part modulation is realized by the 3D-printed groove-structured metamaterials sketched in Fig. 4.14(c), which is able to decelerate sound waves as we have presented in Section 4.3. The imaginary part modulation can be accomplished through purposely introduced sound leakage, similar to the radiative losses in optical systems [176]. Slit structures have been demonstrated for such purpose, but with strong dispersion and changed real part of refractive index [48]. Instead the holey-structured acoustic metamaterials, namely, the commercial mesh fabrics, are used here, as shown in Fig. 4.14(c). The deep-subwavelength pores are homogeneously distributed so that they guarantee nearly purely resistive impedance boundary and precise leakage control, leading to almost nondispersive loss, without affecting the real part of index. It would enable the approximately-balanced modulation in a relatively broader bandwidth.

4.5.3 Sample fabrication and experimental setup

The parameters of the holey-structured metamaterials that satisfy the imaginary part modulation can be evaluated based on Eq. (4.21). The hole diameter d must be smaller than 30 μm to guarantee a sufficiently large resistance-reactance ratio (*e.g.*, $R/X > 10$) around the Bragg frequency of 2820 Hz. Therefore, we choose the mesh fabrics [Fig. 4.15(a)], which are woven with monofilament fibers (Saatifil Acoustex HD7), as the holey-structured metamaterial modulator. As shown in the scanning electron microscope image given by Fig. 4.15(b), this type of material has controllable acoustic impedance governed by the uniformly distributed pores that can be precisely manufactured on micron-scale. The overall acoustic impedance is determined by mean of the flow resistance measurement.

As exhibited in Fig. 4.15(a), the real part metamaterial modulator and the frameworks of the imaginary part metamaterial modulator are fabricated using additive

manufacturing based on fused deposition modeling. The base material is polylactic acid, which can be treated as rigid for airborne sound due to the large contrast in acoustic impedance. The mesh fabrics for imaginary part modulation are firmly attached to the framework with glues. The contact edges are covered with adhesive paper to avoid any possible gap. While such materials are thin and flexible, the vibroacoustic coupling is extremely weak and no resonance behavior is observed in practice.

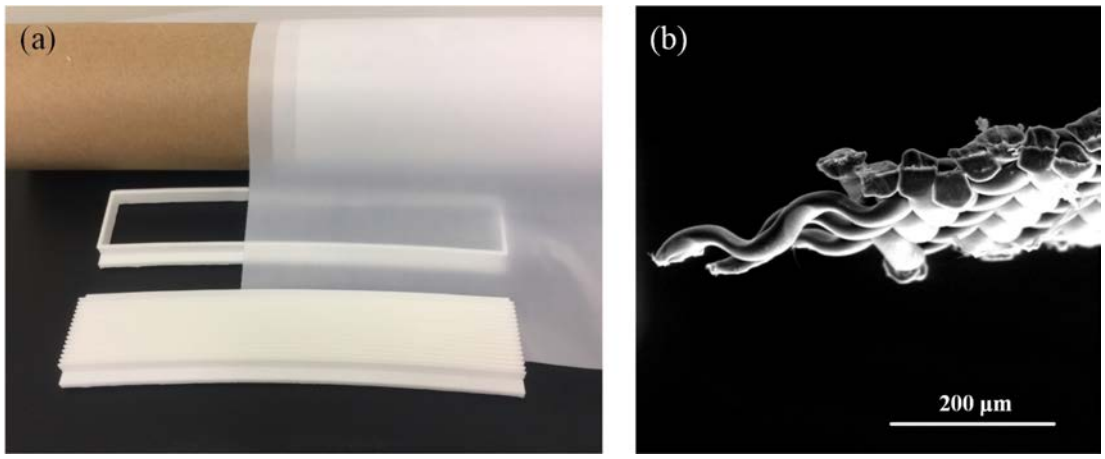

FIG. 4.15. The metamaterial samples used to construct the passive acoustic PT-symmetric metamaterials crystal [169]. (a) The groove-structured metamaterial is used for real part modulation, while the mesh fabrics attached on frame provides imaginary part modulation. (b) The scanning electron microscope image of the mesh fabrics side view.

The experimental setup is shown in Fig. 4.16. The computer controls an automated scanning system via LabVIEW. The lock-in amplifier (Zurich Instrument HF2LI) is used for signal generation and acquisition. A series of continuous sinusoidal signals sweeping from 2500 Hz to 3200 Hz are sent to the audio power amplifier (Brüel & Kjær type 2716C) before being applied to the transducer array that consists of 36 identical 1.5-inch full-range loudspeaker units (Peerless by Tymphany PMT-40N25AL01-04). The center-to-center distance between two neighboring speaker units is 40 mm so that the array can effectively generate nearly plane acoustic waves travelling inside the waveguide.

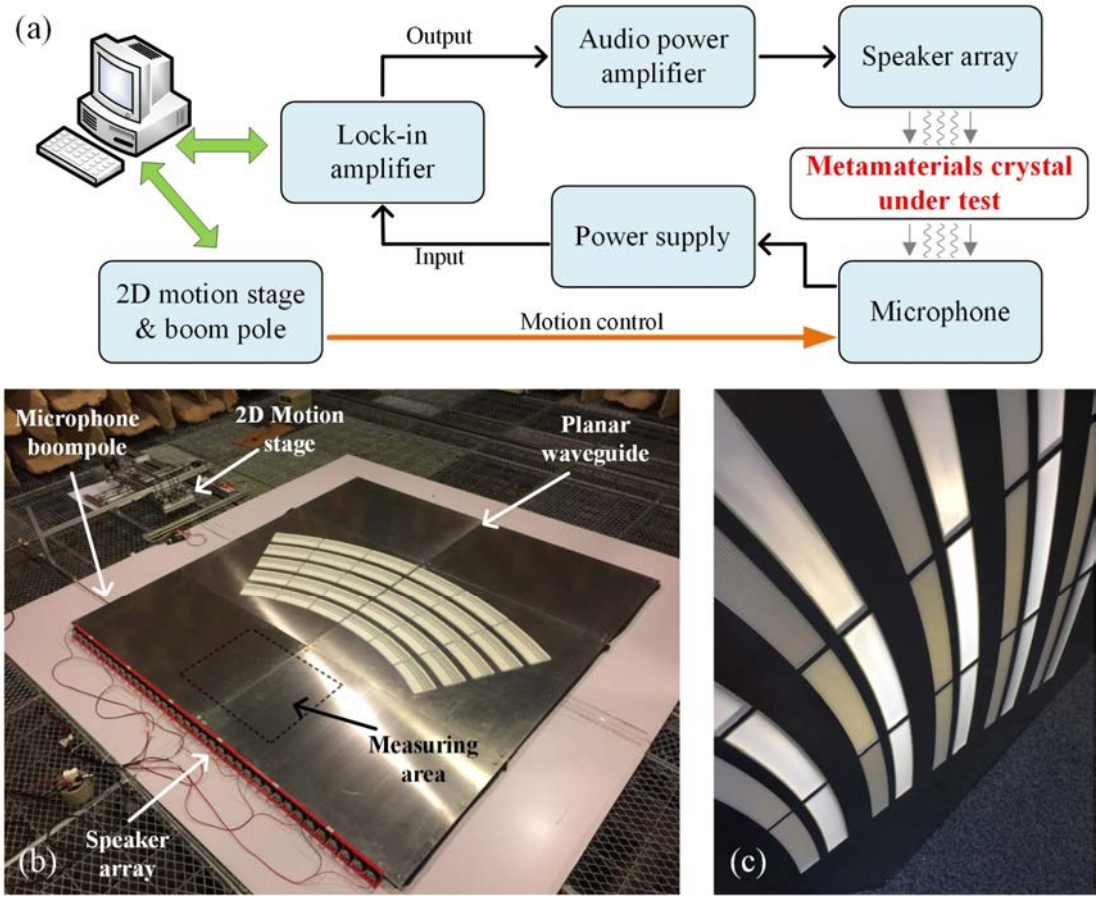

FIG. 4.16. Experimental measurement of the passive acoustic PT-symmetric metamaterials crystal [169]. (a) Working flow of the measurement. (b) Photo of the experimental arrangement in an anechoic chamber. The dashed rectangle denotes the measuring area inside the waveguide. (c) Inner surface of the plate mounted with the mesh fabrics and the groove-structured metamaterials.

The acoustic pressure fields inside the waveguide are scanned using a micro-electro-mechanical microphone (GoerTek Inc. S08OT421). The microphone is very small in size (3.8 mm×3.0 mm×1.1 mm) and installed at the end of a 3-mm diameter slender boompole, whose movement is controlled by the motion stage. The total measured area is 400 mm×400 mm, with a spatial resolution of 10 mm that is less than one-tenth of the shortest wavelength. The recorded signals are sent back to the lock-in amplifier via a pre-amplifier.

Since the studied model is symmetric along the z direction, we may simplify the experimental implementation by constructing only half the waveguide structure and

replacing the symmetry plane with a rigid boundary (i.e. waveguide height becomes $H = 20$ mm for single-side meta-structures rather than $2H = 40$ mm for double-side meta-structures). In this sense, a total of 60 pieces (30 pairs) of the metamaterial samples, including the groove-structured metamaterials for real part modulation and the mesh fabrics for imaginary part modulation, are mounted on the slots of the aluminum top plate [Fig. 4.16(b)], forming an integrated waveguide along with the rigid middle density fiberboard at the bottom. The sample positions are carefully adjusted so that they can be in alignment with the inner surface of the plate [Fig. 4.16(c)]. The waveguide height is guaranteed by inserting several adjustable supports between the two plates. Sealing putty is utilized to prevent waveguide leakage other than those intentionally introduced through the mesh fabrics. In addition, to alleviate the reflections from the waveguide openings, sound absorbing materials are arranged around the sound field inside the waveguide. All the equipment and samples are placed in an anechoic room so that high signal-to-noise ratio can be obtained.

4.5.4 Experimental results

Full-wave FEM simulations and experimental measurements have been conducted to test our hypothesis. Figure 4.17(a) presents the normalized sound energy density fields for both incidences at 3000 Hz, in which the simulated and measured results agree well with each other. Remarkable contrast of the responses in opposite directions can be observed from the interference patterns within the measurement areas, marked by the white boxes. Strong reflections only occur at the positions that satisfy the wave-vector matching condition. In other words, not all unpaired wave vectors provided by the passive PT-symmetric structure interact with incident waves in two-dimensional space.

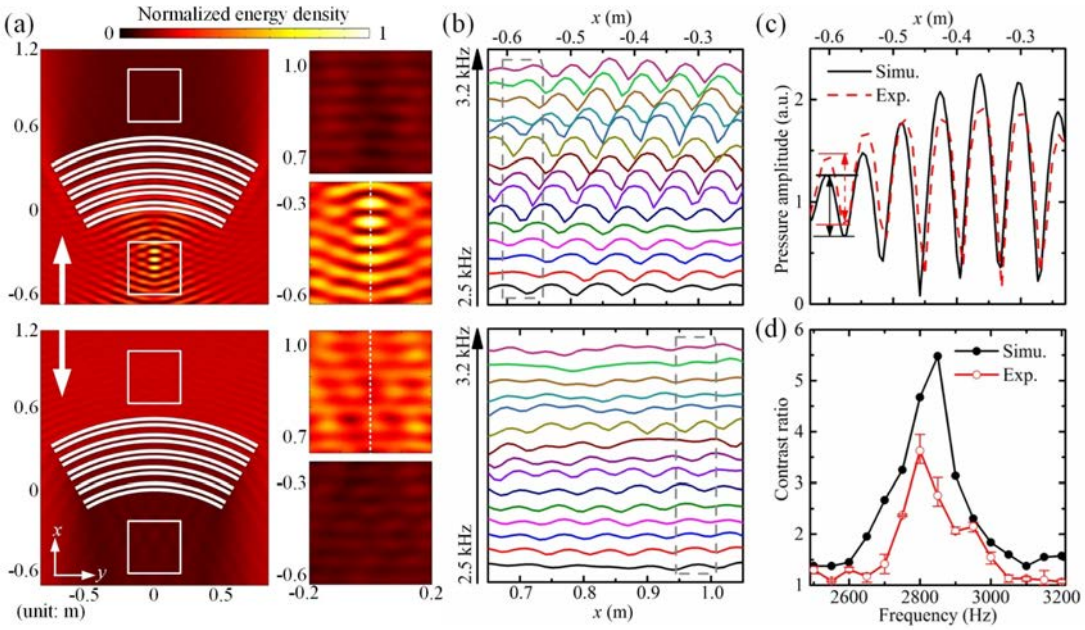

FIG. 4.17. Unidirectional reflection and focusing [169]. (a) Simulated (left) and measured (right) acoustic energy density fields for the forward (upper) and backward (lower) incidences at 3000 Hz. The white boxes mark the measurement areas. The arrows denote the incidences. (b) Absolute acoustic pressure distributions for forward (upper) and backward (lower) incidences, along the dashed lines marked in (a). The dashed rectangles indicate the areas where the standing-wave ratios G_f and G_b are extracted. (c) Simulated and measured standing wave patterns at 3000 Hz for forward incidence. The red/black arrow marks the peak and valley employed to calculate G_f and G_b in experiment/simulation. (d) Extracted contrast ratio G_f/G_b versus frequency. The error bars are generated from four repeated measurements.

To validate that the focusing effect is indeed due to the unpaired wave vectors offered by the passive PT-symmetric metamaterials crystal instead of simply the geometric shape of the concave surface, the measured sound pressure distributions at different frequencies along $y=0$ are presented in Fig. 4.17(b). The overall amplitude of the standing wave fields is frequency-dependent for forward incidence [Fig. 4.17(b), the upper sub-figure], while being relatively stable and frequency-independent for backward incidence [Fig. 4.17(b), the lower sub-figure]. In contrast, it is not difficult to imagine that, when the metamaterials crystal is replaced by a rigid concave reflector,

the overall amplitude of the standing-wave fields would in both directions would be independent to the frequency within the studied spectrum (see Appendix C).

Nearby the exceptional point, the system is strongly reflective from one side but almost reflectionless from the other. Here, the forward and backward standing-wave ratios G_f and G_b, *viz*., the ratio between the peak and valley values of the standing-wave fields [Fig. 4.17(c)], are extracted to evaluate the reflection strengths in both directions. The contrast ratio G_f / G_b plotted in Fig. 4.17(d) can thus be utilized to estimate the contrast between the two reflections. Note that the interference pattern is a result of the superposition between the incident plane waves and the reflected waves propagating in all possible directions. To reduce the disturbance of reflections from the positions other than $y = 0$, G_f is extracted in the area away from the focal spot [dashed rectangles in Fig. 4.17(b)], where the reflected waves diverge, and the normal reflection dominates. In Fig. 4.17(d), the peak serves as an indicator to show that the contrast between forward and backward reflections reaches maximum, which occurs nearby exceptional point. Another way to further confirm the one-way wave-vector matching behavior is by simply reversing the complex modulation, that is, by switching the reflective and the reflectionless sides. In this scenario, the concave surface would only generate very weak focusing effect (see Appendix B).

The acoustic focusing effect over a relatively wide spectrum enabled by directional wave-vector matching is further confirmed using the simulated scattered energy density fields as presented in Fig. 4.18(a). At 2500 Hz, lower than the Bragg frequency f_B, the existing wave-vector mismatch hardly induces any reflection for the forward incidence. As the frequency approaches and eventually surpasses the Bragg frequency f_B, the wave-vector matching condition becomes approximately satisfied within the two-

dimensional plane, giving rise to clear reflections and the resultant focused sound field. The experimentally measured interference patterns shown in Fig. 4.18(b) are remarkably frequency-dependent, which is a strong evidence of the reflection wavefront change [see dashed arrows in Fig. 4.18(b)]. The simulated scattered energy density distributions along $x = -350$ mm and $y = 0$ mm [dashed lines in Fig. 4.18(a)] for multiple operating frequencies are displayed in Figs. 4.18(c) and 4.18(d) as well. Clearly, the focal spots locate within a small area over the studied spectrum.

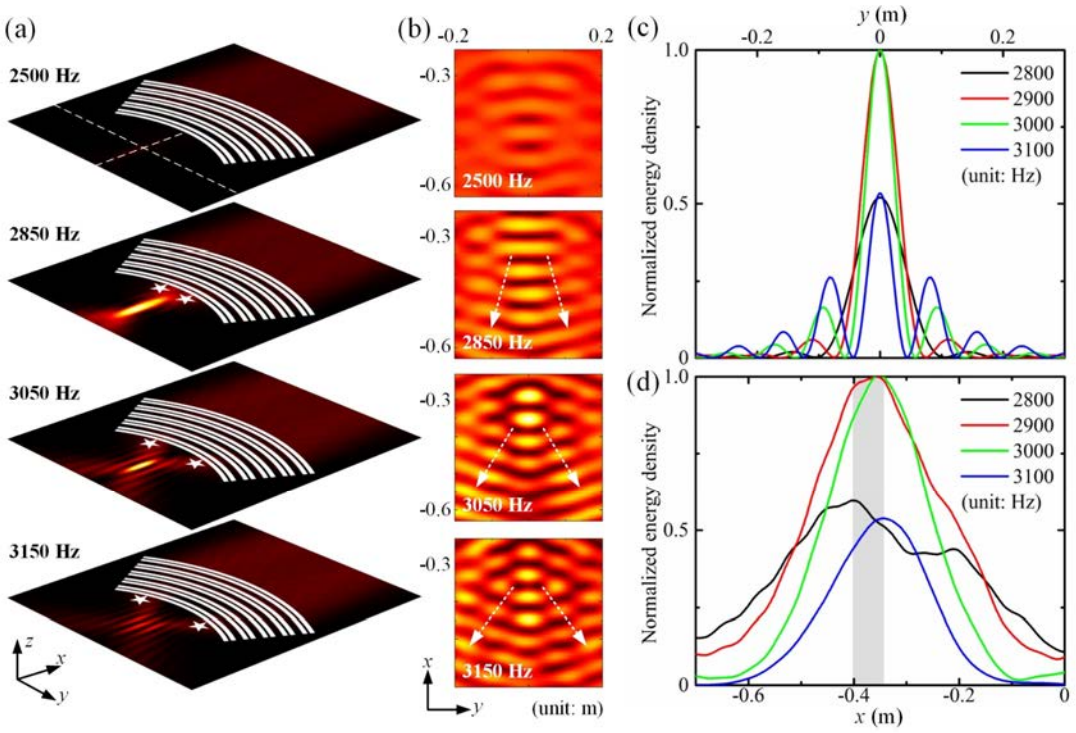

FIG. 4.18. Unidirectional sound focusing over spectrum [169]. (a) Simulated scattered energy density fields at four operating frequencies: 2500 Hz, 2850 Hz, 3050 Hz, and 3150 Hz. For different frequencies, strong reflections occur at different locations, marked by the white asterisks, to form focal areas. (b) Measured total energy density fields for the forward incidence at frequencies shown in (a). The interference pattern varies with frequency due to the change of reflected wavefront normal, indicated by the white arrows. (c) and (d) Simulated scattered energy density distributions along the dashed lines $x = -350$ mm and $y = 0$ mm in (a). All the curves are normalized per maximum. The shadow area in (d) indicates the spatial range of focal zones at multiple frequencies.

4.6 Summary

In summary, modulating refractive index in complex plane enables the study of PT symmetry with acoustic systems. In contrast to the balanced gain-loss configurations that require gain medium or external intervention, our all passive acoustic metamaterials crystal offers intrinsic PT-symmetric potential to create unpaired wave vector via complex modulation of the effective refractive index. By expanding the potential in two-dimensional space, it is consequently able to demonstrate the exceptional point as well as the unidirectional acoustic focusing effect over a certain bandwidth. In addition, the zero cut-off of such acoustic PT-symmetric system makes it much easier to extend PT symmetry study in multi-dimensional space, which remains a great challenge in other classical wave systems. To further realize a genuine two-dimensional passive PT-symmetric system, one may synthesize multiple passive PT-symmetric potentials together so that the material can simultaneously offer varies unpaired wave vectors to incident waves (see Appendix D). Our demonstration provides a new degree of freedom to the implementation of unique wave dynamics, and at the same time paves the way towards practical investigation of general quantum-analogs phenomena beyond one-dimensional waveguide configuration.

Chapter 5: Conclusion

This thesis has studied the meta-structured surfaces for airborne guided acoustic mode, and the corresponding functionalities and applications including acoustic rainbow trapping (ART), subwavelength sound focusing/imaging, and unidirectional wave vectors manipulation. Meanwhile, it has also been highlighted that well-tailored losses can be used to explore passive parity time (PT) symmetry in acoustic system.

In Chapter 2, a type of gradient holey-structured metasurfaces has been proposed to achieve ART effect with controllable trapping pattern. Such metasurfaces allow broadband sound grazing the metasurfaces to be converted into a surface acoustic mode travelling in gradually vanished group velocity, giving rise to spatial-spectral separation and strong compression governed by both the frequency and the gradient profile. The effect of the inherent visco-thermal losses inside the holes has also been investigated to evaluate the performance of the metasurface in real life. Our analysis has shown that the inherent losses contribute to an anomaly of the group velocity distribution at the trapping position, accompanied by progressively increased attenuation along the wave propagation direction. Accordingly, the intense backscattering observed in the lossless case, due to the mode conversion between the bidirectional waves, is no longer remarkable. This so-called absorptive ART effect deepens our understanding about the structure-induced surface acoustic waves (SSAWs) at a lossy metasurface and is a significant step towards the practical introduction of ART-based devices. It may also be utilized to construct broadband absorptive metasurfaces for hypersonic boundary layer stabilization [80,81].

In Chapter 3, the thesis has experimentally presented the subwavelength focusing and imaging effects enabled by a gradient-index (GRIN) metasurface via the SSAWs with large wave vectors. The GRIN metasurface design has been significantly

simplified because of the straightforward correlation between the hole depth and the required index values. Such design method may be further applied to other GRIN devices [134], e.g. acoustic Eaton lens, Luneburg lens, Maxwell-fish-eye lens and black hole. Functionalities such as airy beam and Talbot effect under conformal transformation [136], can also be realized with a similar configuration. Meanwhile, even deeper subwavelength scale would be available if the unit cells are spatially coiled [14,137] or helically structured [138]. In addition, the system is open to the surrounding environment and the confined sound field is measurable in the upper half-space. It is thus an ideal platform to experimentally observe, characterize and investigate the propagation and energy flow of sound "inside" the metamaterials or sonic crystals counterparts. For instance, the phenomenon of backscattering-immune wave guiding in an acoustic topological insulator is able to be visualized with experiment in the subwavelength regime through measuring the topological surface acoustic polaritons [101], which is still a difficult task for bulk composites or structures. Moreover, the coupling between the non-leaky surface mode and a radiative mode is possible through acoustic antennas [86,100]. It may enable more flexible ways of sound manipulation and open new possibilities to innovative applications for acoustic focusing, imaging, sensing and detection beyond the diffraction limit.

In Chapter 4, we have shown that the proposed acoustic metamaterials crystal provides intrinsic passive parity-time-symmetric (PT-symmetric) potential to generate unpaired wave vector through modulating the effective refractive index in complex domain. By two-dimensionally expanding the potential, the exceptional point and the associated unidirectional sound focusing effect (along with reflectionless acoustic transparency in the opposite direction) can be observed over a certain bandwidth. The absence of cut-off in such acoustic PT-symmetric system suggests a feasible way to

extend general PT symmetry study to multi-dimensional space, which remains a great challenge in experiment with other classical wave systems. To further construct a genuine two-dimensional passive PT-symmetric material, one may synthesize multiple passive PT-symmetric potentials into one compact region so that the material can simultaneously offer differently-oriented unpaired wave vectors (see Appendix E). Our demonstration not only provides a new degree of freedom to the realization of unique wave dynamics for applications like noise control, acoustic sensing, and imaging, but also paves the way towards practical investigation of general quantum-analogs phenomena beyond one-dimensional waveguide configuration.

Appendices

A. Simulation of the dispersion relation of the structure-induced surface mode

The simulated dispersion curves (scatters, finite element results) in Figs. 2.1(c) 3.2(b) and 3.2(c) are obtained by numerically calculating the eigenfrequencies of a unit cell for wave vectors within the irreducible Brillouin zone in COMSOL Multiphysics. As shown in Fig. A1, the three-dimensional simulation domain includes a single square hole and a cuboid region above it, corresponding to a square lattice within the *xy*-plane. Floquet periodic boundary conditions are applied in the x and y directions of the cuboid region while rigid wall boundary conditions for all other boundaries. The top wall of the simulation domain is sufficiently far away from the hole [98] to guarantee an accurate calculation of the surface mode (scattering boundary condition also works [101]). Else, the returned results would become the case of a planar waveguide connected with periodic side-branched quarter-wavelength resonators, in which an avoided crossing bandgap can be observed.

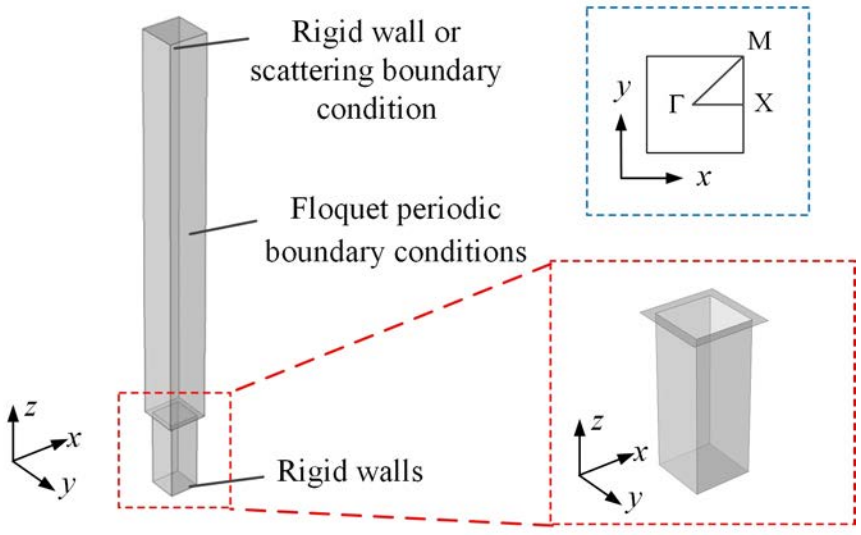

FIG. A1. Simulation model for obtaining the dispersion relation of the structure-induced surface acoustic mode. The lower right inset is a detailed view of the blind square hole. The upper right inset shows the irreducible Brillouin zone in calculation.

B. Effective medium simulation of the curved passive PT-symmetric material

For the purpose of verification, we also numerically simulate the effective medium model of the two-dimensionally extended acoustic PT-symmetric metamaterials crystal. As shown in Fig. B1(a), similarly, the one-dimensional refractive index distribution is circumferentially expanded. The result is consequently the effective medium model of the metamaterials crystal proposed in Section 4.5.

The obtained energy density fields in Figs. B1(b) and B1(c) agree well with the results that have been demonstrated in Fig. 4.17(a), showing the same one-way focusing phenomenon. To better evaluate the directional wave-vector matching, the scattered pressure and energy density [Figs. B2(a) and B2(b)] fields for forward incidence at different frequencies are simulated and presented as well. The reflected wavefront varies in accordance with the wave-vector matching condition, when the operating frequency reaches the Bragg frequency from below.

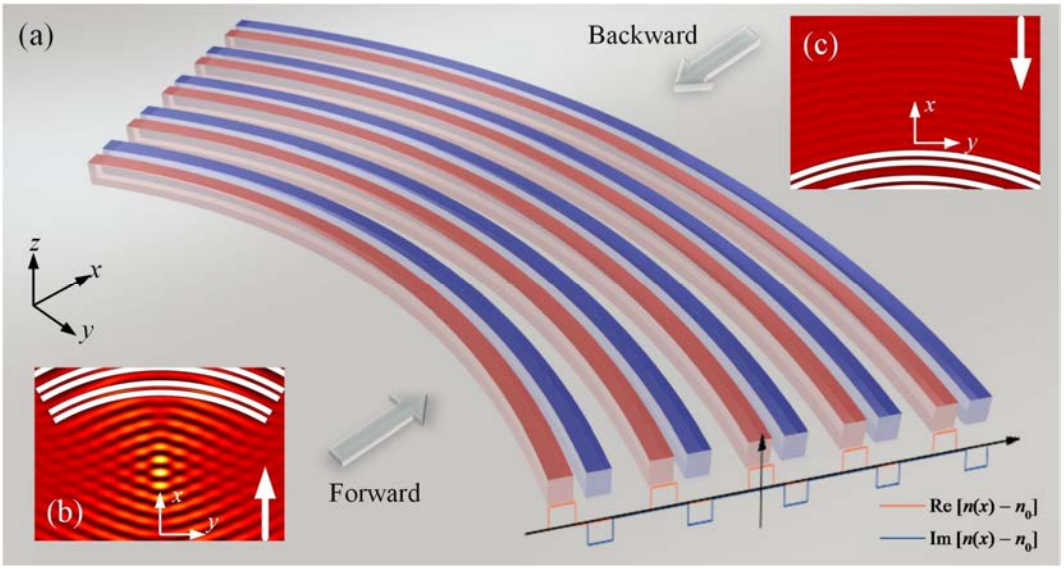

FIG. B1. Effective medium simulation of the passive acoustic PT-symmetric material in two-dimensional space for one-way sound focusing [169]. (a) Schematic of the effective medium model. Simulated energy density fields for (b) forward and (c) backward incidences. The bold arrows denote the directions of incident waves.

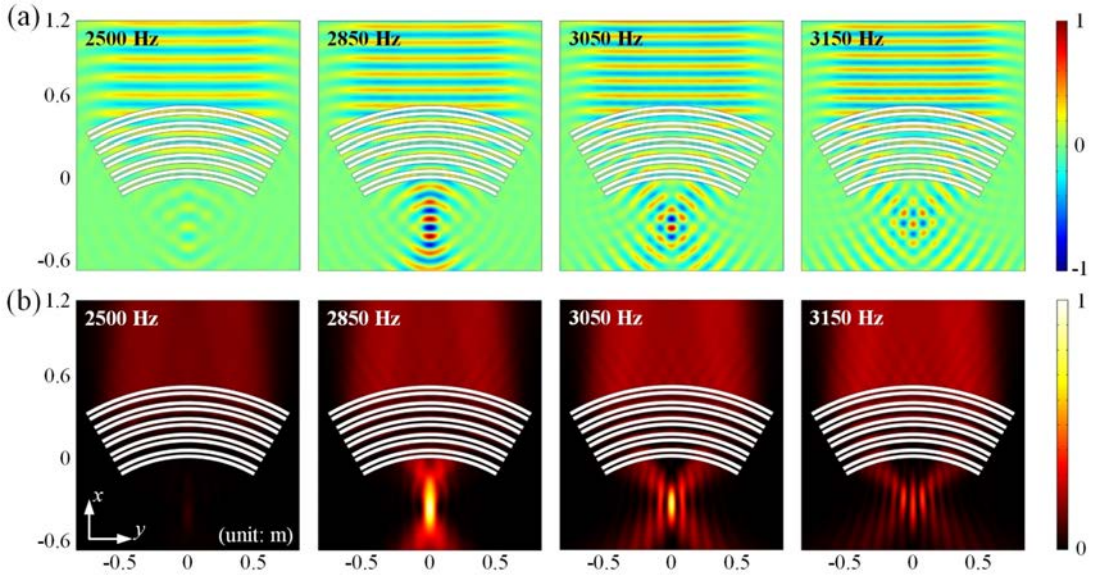

FIG. B2. Directional wave-vector match observed in the effective medium simulation [169]. (a) Scattered acoustic pressure fields and (b) scattered energy density fields at four representative frequencies. All amplitudes (pressure and energy density) are normalized per maximum value of the sound fields among the four frequencies.

To comprehensively verify the unidirectional focusing phenomenon and the underlying physics, we perform numerical simulation to study the passive PT-symmetric medium with direction-reversed one-way wave vectors, namely, when the concave side is reflectionless while the convex side is reflective. In this case, a counter-intuitive phenomenon can be expected: the passive PT-symmetric medium would prevent the concave surface from focusing waves as a result of the reflectionless nature. As illustrated in Fig. B3(a), the passive PT-symmetric potential due to the complex modulation of refractive index is flipped in direction compared to Figs. B1 and B2, which provides unidirectional wave vectors towards the outer radius. The simulated results for forward incidence are shown in Figs. B3(b). It can be observed that the scattered waves from the concave side are very weak and lead to trivial focusing effect. This is in stark contrast to the results in Figs. 4.17, 4.18, B1, and B2, in which the reflective side is concave and thus generates strongly focused sound field. On the other

hand, the wave-vector matching occurs for incident waves penetrating upon the convex side. It induces obvious reflected waves, especially prominent along the two directions that satisfy the wave-vector matching condition in two-dimensional space, as marked by the black arrows in Fig. B3(c). This further confirms the effectiveness of the unpaired wave vectors offered by the passive PT-symmetric potential.

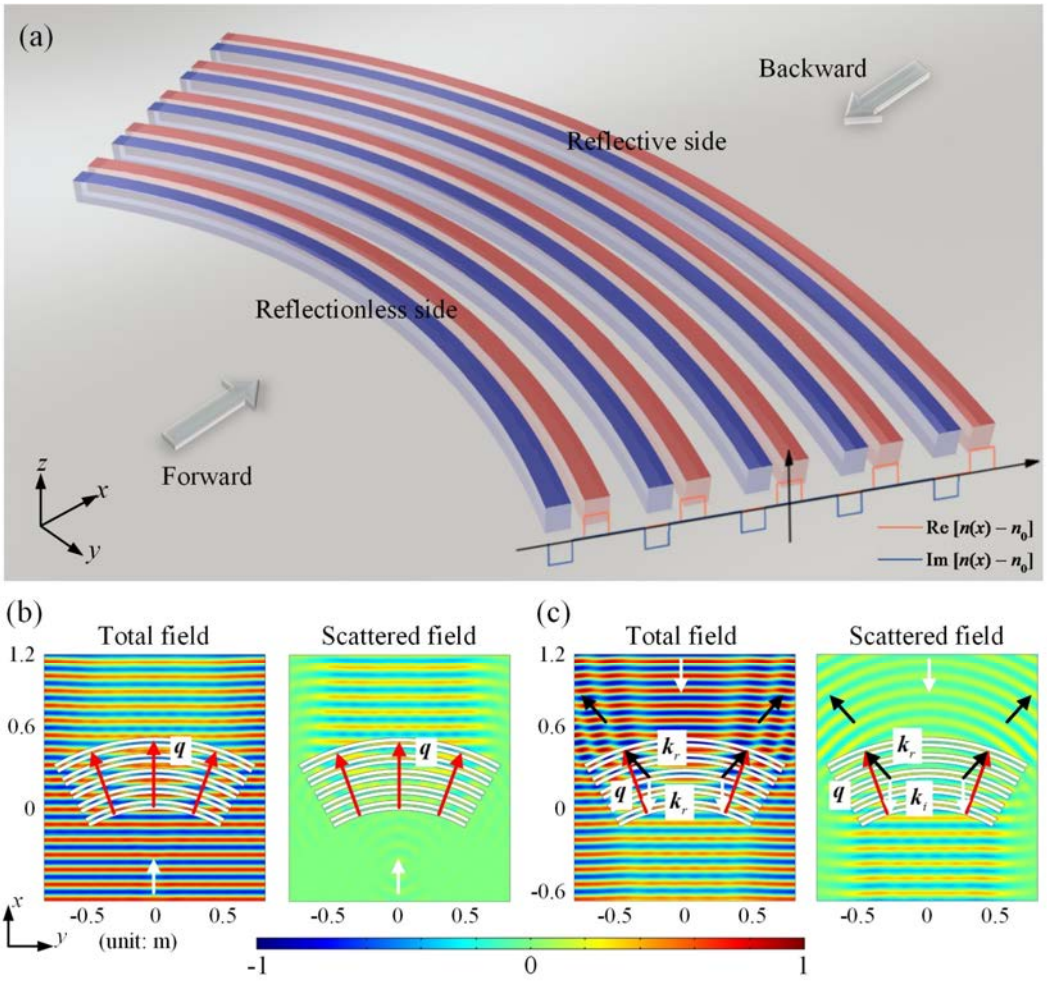

FIG. B3. Passive PT-symmetric medium with direction-reversed potential [169]. (a) Schematic of the effective medium model. The direction of the refractive index modulation is reversed, which makes the concave side reflectionless and the convex side reflective. Total (left) and scattered (right) fields for (b) forward and (c) backward incidences are simulated. The white, black, and red arrows represent the incident, the reflected, and the unpaired modulation wave vectors, respectively. Clearly, the concave side (that should have led to intensively focused sound field if the reflections are symmetric) generates very weak focusing effect.

C. Sound fields of a rigid concave reflector

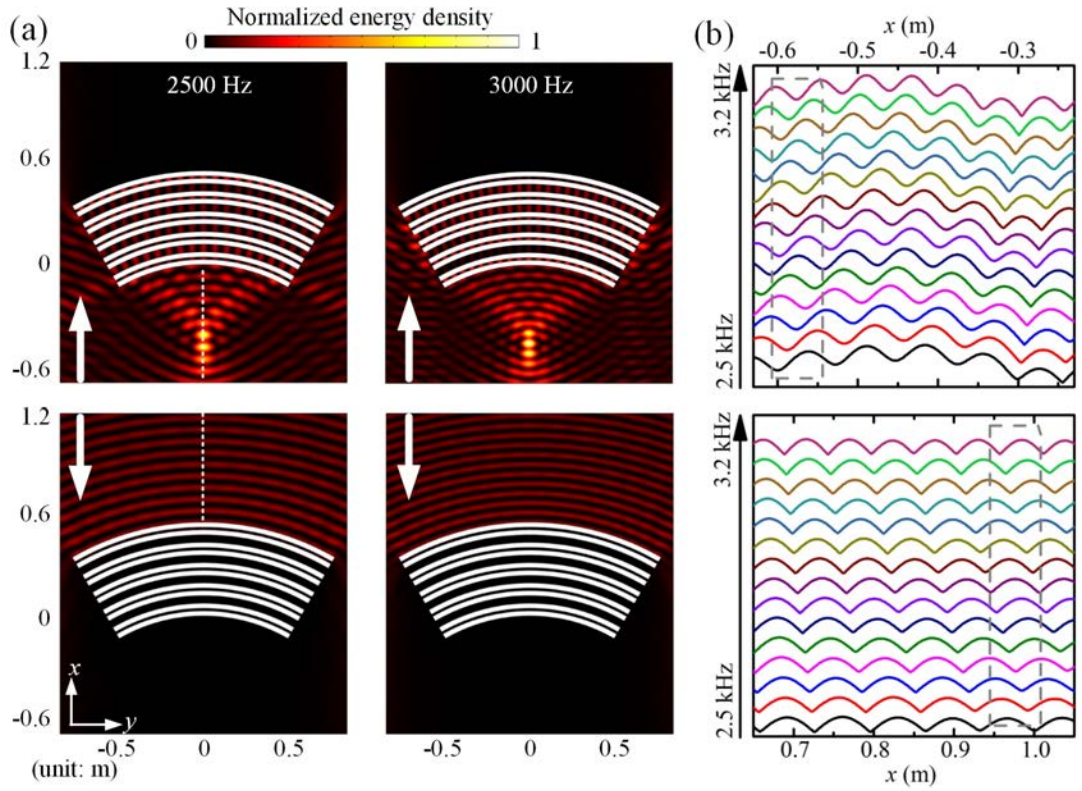

FIG. C1. Asymmetric focusing for a rigid concave reflector with the same shape of the passive PT-symmetric metamaterials crystal [169]. (a) Simulated acoustic energy density fields for forward (top half) and backward (bottom half) incidences at 2500 Hz and 3000 Hz, respectively. The arrows denote incidence directions. (b) Absolute acoustic pressure distributions for forward (top) and backward (bottom) incidences, along the white dashed lines marked in (a), from 2500 Hz to 3200 Hz with 50 Hz stepping.

Here we perform a numerical simulation to show the sound fields for a rigid concave reflector with the same shape of the passive PT-symmetric metamaterials crystal. Figure C1(a) gives the acoustic energy density fields for forward and backward incidences at 2500 Hz and 3000 Hz, respectively. Note that the designed Bragg frequency is about 2858 Hz. We recall the results for the passive PT-symmetric metamaterial crystal, where the reflection sound field is nearly negligible at 2500 Hz [Figs. 4.18(a) and 4.18(b)] but obviously focused at 3000 Hz [Fig. 4.17(a)] for the

forward incidence. Meanwhile, the reflection is nearly negligible at both 2500 Hz and 3000 Hz [Figs. 4.17(a) and 4.17(b) in the main text] for the backward incidence. In stark contrast, the reflection sound fields for the rigid reflector are strongly focused for the forward incidence but completely diverged for the backward incidence at both 2500 Hz and 3000 Hz, as shown in Figs. C1(a) and C1(b). By examining the standing wave patterns in Fig. C1(b), we further find that the standing wave ratio is approximately frequency-independent, which is also very different from the case of the passive PT-symmetric metamaterials crystal [Fig. 4.17(b)]. In addition, the focal spot of the rigid reflector is farther away from the inner concave surface than the one of the passive PT-symmetric metamaterials crystal. This is due to the fact that the effective surface of reflection for the passive PT-symmetric metamaterials crystal is actually located within the metamaterials rather than exactly at the inner concave surface.

D. Superposition of the passive parity-time-symmetric potentials

To demonstrate the possibility of constructing a rigorous two-dimensional PT-symmetric medium, we further combine the passive PT-symmetric potentials along two different directions together (linear superposition of the complex modulations $\Delta n(x)$) as presented in Fig. D1. The constructed passive PT-symmetric medium is composed of 9 pairs of complex modulations with a modulation amplitude of 3% in both the *x* and the *y* directions, following the one-dimensional configuration presented in Fig. 4.5. It simultaneously generates two unpaired wave vectors of magnitude $2k_0$ that can interact with incident waves of wavenumber k_0 from two distinct directions, resulting in clear reflections in these directions as shown in Fig. D1(a) and D1(b). Such synthesis of PT-symmetric potentials makes the passive PT-symmetric medium a genuine two-dimensional system.

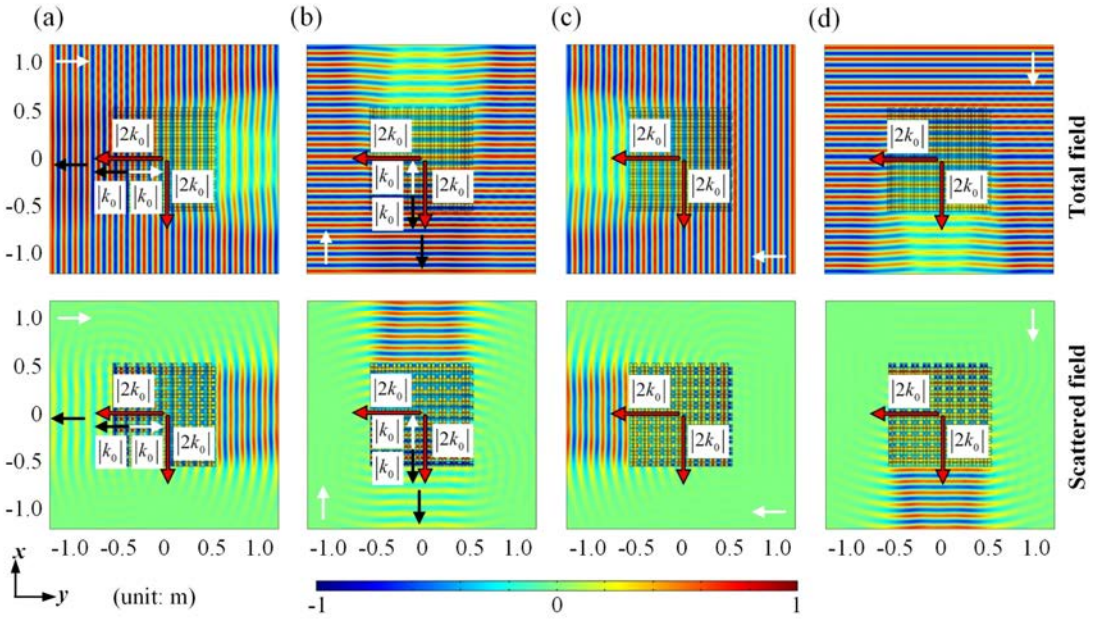

FIG. D1. Synthesizing passive PT-symmetric potentials in two-dimensional space [169]. Total (upper) and scattered (lower) acoustic pressure fields for (a) incidence from the left, (b) incidence from below, (c) incidence from the right, and (d) incidence from above. The passive PT-symmetric medium is composed of 9 pairs of complex modulations with a modulation amplitude of 3% in both the *x* and the *y* directions, providing two unpaired wave-vectors of magnitude $2k_0$ towards left and down (red arrows), for incident plane waves at 2858.3 Hz. Along the modulation directions, the PT-symmetric potentials are the same as the one-dimensional configuration in Fig. 4.5. The white and black arrows denote the incidence and reflection directions. All the amplitudes are normalized per maximum.

References

[1] V. G. Veselago, Sov. Phys. Usp. **10**, 509 (1968).

[2] J. B. Pendry, A. J. Holden, D. J. Robbins, and W. J. Stewart, Ieee T Microw Theory **47**, 2075 (1999).

[3] J. B. Pendry, A. J. Holden, W. J. Stewart, and I. I. Youngs, Phys. Rev. Lett. **76**, 4773 (1996).

[4] D. R. Smith, W. J. Padilla, D. C. Vier, S. C. Nemat-Nasser, and S. Schultz, Phys. Rev. Lett. **84**, 4184 (2000).

[5] J. B. Pendry, Phys. Rev. Lett. **85**, 3966 (2000).

[6] U. Leonhardt, Science **312**, 1777 (2006).

[7] J. B. Pendry, D. Schurig, and D. R. Smith, Science **312**, 1780 (2006).

[8] D. Schurig, J. J. Mock, B. J. Justice, S. A. Cummer, J. B. Pendry, A. F. Starr, and D. R. Smith, Science **314**, 977 (2006).

[9] Z. Liu, X. Zhang, Y. Mao, Y. Y. Zhu, Z. Yang, C. T. Chan, and P. Sheng, Science **289**, 1734 (2000).

[10] J. Li and C. T. Chan, Phys. Rev. E **70**, 055602 (2004).

[11] N. Fang, D. Xi, J. Xu, M. Ambati, W. Srituravanich, C. Sun, and X. Zhang, Nat. Mater. **5**, 452 (2006).

[12] Z. Yang, J. Mei, M. Yang, N. H. Chan, and P. Sheng, Phys. Rev. Lett. **101**, 204301 (2008).

[13] S. H. Lee, C. M. Park, Y. M. Seo, Z. G. Wang, and C. K. Kim, Phys. Rev. Lett. **104**, 054301 (2010).

[14] Z. Liang and J. Li, Phys. Rev. Lett. **108**, 114301 (2012).

[15] Z. Liang *et al.*, Sci. Rep. **3**, 1614 (2013).

[16] Y. Xie, B. I. Popa, L. Zigoneanu, and S. A. Cummer, Phys. Rev. Lett. **110**, 175501 (2013).

[17] M. Yang, G. Ma, Z. Yang, and P. Sheng, Phys. Rev. Lett. **110**, 134301 (2013).

[18] T. Brunet, A. Merlin, B. Mascaro, K. Zimny, J. Leng, O. Poncelet, C. Aristegui, and O. Mondain-Monval, Nat. Mater. **14**, 384 (2015).

[19] N. Kaina, F. Lemoult, M. Fink, and G. Lerosey, Nature **525**, 77 (2015).

[20] X. Ao and C. T. Chan, Phys. Rev. E **77**, 025601 (2008).

[21] J. Li, L. Fok, X. Yin, G. Bartal, and X. Zhang, Nat. Mater. **8**, 931 (2009).

[22] H. Jia, M. Z. Ke, R. Hao, Y. T. Ye, F. M. Liu, and Z. Y. Liu, Appl. Phys. Lett. **97**, 173507 (2010).

[23] D. Torrent and J. Sanchez-Dehesa, Phys. Rev. Lett. **105**, 174301 (2010).

[24] J. Zhu, J. Christensen, J. Jung, L. Martin-Moreno, X. Yin, L. Fok, X. Zhang, and F. J. Garcia-Vidal, Nat Phys **7**, 52 (2010).

[25] J. Christensen and F. J. Garcia de Abajo, Phys. Rev. Lett. **108**, 124301 (2012).

[26] V. M. Garcia-Chocano, J. Christensen, and J. Sanchez-Dehesa, Phys Rev Lett **112**, 144301 (2014).

[27] C. Shen, J. Xu, N. X. Fang, and Y. Jing, Phys Rev X **4** (2014).

[28] C. Shen, Y. Xie, N. Sui, W. Wang, S. A. Cummer, and Y. Jing, Phys. Rev. Lett. **115**, 254301 (2015).

[29] M. Ambati, N. Fang, C. Sun, and X. Zhang, Phys Rev B **75** (2007).

[30] F. Lemoult, M. Fink, and G. Lerosey, Phys. Rev. Lett. **107**, 064301 (2011).

[31] C. M. Park, J. J. Park, S. H. Lee, Y. M. Seo, C. K. Kim, and S. H. Lee, Phys. Rev. Lett. **107**, 194301 (2011).

[32] M. Moleron and C. Daraio, Nat. Commun. **6**, 8037 (2015).

[33] S. A. Cummer and D. Schurig, New J Phys **9**, 45 (2007).

[34] A. N. Norris, Proc. R. Soc. A **464**, 2411 (2008).

[35] H. Y. Chen and C. T. Chan, J. Phys. D: Appl. Phys. **43**, 113001 (2010).

[36] B. I. Popa, L. Zigoneanu, and S. A. Cummer, Phys. Rev. Lett. **106**, 253901 (2011).

[37] S. Zhang, C. Xia, and N. Fang, Phys. Rev. Lett. **106**, 024301 (2011).

[38] X. Zhu, B. Liang, W. Kan, X. Zou, and J. Cheng, Phys. Rev. Lett. **106**, 014301 (2011).

[39] L. Zigoneanu, B. I. Popa, and S. A. Cummer, Nat. Mater. **13**, 352 (2014).

[40] S. A. Cummer, J. Christensen, and A. Alu, Nat Rev Mater **1**, 16001 (2016).

[41] G. Ma and P. Sheng, Sci. Adv. **2**, e1501595 (2016).

[42] H. Ge, M. Yang, C. Ma, M. Lu, Y. Chen, N. Fang, and P. Sheng, Natl. Sci. Rev. (2017).

[43] B. I. Popa and S. A. Cummer, Nat. Commun. **5**, 3398 (2014).

[44] Z. M. Gu, J. Hu, B. Liang, X. Y. Zou, and J. C. Cheng, Sci. Rep. **6**, 19824 (2016).

[45] X. F. Zhu, H. Ramezani, C. Z. Shi, J. Zhu, and X. Zhang, Phys Rev X **4** (2014).

[46] R. Fleury, D. Sounas, and A. Alu, Nat. Commun. **6**, 5905 (2015).

[47] R. Fleury, D. L. Sounas, and A. Alu, IEEE J. Sel. Top. Quant. **22**, 121 (2016).

[48] C. Shi, M. Dubois, Y. Chen, L. Cheng, H. Ramezani, Y. Wang, and X. Zhang, Nat. Commun. **7**, 11110 (2016).

[49] K. Ding, G. C. Ma, M. Xiao, Z. Q. Zhang, and C. T. Chan, Phys Rev X **6** (2016).

[50] J. Christensen, M. Willatzen, V. R. Velasco, and M. H. Lu, Phys. Rev. Lett. **116**, 207601 (2016).

[51] Y. Li, B. Liang, Z. M. Gu, X. Y. Zou, and J. C. Cheng, Sci. Rep. **3**, 2546 (2013).

[52] Y. Li, X. Jiang, R. Q. Li, B. Liang, X. Y. Zou, L. L. Yin, and J. C. Cheng, Phys Rev Appl **2** (2014).

[53] Y. Xie, W. Wang, H. Chen, A. Konneker, B. I. Popa, and S. A. Cummer, Nat. Commun. **5**, 5553 (2014).

[54] G. Ma, M. Yang, S. Xiao, Z. Yang, and P. Sheng, Nat. Mater. **13**, 873 (2014).

[55] Y. Cheng, C. Zhou, B. G. Yuan, D. J. Wu, Q. Wei, and X. J. Liu, Nat. Mater. **14**, 1013 (2015).

[56] T. F. Krauss, Nat. Photon. **2**, 448 (2008).

[57] K. L. Tsakmakidis, O. Hess, R. W. Boyd, and X. Zhang, Science **358**, eaan5196 (2017).

[58] K. L. Tsakmakidis, A. D. Boardman, and O. Hess, Nature **450**, 397 (2007).

[59] C. R. Williams, S. R. Andrews, S. A. Maier, A. I. Fernandez-Dominguez, L. Martin-Moreno, and F. J. Garcia-Vidal, Nat. Photon. **2**, 175 (2008).

[60] L. Chen, G. P. Wang, Q. Q. Gan, and F. J. Bartoli, Phys Rev B **80**, 161106 (2009).

[61] Q. Gan, Y. J. Ding, and F. J. Bartoli, Phys. Rev. Lett. **102**, 056801 (2009).

[62] J. Park, K. Y. Kim, I. M. Lee, H. Na, S. Y. Lee, and B. Lee, Opt. Express **18**, 598 (2010).

[63] Q. Gan, Y. Gao, K. Wagner, D. Vezenov, Y. J. Ding, and F. J. Bartoli, Proc. Natl. Acad. Sci. **108**, 5169 (2011).

[64] M. S. Jang and H. Atwater, Phys. Rev. Lett. **107**, 207401 (2011).

[65] S. He, Y. He, and Y. Jin, Sci. Rep. **2**, 583 (2012).

[66] H. Hu, D. Ji, X. Zeng, K. Liu, and Q. Gan, Sci. Rep. **3**, 1249 (2013).

[67] A. Santillan and S. I. Bozhevolnyi, Phys Rev B **84** (2011).

[68] A. Cicek, O. A. Kaya, M. Yilmaz, and B. Ulug, J. Appl. Phys. **111**, 013522 (2012).

[69] A. Santillan and S. I. Bozhevolnyi, Phys Rev B **89** (2014).

[70] J. Christensen, P. A. Huidobro, L. Martin-Moreno, and F. J. Garcia-Vidal, Appl. Phys. Lett. **93**, 083502 (2008).

[71] J. Zhu, Y. Y. Chen, X. F. Zhu, F. J. Garcia-Vidal, X. B. Yin, W. L. Zhang, and X. Zhang, Sci. Rep. **3** (2013).

[72] V. Romero-Garcia, R. Pico, A. Cebrecos, V. J. Sanchez-Morcillo, and K. Staliunas, Appl. Phys. Lett. **102**, 091906 (2013).

[73] X. Ni, Y. Wu, Z. G. Chen, L. Y. Zheng, Y. L. Xu, P. Nayar, X. P. Liu, M. H. Lu, and Y. F. Chen, Sci. Rep. **4**, 7038 (2014).

[74] C. Zhou, B. G. Yuan, Y. Cheng, and X. J. Liu, Appl. Phys. Lett. **108**, 063501 (2016).

[75] Y. L. Xu and P. Peng, J. Appl. Phys. **117**, 035103 (2015).

[76] D. G. Zhao, Y. Li, and X. F. Zhu, Sci. Rep. **5**, 9376 (2015).

[77] Z. Tian and L. Yu, Sci. Rep. **7**, 40004 (2017).

[78] Y. Chen, H. Liu, M. Reilly, H. Bae, and M. Yu, Nat. Commun. **5**, 5247 (2014).

[79] H. Jia, M. H. Lu, X. Ni, M. Bao, and X. D. Li, J. Appl. Phys. **116**, 124504 (2014).

[80] A. V. Fedorov, N. D. Malmuth, A. Rasheed, and H. G. Hornung, AIAA J. **39**, 605 (2001).

[81] A. Fedorov, A. Shiplyuk, A. Maslov, E. Burov, and N. Malmuth, J Fluid Mech **479**, 99 (2003).

[82] L. Kelders, J. F. Allard, and W. Lauriks, J. Acoust. Soc. Am. **103**, 2730 (1998).

[83] Z. J. He, H. Jia, C. Y. Qiu, Y. T. Ye, R. Hao, M. Z. Ke, and Z. Y. Liu, Phys Rev B **83** (2011).

[84] D. Torrent and J. Sanchez-Dehesa, Phys. Rev. Lett. **108**, 174301 (2012).

[85] A. A. Maznev and V. E. Gusev, Phys Rev B **92** (2015).

[86] L. Quan, F. Qian, X. Z. Liu, X. F. Gong, and P. A. Johnson, Phys Rev B **92** (2015).

[87] O. Schnitzer, Phys Rev B **96** (2017).

[88] L. Schwan, A. Geslain, V. Romero-Garcia, and J. P. Groby, Appl. Phys. Lett. **110**, 051902 (2017).

[89] T. Liu, S. Liang, F. Chen, and J. Zhu, J. Appl. Phys. **123**, 091702 (2018).

[90] J. B. Pendry, L. Martin-Moreno, and F. J. Garcia-Vidal, Science **305**, 847 (2004).

[91] A. P. Hibbins, B. R. Evans, and J. R. Sambles, Science **308**, 670 (2005).

[92] J. Christensen, A. I. Fernandez-Dominguez, F. De Leon-Perez, L. Martin-Moreno, and F. J. Garcia-Vidal, Nat Phys **3**, 851 (2007).

[93] J. Christensen, L. Martin-Moreno, and F. J. Garcia-Vidal, Phys Rev B **81** (2010).

[94] Y. Zhou, M. H. Lu, L. Feng, X. Ni, Y. F. Chen, Y. Y. Zhu, S. N. Zhu, and N. B. Ming, Phys. Rev. Lett. **104**, 164301 (2010).

[95] L. Quan, X. Zhong, X. Liu, X. Gong, and P. A. Johnson, Nat. Commun. **5**, 3188 (2014).

[96] H. Jia, M. H. Lu, Q. C. Wang, M. Bao, and X. D. Li, Appl. Phys. Lett. **103**, 103505 (2013).

[97] Y. T. Ye, M. Z. Ke, Y. X. Li, T. Wang, and Z. Y. Liu, J. Appl. Phys. **114**, 154504 (2013).

[98] A. A. Maznev, G. Gu, S. Y. Sun, J. Xu, Y. Shen, N. Fang, and S. Y. Zhang, New J Phys **17**, 042001 (2015).

[99] J. Y. Lu, C. Y. Qiu, M. Z. Ke, and Z. Y. Liu, Appl. Phys. Lett. **106**, 201901 (2015).

[100] J. Cui, J. H. Liu, Y. W. Mao, Y. F. Li, and X. Z. Liu, Aip Adv **7**, 115301 (2017).

[101] S. Yves, R. Fleury, F. Lemoult, M. Fink, and G. Lerosey, New J Phys **19**, 075003 (2017).

[102] T. Liu and J. Zhu, Pr Int Congr Sound V (2016).

[103] F. J. Garcia-Vidal, L. Martin-Moreno, and J. B. Pendry, J. Opt. A: Pure Appl. Opt. **7**, S97 (2005).

[104] X. L. Wang, Appl. Phys. Lett. **96**, 134104 (2010).

[105] G. Theocharis, O. Richoux, V. R. Garcia, A. Merkel, and V. Tournat, New J Phys **16**, 093017 (2014).

[106] G. P. Ward, R. K. Lovelock, A. R. Murray, A. P. Hibbins, J. R. Sambles, and J. D. Smith, Phys. Rev. Lett. **115**, 044302 (2015).

[107] M. Moleron, M. Serra-Garcia, and C. Daraio, New J Phys **18**, 033003 (2016).

[108] X. Jiang, B. Liang, R. Q. Li, X. Y. Zou, L. L. Yin, and J. C. Cheng, Appl. Phys. Lett. **105**, 243505 (2014).

[109] A. Merkel, G. Theocharis, O. Richoux, V. Romero-Garcia, and V. Pagneux, Appl. Phys. Lett. **107**, 244102 (2015).

[110] N. Jimenez, V. Romero-Garcia, V. Pagneux, and J. P. Groby, Phys Rev B **95** (2017).

[111] N. Jimenez, V. Romero-Garcia, V. Pagneux, and J. P. Groby, Sci. Rep. **7**, 13595 (2017).

[112] Y. Li, C. Shen, Y. Xie, J. Li, W. Wang, S. A. Cummer, and Y. Jing, Phys. Rev. Lett. **119**, 035501 (2017).

[113] V. C. Henriquez, V. M. Garcia-Chocano, and J. Sanchez-Dehesa, Phys Rev Appl **8**, 014029 (2017).

[114] M. R. Stinson, J. Acoust. Soc. Am. **89**, 550 (1991).

[115] V. F. Kozlov, A. V. Fedorov, and N. D. Malmuth, J. Acoust. Soc. Am. **117**, 3402 (2005).

[116] W. R. Kampinga, University of Twente, 2010.

[117] E. L. Bolda, R. Y. Chiao, and J. C. Garrison, Phys. Rev. A **48**, 3890 (1993).

[118] S. Sahebdivan, University of St Andrews, 2016.

[119] N. Fang, H. Lee, C. Sun, and X. Zhang, Science **308**, 534 (2005).

[120] Z. Jacob, L. V. Alekseyev, and E. Narimanov, Opt. Express **14**, 8247 (2006).

[121] A. Salandrino and N. Engheta, Phys Rev B **74** (2006).

[122] Z. Liu, H. Lee, Y. Xiong, C. Sun, and X. Zhang, Science **315**, 1686 (2007).

[123] S. Guenneau, A. Movchan, G. Petursson, and S. A. Ramakrishna, New J Phys **9**, 399 (2007).

[124] K. Deng, Y. Q. Ding, Z. J. He, H. P. Zhao, J. Shi, and Z. Y. Liu, J. Appl. Phys. **105**, 124909 (2009).

[125] J. J. Park, C. M. Park, K. J. B. Lee, and S. H. Lee, Appl. Phys. Lett. **106**, 051901 (2015).

[126] F. Liu, F. Cai, S. Peng, R. Hao, M. Ke, and Z. Liu, Phys. Rev. E **80**, 026603 (2009).

[127] X. M. Zhou and G. K. Hu, Appl. Phys. Lett. **98**, 263510 (2011).

[128] H. K. Zhang, X. M. Zhou, and G. K. Hu, Appl. Phys. Lett. **109**, 224103 (2016).

[129] J. de Rosny and M. Fink, Phys. Rev. Lett. **89**, 124301 (2002).

[130] A. Sukhovich, B. Merheb, K. Muralidharan, J. O. Vasseur, Y. Pennec, P. A. Deymier, and J. H. Page, Phys. Rev. Lett. **102**, 154301 (2009).

[131] A. A. Maznev and O. B. Wright, Wave Motion **68**, 182 (2017).

[132] S.-C. S. Lin, T. J. Huang, J.-H. Sun, and T.-T. Wu, Phys Rev B **79** (2009).

[133] A. Climente, D. Torrent, and J. Sanchez-Dehesa, Appl. Phys. Lett. **97**, 104103 (2010).

[134] T. M. Chang, G. Dupont, S. Enoch, and S. Guenneau, New J Phys **14**, 035011 (2012).

[135] S. M. Mansfield and G. S. Kino, Appl. Phys. Lett. **57**, 2615 (1990).

[136] X. Wang, H. Chen, H. Liu, L. Xu, C. Sheng, and S. Zhu, Phys. Rev. Lett. **119**, 033902 (2017).

[137] Y. Li, B. Liang, X. Tao, X. F. Zhu, X. Y. Zou, and J. C. Cheng, Appl. Phys. Lett. **101**, 233508 (2012).

[138] X. Zhu, K. Li, P. Zhang, J. Zhu, J. Zhang, C. Tian, and S. Liu, Nat. Commun. **7**, 11731 (2016).

[139] C. M. Bender and S. Boettcher, Phys. Rev. Lett. **80**, 5243 (1998).

[140] R. El-Ganainy, K. G. Makris, D. N. Christodoulides, and Z. H. Musslimani, Opt. Lett. **32**, 2632 (2007).

[141] K. G. Makris, R. El-Ganainy, D. N. Christodoulides, and Z. H. Musslimani, Phys. Rev. Lett. **100**, 103904 (2008).

[142] A. Guo, G. J. Salamo, D. Duchesne, R. Morandotti, M. Volatier-Ravat, V. Aimez, G. A. Siviloglou, and D. N. Christodoulides, Phys. Rev. Lett. **103**, 093902 (2009).

[143] C. E. Rüter, K. G. Makris, R. El-Ganainy, D. N. Christodoulides, M. Segev, and D. Kip, Nat Phys **6**, 192 (2010).

[144] L. Feng, R. El-Ganainy, and L. Ge, Nat. Photon. **11**, 752 (2017).

[145] R. El-Ganainy, K. G. Makris, M. Khajavikhan, Z. H. Musslimani, S. Rotter, and D. N. Christodoulides, Nat Phys **14**, 11 (2018).

[146] H. Zhao and L. Feng, Natl. Sci. Rev. **5**, 183 (2018).

[147] S. Longhi, Phys. Rev. Lett. **103**, 123601 (2009).

[148] Y. L. Xu, W. S. Fegadolli, L. Gan, M. H. Lu, X. P. Liu, Z. Y. Li, A. Scherer, and Y. F. Chen, Nat. Commun. **7**, 11319 (2016).

[149] Z. Lin, H. Ramezani, T. Eichelkraut, T. Kottos, H. Cao, and D. N. Christodoulides, Phys. Rev. Lett. **106**, 213901 (2011).

[150] L. Ge, Y. D. Chong, and A. D. Stone, Phys. Rev. A **85** (2012).

[151] A. Regensburger, C. Bersch, M. A. Miri, G. Onishchukov, D. N. Christodoulides, and U. Peschel, Nature **488**, 167 (2012).

[152] L. Feng, Y. L. Xu, W. S. Fegadolli, M. H. Lu, J. E. Oliveira, V. R. Almeida, Y. F. Chen, and A. Scherer, Nat. Mater. **12**, 108 (2013).

[153] B. Peng *et al.*, Nat Phys **10**, 394 (2014).

[154] S. Longhi, Phys. Rev. A **82**, 031801 (2010).

[155] Y. D. Chong, L. Ge, and A. D. Stone, Phys. Rev. Lett. **106**, 093902 (2011).

[156] Y. Sun, W. Tan, H. Q. Li, J. Li, and H. Chen, Phys. Rev. Lett. **112**, 143903 (2014).

[157] L. Feng, Z. J. Wong, R. M. Ma, Y. Wang, and X. Zhang, Science **346**, 972 (2014).

[158] H. Hodaei, M. A. Miri, M. Heinrich, D. N. Christodoulides, and M. Khajavikhan, Science **346**, 975 (2014).

[159] P. Miao, Z. Zhang, J. Sun, W. Walasik, S. Longhi, N. M. Litchinitser, and L. Feng, Science **353**, 464 (2016).

[160] H. Zhao, W. S. Fegadolli, J. Yu, Z. Zhang, L. Ge, A. Scherer, and L. Feng, Phys. Rev. Lett. **117**, 193901 (2016).

[161] C. M. Bender and D. J. Weir, J. Phys. A: Math. Theor. **45**, 425303 (2012).

[162] C. M. Bender, M. Gianfreda, and S. P. Klevansky, Phys. Rev. A **90**, 022114 (2014).

[163] L. Ge and A. D. Stone, Phys Rev X **4** (2014).

[164] H. Benisty, A. Lupu, and A. Degiron, Phys. Rev. A **91**, 053825 (2015).

[165] M. Turduev, M. Botey, I. Giden, R. Herrero, H. Kurt, E. Ozbay, and K. Staliunas, Phys. Rev. A **91** (2015).

[166] W. W. Ahmed, R. Herrero, M. Botey, and K. Staliunas, Phys. Rev. A **94** (2016).

[167] A. V. Poshakinskiy, A. N. Poddubny, and A. Fainstein, Phys. Rev. Lett. **117**, 224302 (2016).

[168] Y. Auregan and V. Pagneux, Phys. Rev. Lett. **118**, 174301 (2017).

[169] T. Liu, X. F. Zhu, F. Chen, S. J. Liang, and J. Zhu, Phys. Rev. Lett. **120**, 124502 (2018).

[170] J. W. S. B. Rayleigh, *The Theory of Sound: Volume II* (MacMillan and Company, 1929).

[171] G. Kirchhoff, Ann. Phys. (Berl.) **210**, 177 (1868).

[172] C. Zwikker and C. W. Kosten, *Sound absorbing materials* (Elsevier, 1949).

[173] D. Y. Maa, J. Acoust. Soc. Am. **104**, 2861 (1998).

[174] V. Fokin, M. Ambati, C. Sun, and X. Zhang, Phys Rev B **76** (2007).

[175] X. Zhu, L. Feng, P. Zhang, X. Yin, and X. Zhang, Opt. Lett. **38**, 2821 (2013).

[176] R. Ferrini, R. Houdre, H. Benisty, M. Qiu, and J. Moosburger, J. Opt. Soc. Am. B **20**, 469 (2003).